MECHANISTIC MODELING OF JET IMPINGEMENT BOILING

MECHANISTIC MODELING OF JET IMPINGEMENT BOILING

By Ahmed Bekhit Ahmed, BSc., MSc.

A Thesis Submitted to the School of Graduate Studies in Partial Fulfillment of the
Requirements for the Degree Doctor of Philosophy

McMaster University DOCTOR OF PHILOSOPHY (2016) Hamilton, Ontario (Mechanical Engineering)

TITLE: Mechanistic Modeling of Jet Impingement Boiling

AUTHOR: Ahmed Bekhit Ahmed, BSc., MSc. (McMaster University)

SUPERVISOR: Professor Mohamed S. Hamed

NUMBER OF PAGES: xiv, 124

Abstract

The current work presents a steady-state experimental study of nucleate and transition boiling under a planar water jet impinging on a flat horizontal copper surface. The maximum attained surface temperature is 560 °C and the maximum wall heat flux is 5 $\mathrm{MW/m^2}$. The boiling curves under the impinging jet have been obtained for 0.6 and 0.7 m/s jet velocity and 15 °C of subcooling. The boiling curves are similar to flow boiling curves in the nucleate boiling regime. However, the curves are characterized by a region of constant heat flux (shoulder) in the transition boiling regime.

The current work studies nucleate and transition impinging jet boiling. Determining the bubble size is essential for the heat flux estimation in the nucleate boiling regime. There are limited number of studies targeting bubble dynamics under impinging jets. The current study presents a new force balance for bubbles growing in the stagnation region for the nucleate boiling regime. The jet dynamics cause two more force components compared to the case of flow boiling: (1) an asymmetric bubble growth force for a moving fluid and (2) a pressure force caused by the jet stagnation. As the force balance depends on bubble growth rate, Zuber's model for non-uniform temperature field has been found to best represent the current experimental data with different b values. $b = \pi/7$ has been found to best fit the data at the stagnation region and $b = 5\pi/6$ for the parallel flow region.

In transition boiling, the existence of the shoulder phenomenon has been attributed to vapor pockets break-up and formation on the heated surface. Vapor break-up and formation has been observed using high speed imaging. A new wall heat flux partitioning model has been developed based on the current physical understanding. The model has two components of heat transfer. Each component has been assumed to have a weighted contribution to the total heat flux based on the degree of superheat.

The components are based on two mechanisms observed during vapor break-up. The first mechanism is due to the interaction between the jet dynamics and the vapor pockets in the stagnation region. The second mechanism which is more frequent at higher temperatures is due to Rayleigh-Taylor instability. The instability of the liquid-vapor interface grows and liquid wets the surface in the form of liquid columns. The modeled wall heat flux follows the experimental boiling curve reasonably. The model has a normalized root mean square error (NRMSE) of 33%.

The wall heat flux has been found to be dependent on the vapor break-up frequency. A micro-size fiber optic has been used to measure the vapor oscillation frequency on the boiling surface. The probe has been produced by a new etching technique to assure minimal interference with the vapor formation or break-up. Based on the collected data, the break-up frequency has been modeled.

To my beautiful wife, Salma

Acknowledgments

Study of boiling is full of challenges and difficulties. The current study has been inspiring, exciting and often frustrating, yet interesting. I wish to express my sincere gratitude to my supervisor Dr. Mohamed S. Hamed who guided me through this study. This work would not have been concluded without the help, encouragement and continuous support of my supervisor. I would like to express my sincere thanks to my supervisory committee members, Dr. Amad Abdul-Razzak and Dr. James Cotton for believing in the value of the current work and for their valuable suggestions and feedback. Special thanks to Dr. Ross L. Judd who enriched the science of boiling and heat transfer throughout the years.

I am indebted to the technicians of the Mechanical Engineering Department at McMaster University: Ron Lodewyks, Jim McLaren, Mark MacKenzie, Joe Verhaeghe, Michael Lee and John Colenbrander for their help in constructing the experimental setup. Thanks are due to my colleagues; Dr. Mohamed Awwad, Dr. Ahmed Omar, Dr. Mohammed A. El Sayed, and David Nakhla for their technical assistance and the ongoing discussion.

Last but not least, I'd like to express my deepest gratitude to my family and wife for their never ending support.

Contents

List of Figures

List of Abbreviations and Symbols

Abbreviations

CHF	Critical heat flux
FPF	Fluid phase function
ONB	Onset of nucleate boiling
OSV	Onset of significant void

Latin

A	Area, empirical factor
a	Acceleration, constant
A_l/A_c	Liquid to cell area ratio
B	Empirical factor
Bo	Bond number
c	Area factor, constant
c_i	Empirical constant
C_P	Specific heat
D	Diameter
f	Frequency
F	Force
g	Gravitational acceleration
h	Heat transfer coefficient
h_{fg}	Latent heat of vaporization
h_v	Vapor layer height
Ja	Jakob number
k	Wavenumber
K	Thermal conductivity
m	Empirical constant
$\dot{m}$	Mass flow rate
N	Number of phase changes
N_a	Nucleation site density
n	Exponent
P	Pressure
q	Heat flux
Re	Reynolds number
r	radius
T	Temperature
t	Time
V_{th}	Threshold voltage
V	Volume
V_j	Jet velocity at nozzle exit
w	Jet width
We	Weber number
x	distance from the jet center
y	Distance from the surface

Greek

α	Thermal diffusivity, void fraction
γ	Contact angle
Δ	Difference
δ_{th}	Thermal BL thickness
δ_m	Microlayer thickness

η_0	Disturbance amplitude
λ_c	Critical wavelength
μ	Dynamic viscosity
ω	Growth rate
ϕ	Optical probe angle, Polar contact angle
ρ	Density
σ	Surface tension
τ	Time constant
θ	Camera tilt angle, dimensionless temperature
ε	Turbulence dissipation

Subscripts

∞	Surrounding
b	bubble
eff	Effective
ev	Evaporation
f	Film
fc	Forced convection
fm	First minimum
g	Growth
h	Heater
i	Intrusion, interface
j	Jet
l	Liquid
min	Minimum
p	Pumping
q	Quenching
s	Sampling
sat	Saturation
sh	Shoulder
sub	Subcooling
sup	Superheat
tc	Transient conduction
v	Vapor
w	Wall / Waiting

Chapter 1

Introduction

The limiting factor in many industries is the maximum operating temperature and/or the maximum heat flux that can be dissipated from hot surfaces. A basic example is steel quenching where high heat fluxes are required as final product properties depend on cooling rates and surface temperatures [1]. Another example is electronic chips cooling where method of cooling is critical to keep component temperature below its desired operating value [2].

Liquid impinging jets are one of the most effective cooling means as the heat transfer coefficient reaches $10\,\mathrm{kW/m^2}$ [1]. Boiling under impingement jets is similar to external flow boiling with different flow dynamics based on the jet configuration and properties. There are five impinging jet configurations: free, submerged, confined, plunging and wall jet [1]. Flow field of free surface jet, shown in Fig. (1.1), is characterized by three consecutive flow zones: stagnation zone (A), acceleration zone (B), parallel flow zone (C). Impinging flow causes an increase in pressure to its maximum value at the stagnation zone with a zero parallel velocity component. As flow direction changes and becomes parallel to the surface, in the acceleration zone, the pressure decreases and the stream-wise velocity increases till both reach their steady state values at the parallel zone [1].

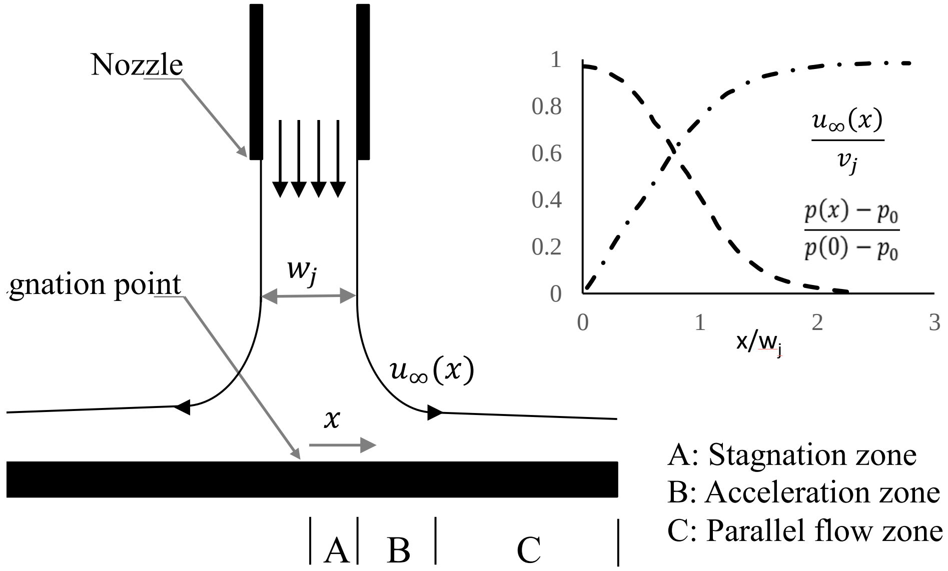

Figure 1.1: Schematic of a free surface impinging jet [1]

Although single-phase jets are capable of extracting high flux at the stagnation zone, surface heat flux increases significantly once boiling takes place. The capability of jet impingement boiling in extracting high heat fluxes is due to: (i) the ability of the impinging, perpendicular, flow to reduce the thickness of the thermal boundary layer at the stagnation zone, (ii) the induced flow mixing due to bubble generation, and (iii) the latent heat associated with phase change boiling on the surface [3]. The critical heat flux (CHF) in jet impingement boiling is almost 3 - 4 times higher than CHF in pool boiling and 0.8 - 1.2 higher than flow boiling.

Boiling can be divided into two main categories: pool boiling and flow boiling. Boiling under impinging jets is a form of flow boiling with special hydrodynamic characterizations. The boiling modes observed under the jet are: nucleate boiling, transition boiling and film boiling. The following sections provide a brief summary of the studies focusing on nucleate boiling and transition boiling regimes in flow and impinging jet boiling.

1.1 Nucleate Boiling

Researchers have been interested in studying impingement jets for decades. The significance of impinging jet boiling was clearly shown when Katto and Kunihiro [4] studied critical heat flux (CHF) and introduced a liquid jet to control the vapor mass on the boiling surface [5]. They noticed a different behavior than classical pool boiling as the jet splashed once it touched the surface and the CHF increased with the increase of the jet velocity.

While the theoretical understanding of the boiling phenomenon has not been fully established, empirical studies and correlations for heat transfer modeling have been extensively investigated [5]. Many studies have been carried out to predict the wall heat flux in the case of subcooled nucleate boiling for different flow conditions and jet configurations. Wolf and Incropera [1] reviewed the experimental studies carried out until 1993. Recently, Qiu et al. [5] updated this review and included recent experimental studies (1993 − 2014) on nucleate boiling from onset of nucleate boiling (ONB) to CHF. They included different jet configurations (free surface, submerged, and confined), jet conditions (jet velocity, jet hydraulic diameter, number of jets, etc.) and surface conditions such as surface aging.

The main objective of most of the impinging jet boiling studies is modeling the wall heat flux. Most studies in the literature, which modeled the heat flux of fully developed nucleate boiling under jet impingement, take the form,

$$q_w = c\,\Delta T_{sup}^{n} \tag{1.1}$$

where c and n are constants determined empirically. Table 1.1 shows a list of the most important empirical studies of jet impingement boiling.

Table 1.1: Fully developed nucleate boiling empirical relations

Authors	Fluid	Jet	ΔT_{sup}[°C]	v_j [m/s]	c	n
Copeland [6]	water	free, circ	8 – 31	0.8 – 6.4	740	2.3
Ruch and Holman [7]	R-113	free, circ	17 – 44	1.2 – 6.9	467	1.95
Monde and Katto [8]	water	free, circ	18 – 46	3.9 – 26	450	2.7
Monde and Katto [8]	R-113	free, circ	15 – 30	2 – 17	790	3.2
Ishigai et al. [9]	water	free, plan	26 – 47	1 – 2.1	42	3.2
Miyasaka et al. [10]	water	free, plan	26 – 90	1.1 – 15.3	79	3
Katto and Kunihiro [4]	water	sub, circ	18 – 38	2.0 – 2.6	340	2.7
Ma and Bergles [11]	R-113	sub, circ	26 – 33	1.0 – 2.7	0.15	4.4
Hall et al. [12]	water	free, circ	50 – 100	3	166	2.7
Liu and Qiu [13]	water [1]	free, circ	25 – 40	1 – 6.5	2.8E-9	9
Qiu and Liu [14]	water–CuO	free, circ	50 – 65	0.5 – 6.5	1.4E-8	8

1.1.1 Effect of Jet Velocity and Degree of Subcooling

The effects of jet velocity and degree of subcooling on the wall heat flux have been studied extensively through the years [8–10, 15, 16]. Ishigai et al. [9] studied the heat transfer of a planar water jet impinging on a flat surface. Steady state experiments were carried out in the nucleate boiling regime to study the effect of jet velocity. They reported an insignificant effect of jet velocities from 1 to 2.1 m/s on the heat flux at the same degree of superheat, 35 °C. Similarly, Miyasaka et al. [10] investigated the effect of a planar jet velocity for a highly subcooled fluid (85 – 108 °C). They found that jet velocity from 1.1 to 15.3 m/s has no noticeable effect on the heat flux for degrees of superheat from 26 to 80 °C. [15]. In similar studies, Wang and Monde [16] and Zhou and Ma [3] found that before ONB, the heat flux increases with jet velocity. But after it, the velocity effect is not apparent.

---

[1] This study was carried out on a superhydrophilic surface

The effect of the subcooling was studied by Ishigai et al. [9] and Vader et al. [15]. Ishigai et al. [9] found that there is a minor effect of the degree of subcooling on the nucleate boiling while doubling the degree of subcooling from 35 to 70 °C of subcooling for jet velocity of 2.1 m/s. Vader et al. [15] studied the effect of subcooling on a flat, constant heat flux surface for jet velocities of 1.8 to 4.5 m/s. They reported a minor effect of increasing the degree of subcooling from 50 to 70 °C on the fully developed nucleate boiling heat flux at the stagnation region.

The CHF was found to greatly depend on both the degree of subcooling and the jet velocity. Ishigai et al. [9] found that the CHF at 55 °C of subcooling is four times higher than that at 5 °C of subcooling and 1.5 times its value when the jet velocity was increased three times. Miyasaka et al. [10] also reported an increase in the CHF with the jet velocity and the degree of subcooling.

1.1.2 Wall Heat Flux Partitioning

The studies listed in Table 1.1 developed empirical relation for the heat flux similar to Eq. (1.1). Although empirical relations constants can be easily obtained, their applicability is limited to the conditions they are developed for. Additionally, empirical modeling does not provide details about the physical mechanisms associated. Mechanistic modeling would overcome the limitations of empirical models, if the underlying physics are modeled.

The approach of wall heat flux partitioning based on mechanistic modeling has been introduced to overcome the limitations of models empiricism [17]. The wall heat flux is divided into multiple components each representing a physical mechanism. Most of the studies that followed the wall heat flux partitioning approach were studying nucleate boiling in flow boiling. Recently, the approach of partitioning has been applied for the case of jet impingement boiling [18, 19]. The following is a review of the different approaches implemented to mechanistically model flow and jet impingement boiling.

1.1.2.1 Wall heat flux partitioning: flow boiling

One of the oldest wall flux partitioning models for flow boiling was proposed by Bowring [20]. He assumed that the wall heat flux can be partitioned into three major components: (i) single phase convection where there is no bubble generation (q_{fc}), (ii) evaporation heat transfer from the superheated layer at bubble base (q_{ev}), and (iii) heat transferred due to disturbance caused by bubbles departing and subcooled liquid replacing bubble volume, referred to as pumping component (q_p). The wall heat flux can be represented as,

$$q_w = q_{fc} + q_{ev} + q_p \tag{1.2}$$

where q_w is the wall heat flux, q_{fc} is represented by single phase convection correlations, and q_{ev} and q_p are defined as,

$$q_{ev} = f\, N_a\, V_b\, \rho_v\, h_{fg} \tag{1.3}$$

$$q_p = f\, N_a\, V_b\, \rho_l\, C_p\, \Delta T_{sup} \tag{1.4}$$

where f is bubble release frequency, N_a is active nucleation site density, V_b is bubble volume, ρ is the density, and h_{fg} is the latent heat of vaporization. Due to the shortage in information about f, N_a, D_b and the inability to model them, Eq. (1.3) and Eq. (1.4) can not be evaluated. The agitation (pumping) component is rather related to the evaporation component through an empirical parameter, $\epsilon = q_p/q_{ev}$, which is a function of the pressure. It is defined as the ratio between the agitation and the evaporation component. The wall heat flux can be expressed as,

$$q_w = q_{fc} + (1 + \epsilon) q_{ev} \tag{1.5}$$

Knowing q_{fc} and ϵ, $q_e v$ can be evaluated from Eq. (1.5); however, the three different components are not evaluated independently. Building on that, Rouhani and Axelsson [21] studied void fraction in flow boiling. They divided the surface into two regions, boiling with static bubbles and boiling with bubble departure with the maximum voidage, α_c, happening at the transition from the first to the second region. The heat flux is comprised of a single phase component and a boiling component. The boiling component is divided into an evaporation partition and a sensible heat partition due to subcooled liquid filling the volume created by the departed bubble. The single phase component (non-boiling component) decreases with the increase in void fraction and becomes zero at the transition to the second region. The wall heat flux is expressed as,

$$q_w = h_{fc} \left(1 - \frac{\alpha}{\alpha_c}\right) \Delta T_{sub} + \dot{m}_v h_{fg} + \dot{m}_v C_p \frac{\rho_l}{\rho_v} \Delta T_{sub} \tag{1.6}$$

where $\dot{m}_v$ is the evaporated liquid mass per unit time per unit area of the surface, α is the void fraction and h_{fg} is the forced convection heat transfer coefficient. Griffith et al. [22] studied pressure drop in flow channels. The pressure drop in the case of boiling is dependent on the void fraction. Griffith noticed a highly subcooled boiling region with low void fraction and less subcooled boiling region with high void fraction. In the first region, scattered static bubbles act as surface disturbances and heat flux is partitioned into: a single-phase flow component and a boiling component. In the second region, the heat is assumed to be transferred to the liquid through condensation of the bubbles.

Zeitoun [23] studied void fraction in vertical flow conduits. He used Bowring's model (Eq. 1.5) and found an expression for the agitation (pumping) component to the evaporation component, ϵ. He calculated the agitation heat flux based on the thermal boundary layer mean temperature difference and the volume of the thermal boundary layer removed by the departed bubble. So, he derived an expression for ϵ as follows,

$$\epsilon = \frac{3}{4}\frac{\delta_{th}}{D_s} Ja_{sup} \tag{1.7}$$

where D_s is Sauter Diameter and δ_{th} is the thermal boundary thickness, which are expressed as follows,

$$\delta_{th} = \frac{K_l(\Delta T_{sup} + \Delta T_{sub})}{q_w} \tag{1.8}$$

$$D_s = 0.0683\left(\frac{\sigma}{g\Delta\rho}\right)^{0.5} \frac{(\rho_l/\rho_g)^{1.326}}{Re_{D_h}^{0.324}\left[Ja_{sub} + \frac{149.2(\rho_l/\rho_g)^{1.326}}{Bo^{0.487}Re_{D_h}^{1.6}}\right]} \tag{1.9}$$

where K_l is liquid thermal conductivity, Ja is Jakob number, and BO is Bond number. Zeitoun did not calculate q_{ev} directly, but estimated it instead, based on q_w and q_{fc}. The pumping component, q_p, is calculated from $q_p = \epsilon\, q_{ev}$. Zeitoun and many other researchers utilized Bowring's model, but the evaporation component was not calculated independently. It was rather calculated after knowing the total wall heat flux q_w and q_{fc}. It is worth noting that the main objective of most of the mentioned models is to predict void fraction and not total surface heat flux. However, their efforts in wall heat flux partition paved the road to conduct heat flux studies.

Del Valle and Kenning [24] experimentally investigated subcooled flow nucleate boiling at atmospheric pressure. They came up with a mechanistic model for wall heat flux, where the boiling surface is divided into four areas, as shown in Fig. (1.2): maximum bubble projected area, surrounding area of influence, overlapping areas of influence, and non-boiling area. Each area has a different heat transfer mechanism. The total wall heat flux is expressed as a summation of three components: (i) evaporation heat flux which is the heat from the microlayer evaporation happening over the maximum bubble projected area, (ii) quenching heat flux in both the bubble projected area and the area of influence, and (iii) convective heat flux. The maximum bubble projected area is defined as,

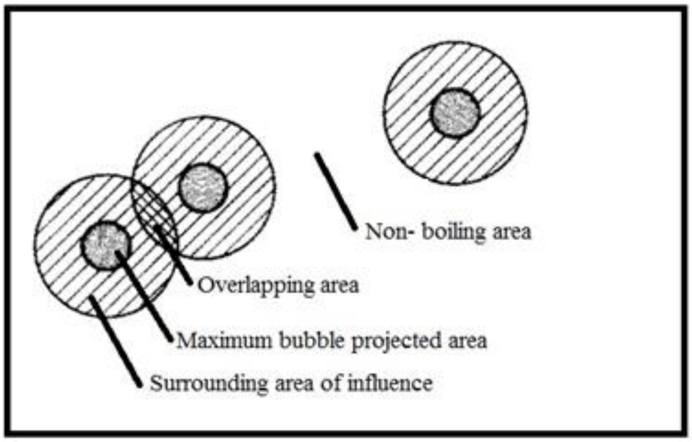

Figure 1.2: The four areas of heat transfer regions [24]

$$A = \frac{\pi}{4} D_{max}^2 N_a \tag{1.10}$$

where D_{max} is the maximum bubble diameter, and N_a is the active nucleation site density. N_a values are tabulated based on the experiments undertaken as a function of wall superheat. The wall heat flux is expressed as,

$$q_w = q_{ev} + (q_{tcb} + q_{tcs}) + q_{fc} \tag{1.11}$$

Heat transfer across the microlayer is approximated by two stages. Firstly, the microlayer evaporates as a semi-infinite bulk liquid with no effect on the wall till a certain time. Then, the temperature gradient in the microlayer is assumed to be linear.

$$q = \frac{K_l \Delta T_{sup}}{\delta_m} \tag{1.12}$$

and due to evaporation, the rate of change in the sub-layer thickness is

$$\frac{d\delta_m}{dt} = -\frac{K_l \Delta T_{sup}}{\rho_l h_{fg} \delta_m} \tag{1.13}$$

After bubble collapse, the mean transient conduction heat transfer for one bubble cycle can be defined as,

$$q_{tc} = \frac{2K_l(\Delta T_{sup} + \Delta T_{sub})}{\sqrt{\pi \alpha_l t_{tc}}} \tag{1.14}$$

Del Valle and Kenning [24] introduced two coefficients: Y to express the area of influence relative to bubble area, and fraction X to express the true boiling area to the nominal area. The difference between true boiling area and nominal area is due to the overlap between the areas of influence of the different nucleation sites; thus, the non-boiling area is expressed as $1 - XYF$, and the area of influence without overlapping is expressed as $(2X - 1)YF - F$. Due to the combined effect of two bubbles, the heat flux extracted from the overlapped area is $4/3$ the flux obtained from Eq. (1.14). The share of the microlayer evaporation component in the total wall heat flux Eq. (1.11) is $2 - 3\%$, single phase heat component 10%, and as less as 5% in case of high heat fluxes. The rest of the heat is due to the quenching heat flux component, either in the area of influence or bubble projected area.

Although Del Valle and Kenning [24] introduced a basic model for wall flux partitioning, they relied on experimental observations to determine bubble radius, active sites density, bubble frequency and bubble influence area. They took into account the overlapping between two nucleation sites only, which caused a limitation when applying their model in a dense nucleation-site surface where overlapping occurs between multiple sites.

Kurul and Podowski [25] studied heat flux in subcooled flow boiling, and divided the wall heat flux into three components: single phase, transient, and evaporation heat flux. Convective heat flux is calculated over area, A_{fc}, where there are no bubbles. It is expressed as,

$$q_{fc} = A_{fc}\, \rho_l\, C_{p,l}\, U_l\, St\, (\Delta T_{sup}) \tag{1.15}$$

where A_{fc} is the area influenced by forced convection, U_l is flow velocity and St is Stanton number. The transient conduction heat flux component is evaluated based on Del Valle and Kenning [24] model. The area of the heater where transient conduction is dominant, A_{tc}, is expressed as,

$$A_{tc} = Y N_a \frac{\pi D_l^2}{4} \tag{1.16}$$

where Y is the area of influence relative to bubble area and D_l is the lift-off diameter. The three components are evaluated independently and summed to get the total wall heat flux. Though, they did not account for the overlapping influence area between nucleation sites.

Basu et al. [26, 27] developed a mechanistic model for flow boiling in vertical conduits. It is assumed that all the heat from the surface is transferred to the adjacent superheated liquid layer. The heat is then transferred to the bulk liquid and to the evaporated liquid at the interface. Multiple heat transfer mechanisms may be present at a time, depending on the bubbles state: stable, growing, sliding, collapsing or departing from the surface.

Using the same concept for area partitioning as Del Valle and Kenning [24], Basu et al. [26] assumes that heat transfers to the adjacent superheated liquid layer. A fraction of the heat flux is used to evaporate bubbles while the rest is transferred to the bulk liquid. Heat flow representation is shown in Fig. (1.3). Basu divided the flow region to (i) upstream of ONB, (ii) between ONB and onset of significant void (OSV), and (iii) downstream of OSV. Upstream of ONB, all the energy is moved to the bulk liquid by forced convection. Hence, the heat flux is given by

$$q_w = q_{fc} = h_{fc}\left(\Delta T_{sup} + \Delta T_{sub}\right) \tag{1.17}$$

While in the region between ONB and OSV, where there are attached bubbles on the surface, the heat is transferred by single-phase forced convection with an enhanced heat transfer coefficient because of the effect of the bubbles on the surface. Enhanced

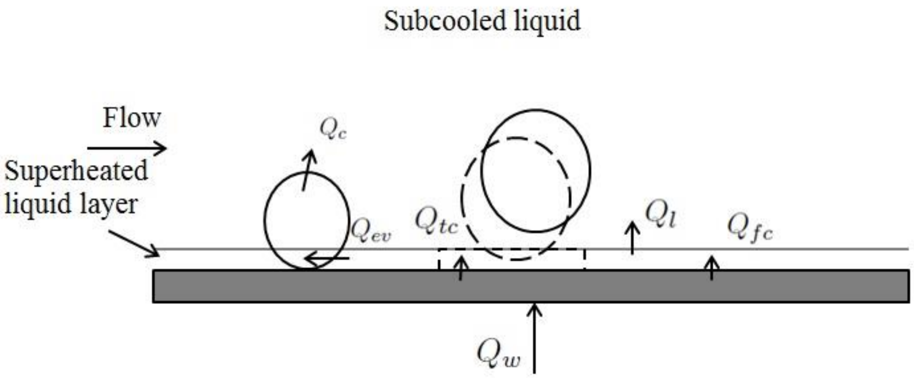

Figure 1.3: Representation of heat flow path [28]

forced convection is expressed as,

$$q_w = q_{fc} = \bar{h}_{fc} \, (\Delta T_{sup} + \Delta T_{sub}) \tag{1.18}$$

The experimental heat transfer coefficient at OSV increases by 30%, $h_{\bar{fc}} = 1.3 \, h_{fc}$, compared to upstream of ONB.

Downstream of OSV, bubbles grow and depart the surface at D_d. The departed bubble slides and grows on the surface till its diameter reaches the lift-off diameter D_l. When bubbles leave the surface to the bulk liquid, they cause disturbance to the thermal boundary layer allowing bulk liquid to fill the departed bubble volume part till time t^* after which the forced convection component prevails. The wall heat flux partitioning can be expressed as,

$$q_w = q_{fc} + q_{tc} \tag{1.19}$$

$$q_{tc} = \frac{1}{t_w + t_g} \int_0^t \frac{K_l}{\sqrt{\pi \, \alpha_l \, t_{tc}}} (\Delta T_{sup} + \Delta T_{sub}) A_{sl} \, R_f \, N_a \, dt \tag{1.20}$$

where R_f is the reduction factor defined as the ratio of actual number of bubbles lifting off the surface to the number of active nucleation sites per unit area, A_{sl} is the sliding area, and

$$t = \begin{cases} t^* & t^* < (t_w + t_g) \\ t_w + t_g & t^* \geq (t_w + t_g) \end{cases} \tag{1.21}$$

where t^* is the transient conduction time, t_w is the waiting time and t_g is the growth time. Heat is transferred by forced convection over the area

$$A_{fc} = \begin{cases} 1 - A_{sl}\,R_f\,N_a & for \quad t = t^*/(t_w + t_g)) \\ A_{sl}\,R_f\,N_a & for \quad t = 1 - (t_w + t_g) \end{cases} \tag{1.22}$$

To be able to find a closure for their model, Basu et al. [26] needed to determine the locations of ONB and OSV in order to partition the surface correctly. Submodels for N_a, D_d, D_l, t_w, and t_g, f were needed to find closure for the wall heat flux partitioning. Although the experiments were well controlled, the applicability of the developed submodels was limited to flow boiling in a vertical conduit.

1.1.2.2 Wall heat flux partitioning: jet impingement boiling

The wall heat flux partitioning models mentioned earlier are developed for subcooled flow boiling. Omar [18] studied jet impingement subcooled nucleate boiling under steady-state conditions. He developed a partitioning model for jet impingement boiling for jet velocities ranging from 0.4 m/s to 1.7 m/s and degrees of subcooling from 10 to 28°C. The model is valid for the stagnation region as well as the parallel flow region. Omar adopted the same assumptions as Basu et al. [26], where heat is transferred to the superheated liquid layer, as shown in Fig. (1.3). Omar assumed single phase heat transfer till ONB. After ONB, a significant enhancement in single phase component occurs due to the turbulence induced by bubbles attached to the surface. The enhancement factor, η, is modeled as a function of the nucleation site density and is given by,

$$\eta = \left(\frac{N_a}{10^5}\right)^{0.15} \tag{1.23}$$

The wall heat flux is partitioned into two components: single phase convection and transient conduction. Omar took into account the bubble state. The bubble either slides on the heated surface before departure or departs at the nucleation site. The possible bubble merge during sliding or due to the spacing between active nucleation sites was not considered, as no experimental data was available due to the small size of the heating surface. A bubble growth termination scenario model was developed to determine bubbles state. The bubble may collapse at its site or grow and slide then collapse. He calculated the maximum diameter based on both thermal and dynamic equilibrium. He used intrusive (fiber optic probe) and non intrusive methods (high speed imaging) to collect information about the bubble dynamics. To find a closure for his model, Omar also modeled the onset of nucleate boiling, ΔT_{ONB}, bubble frequency, f, nucleation site density, N_a, and growth and waiting time, t_g and t_w based on experimental data. The wall heat flux partitioning components are shown in Fig.(1.4).

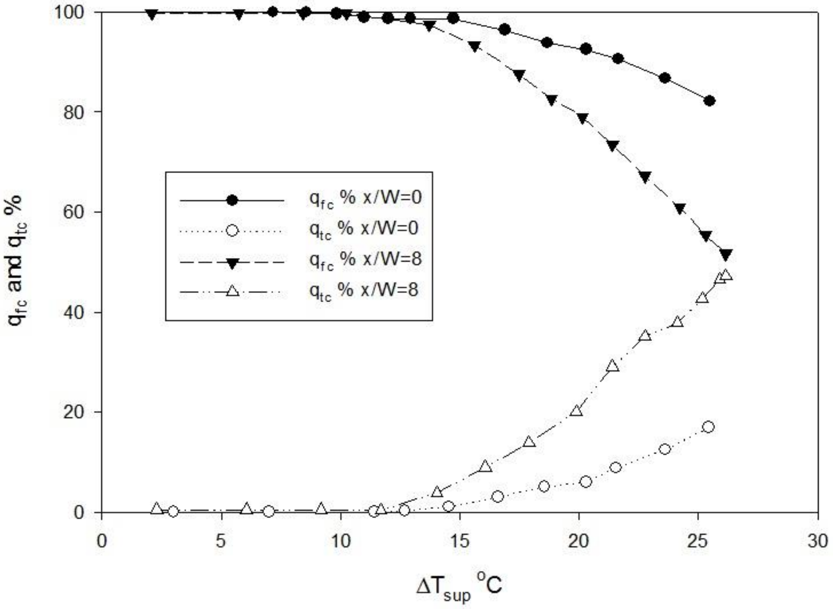

Figure 1.4: Wall heat flux partition at the stagnation region x/w=0 and at x/w=8 [18]

Out of all the closure submodels, determining the bubble departure diameter is the most important one. Heat flux models are greatly dependent on the area occupied by the bubbles or affected by its presence. Bubble equilibrium diameter is a balance between the number of forces acting on the growing bubble. The next section presents a review of bubble growth models and forces considered on a growing bubble.

1.1.3 Bubble Dynamics

1.1.3.1 Bubble growth models

Once the bubble embryo is formed, the bubble growth is characterized by the momentum interaction between the growing bubble and the surrounding liquid, i.e. inertia forces. As the bubble grows, heat diffusion comes into play till the growth is completely controlled by heat diffusion. The transition between the two growth mechanisms is smooth with no sudden changes in growth rate or size [29]. For example, at low pressure boiling, the growth is mainly controlled by inertia forces. While at high pressure, bubble growth is predominately controlled by heat diffusion [30].

Momentum growth controls bubble growth in the early stages. It was leveraged early as a description of spherical bubbles growing in a superheated liquid bath. By assuming potential flow, the solution of the liquid momentum equation around the bubble was found by Rayleigh [31]. The relation between bubble growth rate and pressure difference is expressed as,

$$\frac{P_v - P_\infty}{\rho_l} = r\,\ddot{r} + 1.5\,\dot{r}^2 + \frac{2\sigma}{\rho_l\, r} \tag{1.24}$$

where p_v is the vapor pressure, p_∞ is the surrounding liquid pressure, r is the bubble radius, and $\dot{r}$ is the rate of change in bubble radius.

Eq. (1.24) shows the balance between the net pressure forces on the bubble and surface tension forces. The pressure inside the bubble is coupled with the temperature of the vapor. Eq. (1.24) can not be solved alone and the energy equation is required to find the bubble radius. However, the equation can be solved with no dependency on the energy equation at the initial stages of bubble growth; the superheated liquid layer energy is not yet consumed and the rate of vapor generation is not the limiting factor in bubble growth [32]. The solution for Eq. (1.24) in the early stages of bubble growth is

$$r = c\,t \tag{1.25}$$

where c is a constant and t is growth time.

Mikic et al. [30] studied bubble growth in a uniformly superheated liquid. They developed a simple relation for bubble growth, and equated the work done by an expanding bubble to the kinetic energy of the liquid mass. Combining the previous result with the linearized Clausius-Clapeyron equation, the obtained equation is similar to Rayleigh solution, Eq. (1.25), by inertia forces. Although a different approach was used, the same conclusion of linear growth at the early stages was drawn.

With advancement in bubble growth time, heat diffusion growth is significant. The bubble growth depletes energy from the superheated layer resulting in a decrease in the vapor temperature. Hence, the growth rate decreases as bubble growth is controlled by the slow heat diffusion. Plesset and Zwick [32] studied bubble growth in superheated liquids. They developed a relation for bubble radius in superheated liquid based on the assumption of thin thermal boundary layer. Combining the assumption with

Eq. (1.24), the instantaneous bubble radius can be expressed as,

$$r = 2\sqrt{3}\, Ja_{sup} \sqrt{\frac{\alpha t}{\pi}} \tag{1.26}$$

where Ja is Jakob number, and α is the thermal diffusivity.

Zuber [33] solved the one dimensional, transient heat conduction problem for uniform temperature field and non-uniform temperature field as follows,

$$r(t) = b\sqrt{\frac{\alpha t}{\pi}}\, \frac{\Delta T C_p\, \rho_l}{h_{fg}\, \rho_v} \left[1 - \frac{q_b \sqrt{\pi \alpha t}}{2K\, \Delta T}\right] \tag{1.27}$$

where b is a constant, k is liquid thermal conductivity and q_b is the heat flux to the bulk liquid. q_b vanishes when the temperature is uniform around the bubble or when the bubble is just departing the nucleation site after reaching its maximum diameter. Then Eq. (1.27) is expressed as,

$$r(t) = 2bJa_{sup} \sqrt{\frac{\alpha t}{\pi}} \tag{1.28}$$

While Zuber model was developed only for diffusion growth, Mikic et al. [30] developed a bubble growth model applicable to the whole range of bubble growth, including both inertial and diffusion for uniformly and non-uniformly superheated liquid. It assumes bubble growth starts from $r = 0$, rather than from the critical radius, r_c. Their model, in a nondimensional form for a non-uniform temperature field, can be written as,

$$
\begin{aligned}
r^{+}(t) =& t^{+0.5}\left(1-\theta\left[\left(1+\frac{t_w^{+}}{t^{+}}\right)^{0.5}-\left(\frac{t_w^{+}}{t^{+}}\right)^{0.5}\right]\right) \qquad (1.29)\\
t^{+} =& \frac{A^2\,t}{B^2}\\
r^{+} =& \frac{B^2\,r}{A}\\
\theta =& \frac{T_w - T_l}{\Delta T}
\end{aligned}
$$

where A and B are related to the wall superheat as follows,

$$A = \left[b\frac{h_{fg}\,\rho_v\,\Delta T_{sat}}{\rho_l\,T_{sat}}\right]^{1/2} \qquad (1.30)$$

$$B = \left[\frac{12}{\pi}\alpha_l\right]^{1/2} Ja \qquad (1.31)$$

$$Ja = \frac{\Delta T_{sat}\,c_{pl}\,\rho_l}{h_{fg}\,\rho_v} \qquad (1.32)$$

where $b = \pi/7$ for a bubble growing on a surface, and t_w^{+} is the nondimensional waiting time. The waiting time is often assumed to be equal to the bubble growth time, while the inverse of the sum of both times gives the bubble release frequency. Mikic et al. [30] collected waiting time data from the experiments carried out to measure the diameter, and found that for $t^{+} \ll 1$, $r \sim t$ (inertial growth), while at $t^{+} \gg 1$, $r \sim \sqrt{t}$ (Heat diffusion growth).

Colombo and Fairweather [34] studied bubble departure in forced convection boiling, and developed a new relation for bubble growth during flow boiling as bubble growth is essential to bubble departure models. They described the bubble growth as the sum of different components, each representing a physical mechanism. While the classical models only considered the effect of evaporation from the superheated layer and condensation to the bulk liquid, Colombo and Fairweather [34] considered the macro-layer evaporation under the bubble as well. The relation is similar to expressions previously developed [33] except for the added macro-layer evaporation component. Bubble growth is expressed as,

$$\frac{dr(t)}{dt} = \left.\frac{dr(t)}{dt}\right|_{mae} + \left.\frac{dr(t)}{dt}\right|_{sup} + \left.\frac{dr(t)}{dt}\right|_{sub} \tag{1.33}$$

$$\left.\frac{dr(t)}{dt}\right|_{mae} = c_1\, Pr^{-1/2}\, Ja \left(\frac{K_l}{\rho_l Cp\, t}\right)^{1/2} \tag{1.34}$$

$$\left.\frac{dr(t)}{dt}\right|_{sup} = b\, k_l \Delta T_{sup}) \left(\frac{3}{\pi}\frac{K_l}{\rho_l\, Cp\, t}\right)^{1/2} \tag{1.35}$$

$$\left.\frac{dr(t)}{dt}\right|_{sub} = (1-b)\frac{h_c}{\rho_v h_{fg}}\Delta T_{sub}) \tag{1.36}$$

where Pr is Prandtl number, c_1 is a constant, h_c is the condensation heat transfer coefficient, and b is the ratio of bubble volume immersed in the superheated liquid.

1.1.3.2 Bubble termination mechanism

The growth and departure of the bubble attached to the heater surface is a complex process engaging both energy and momentum exchange between the growing bubble and the surrounding liquid. The momentum equation for the growing bubble can be expressed as follows,

$$\sum F_y = \rho_v V_b \frac{d\, u_{bcy}}{dt} \tag{1.37}$$

where V_b is the bubble volume and u_{bcy} is the velocity of the center of mass of the bubble. The process is quasi-static since the acceleration of the vapor bubble for most cases, the right hand side, is negligible when the bubble is attached to the surface and $\rho_l >> \rho_v$. The term $d\, u_{bcy}/dt$ is finite at bubble departure. Hence, the quasi-static condition, $\sum F_y = 0$, is violated at the moment of departure [35, 36].

There are four probabilities for bubble termination, shown in Fig. (1.5), for any bubble attached to the surface. The bubble will either (i) stay stagnant, (ii) collapse (condense), (iii) lift-off into the bulk liquid or (iv) slide on the heated surface. While the first two possibilities are controlled by heat flow to the bubble by evaporation and condensation, respectively, the latter two possibilities are controlled by the balance of forces acting on the bubble.

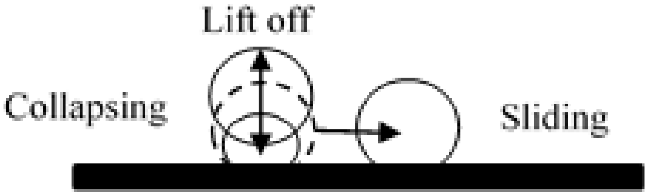

Figure 1.5: Bubble four termination possibilities

VanHelden et al. [37] experimentally studied bubble detachment and forces acting on a bubble. The bubble was nucleating from a designed cavity on a heated surface in a vertical flow conduit. Five forces were taken into account: surface tension, hydrodynamic force (Lift), thermal gradient force, expansion force (Rayleigh equation for dynamic pressure) and buoyancy force. The bubble detaches from the heater surface when the RHS of the momentum equation (Eq. (1.37)) is greater than the standard deviation of the force balance. Lift, expansion and buoyancy forces vary with the radius of the growing bubble. On the other side, thermal gradient force and x-component surface tension force are almost constant with the radius.

Thorncroft et al. [38] carried out an experimental study for upward and downward vertical flows. From visual observations, most of the bubble growth occurred during bubble sliding on the heated surface, while a small portion occurred while the bubbles were attached to the nucleation site. Lift-off is noticed in the case of downward flow, while departing (sliding along the surface) was noticed in case of upward flow. Shear lift forces are hypothesized to push the bubble against the wall. Results showed that bubble sliding enhanced the rate of heat transfer. The heat transfer coefficient in the upflow was noticeably higher than downflow at the same testing conditions.

Klausner et al. [39] investigated bubble departure in a specially manufactured flow boiling channel. The bubble has been observed to slide along the heated surface after departing from the nucleation site. The bubble slid on the surface for a finite distance before it lift-off. They plotted a probability density function of departure diameter for 200 bubbles covering a wide range of flow boiling conditions. They showed that the increase in mass flux resulted in a decrease in bubble departure diameter which can be directly attributed to the quasi-static drag forces. The measured bubble diameter showed dependency on the mass flux and heat flux. An increase in the heat flux resulted in an increase in the bubble departure diameter. However, an increase in the mass flux resulted in decrease in the departure diameter.

Many researchers adopted Klausner force model to estimate bubble departure diameter and bubble growth diameter [34, 40]. Klausner et al. [39] considered different force components acting on a growing bubble as shown in Fig. (1.6).

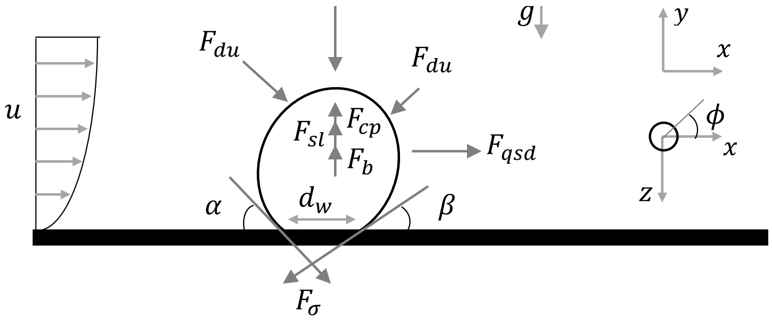

Figure 1.6: Forces acting on a growing vapor bubble in flow boiling [39]

The x-direction and y-direction force balance is expressed as,

$$\sum F_x = F_{\sigma,x} + F_{qsd} + F_{du,x} \tag{1.38a}$$

$$\sum F_y = F_{\sigma,y} + F_{du,y} + F_{sl} + F_h + F_{cp} + F_b \tag{1.38b}$$

where F_σ is the surface tension force, $F_q sd$ is the quasi-steady drag force, F_{du} is the unsteady growth force, F_{sl} is the lift created by the flow, F_h is the hydrodynamic force, F_{cp} is the contact pressure force, and F_b is the buoyancy force.

From the force balance, Klausner et al. estimated the bubble departure diameter and the scenario of bubble termination that will prevail. Determining the bubble diameter under an impinging jet is essential for a wall heat flux mechanistic model.

Omar and Hamed [41] were the first to study bubble growth in the parallel flow region of a free impinging jet. The jet velocity ranged from 0.4 to 1.7 m/s and degrees of subcooling from 10 to 28 °C. They decoupled the thermal and dynamic effect on bubble growth. Bubble departures the surface at minimum bubble diameter attained from (i) the thermal equilibrium and (ii) the dynamic equilibrium.

Thermal equilibrium determines the bubble diameter based on the balance between the heat flowing to and from the bubble. When the two components equate, the bubble diameter reaches equilibrium. Dynamic equilibrium model determines the bubble diameter based on the balance of forces on the bubble. Similar to Klausner et al. [39], Omar and Hamed [41] considered the drag force, growth force, buoyancy force and shear lift force. Surface tension force was found to have an insignificant effect on bubble departure diameter.

Decoupling thermal and dynamic effect is an idealistic approach for bubble growth under impinging jet. It simplifies the determination of departure diameter by considering each case independently. A more accurate approach is that bubble growth is controlled by thermal equilibrium while departure is controlled by net forces on the bubble. There is a limited number of studies on bubble growth in the stagnation region of impinging jets.

1.2 Transition Boiling

While nucleate boiling is the most favorable operating mode due to its predictability, transition boiling is the least favorable due to the deterioration in the rate of heat transfer. Studies of transition boiling are limited because of the inherent instability (negative slope of the boiling curve) and the technological challenges of carrying out the experiments. The following section provides a brief summary of the studies focusing on transition boiling under an impinging jet.

Ishigai et al. [9] studied the effect of planar-jet velocity ($0.65 - 3.5\,\mathrm{m/s}$) and degree of subcooling ($5 - 55\,^{\circ}\mathrm{C}$) on stainless steel quenching at temperatures up to $1000\,^{\circ}\mathrm{C}$. The transient boiling curves for high degrees of subcooling ($\Delta T_{sub} > 25\,^{\circ}\mathrm{C}$) showed that the heat flux did not reach the CHF point directly from the Leidenfrost point. However, the heat flux went through a plateau of heat flux that was not observed at lower degrees of subcooling, as shown in Fig. (1.7). They concluded that the degree of subcooling was the main driver for the plateau in the heat flux (shoulder heat flux). The higher the subcooling, the higher the shoulder heat flux. The degree of subcooling also affected the range of degrees of superheat at which the shoulder was observed. The jet velocity slightly shifted the shoulder heat flux up, yet it was not the prime cause.

Miyasaka et al. [10] carried out steady-state boiling experiments at the stagnation point of a planar jet at high degrees of subcooling ($\Delta T_{sub} = 85\,^{\circ}\mathrm{C}$) and jet velocity ranges from 1.5 to 15 m/s. They noticed two modes of boiling after the CHF, namely:

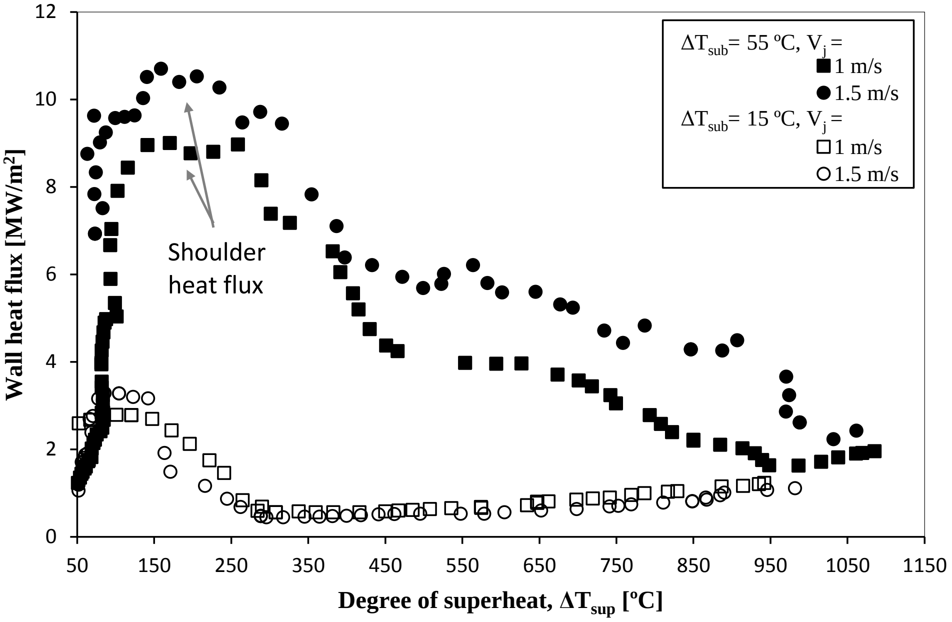

Figure 1.7: Boiling curve for a planar water jet [9]

(i) the first and (ii) the second transition regions, as shown in Fig. (1.8). The first region, subsequent to the CHF, witnessed a heat flux increase with the increase in the degree of superheat. The second region was characterized with a constant heat flux despite the increase in the surface temperature. Although they experimented with different jet velocities, they observed the same boiling curve shape; however, the boiling curve was shifted up at higher jet velocities.

Years later, Robidou et al. [42] experimentally obtained the boiling curve for a planar water jet in the stagnation and the parallel flow region for degrees of subcooling ranging from 7 to 17 °C and jet velocities of 0.7 and 0.8 m/s. They carried out controlled surface-temperature steady-state experiments covering the transition boiling regime. They observed a local minimum in the heat flux within the transition region, as shown in Fig. (1.9), after which an increase in the heat flux was reported. The heat flux then reached a plateau even with the increase in the surface degree of superheat. They

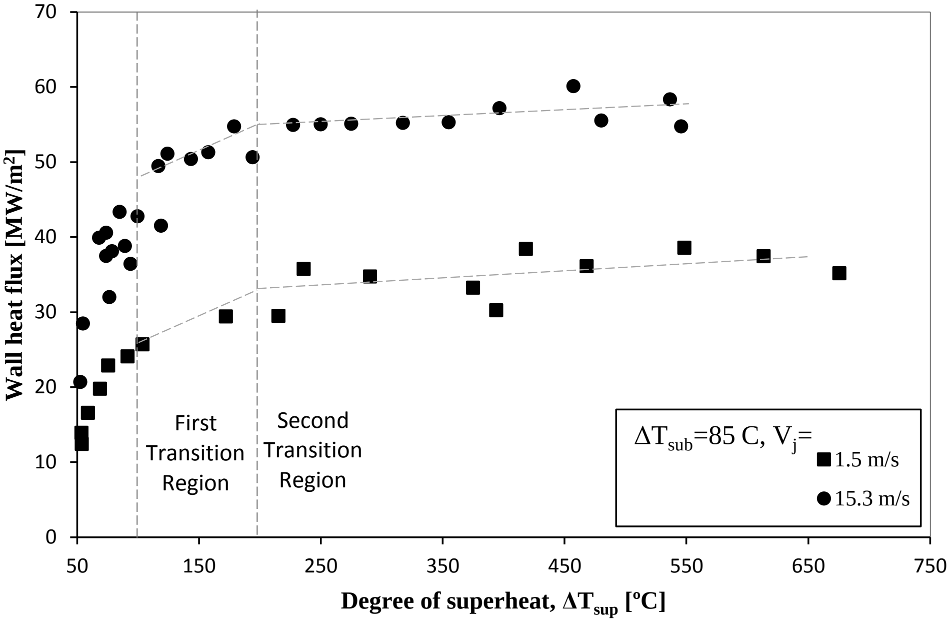

Figure 1.8: Boiling curve for a planar water jet [10]

attributed the occurrence of the shoulder heat flux to the break up of the coalesced bubbles (i.e., the vapor blanket) that formed at the CHF into smaller bubbles, known as Microbubble Emission Boiling (MEB) [43].

Suzuki et al. [44], Suzuki [45] investigated microbubble emission boiling in small channel flow boiling. They concluded that at low degrees of subcooling (10 °C), the wall heat flux beyond the CHF decreased, while it increased at higher degrees of subcooling (20 − 30 °C). They also reported the same conclusion with the flow velocity; at higher flow velocities, the MEB generation was higher than in the case of low flow velocities. Both the flow velocity and the degree of subcooling accelerated the defragmentation of the coalesced bubbles into microbubbles, and hence the extracted heat flux beyond the CHF increased.

Gradeck et al. [46] studied quenching of stationary and moving surfaces with impinging jets in both stagnation and parallel flow regions. For stationary cylinders,

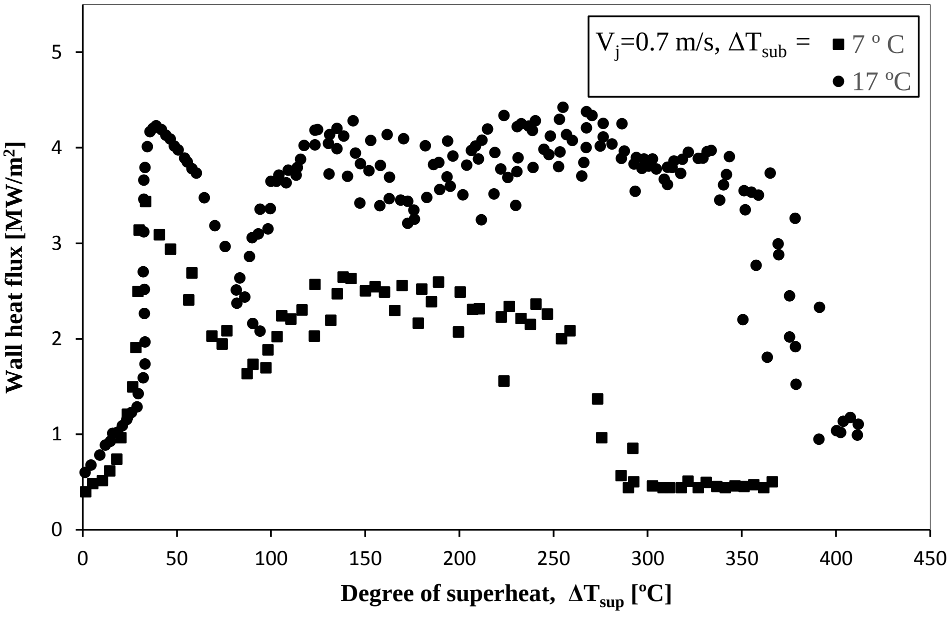

Figure 1.9: Boiling curve for a planar water jet [43]

the shoulder heat flux was observed in the stagnation region. The range of superheat, over which the shoulder heat flux was observed, depended on the degree of subcooling. Once the surface started to move, the shoulder heat flux decreased and it was not observed at high surface velocities.

The previous studies present experimental data and observations of transition boiling under an impingement jet. However, such studies lack the physical explanation of the shoulder phenomenon based on experimental observations. A few studies physically modeled the shoulder heat flux based on hypothesis or macro level observations. Seiler-Marie et al. [47] hypothesized that jet momentum is the main cause of vapor layer break up and the periodic bubble oscillation is the main cause of the shoulder heat flux. They assumed that once the jet breaks up the vapor layer, liquid comes into contact with the surface. The liquid is heated by transient conduction till the phase changes and the generated vapor evicts the liquid. The vapor layer was assumed not to grow beyond a certain critical length; it is equal to the critical wavelength of Rayleigh-Taylor instability. Their expression of the critical wavelength did not account for the effect of the heat and mass transfer along the interface. Instead, they estimated it based on the classical Rayleigh-Taylor instability analysis.

Based on the experimental data obtained by Robidou et al. [42], Seiler-Marie et al. [47] proposed a model for the first minimum, Eq. (1.39), and the shoulder heat flux, Eq. (1.40). Because of the lack of experimental measurements, the frequency of the vapor break up was correlated to a time scale, given by Eq. (1.41), derived from non-dimensional analysis. Also, the volume of the liquid rushing into the surface was assumed to be proportional to a sphere volume ($V = K\pi D_c^3/6$) with a diameter equal to the critical wavelength with an empirical proportionality constant.

$$q_{fm} = K_l \, \frac{T_i - T_l}{\sqrt{\pi \alpha_l \tau}} \tag{1.39}$$

$$q_{sh} = \rho_l \, Cp_l \, \Delta T_{sub} \, \frac{V/\tau}{A} \tag{1.40}$$

$$\tau \simeq (\rho_l - \rho_v)^{-1/4} \, \sigma^{1/4} \, a_{tot}^{3/4} \tag{1.41}$$

where T_i is the liquid-surface interface temperature, T_l is the liquid temperature, V is the liquid volume, A is the surface area affected by bubble oscillation, and a_{tot} is the total vapor-liquid interface acceleration.

Bogdanic et al. [48] measured the liquid contact frequency and vapor structure height under the jet. They used a miniature optical probe (1.5 μm tip diameter) to distinguish between vapor and liquid on the heated surface. The observed frequency was 900 Hz at the first minimum and 2,000 Hz at the beginning of the shoulder. With the increase of superheat, liquid intrusion frequency increased to 20 kHz. Based on their measurements, they developed a simple heat flux model, and assumed that the liquid intrusions are the main contributor to the shoulder heat flux. They assumed that all the intruded liquid volume that comes into contact with the surface is evaporated. Their assumption is valid as long as the liquid maintains contact with the surface, but the liquid layer in contact with the surface evaporates and the rest of the liquid volume loses the source of energy required to evaporate. They did not define the area on the surface that is wet by the liquid. Instead, they used an empirical constant to account for all the uncertainties associated with their assumptions. Their model fits their experimental data with deviation from −38% to +16%.

1.3 Current Study Objectives

From the literature review, several attempts have been made to develop a sound mechanistic model to predict the total wall heat flux in the case of pool and flow boiling. Although the concept of wall flux partitioning has been extensively used, only a few trials aim to find a mechanistic model for jet impingement boiling. The current work paves the road to a sound mechanistic model of nucleate and transition boiling under an impinging jet.

1.3.1 Nucleate Boiling

Omar [18] modeled impingement jet nucleate boiling based on the wall heat flux partitioning approach developed by Basu [28] for flow boiling. Omar's model is dependent on bubble diameter. Hence, an accurate force balance model is essential to estimate bubble departure diameter in the stagnation region.

The current work is intended to fill the gap in the area of bubble dynamics for accurate nucleate boiling wall heat flux partitioning. The following are the current study objectives for nucleate boiling:

- Develop a force balance model for bubbles growing in the stagnation region to estimate bubble departure diameter. Earlier work done by Omar and Hamed [41] considered bubbles growing in the parallel flow region of the jet. More attention is given to the stagnation region in the current work, as flow dynamics in the parallel flow region are obviously different from those in the stagnation region. The model is validated with experimental data collected.

- Implement a bubble growth model for a bubble growing in the jet stagnation region and in the parallel flow region. Bubble growth is crucial for evaluating forces acting on a bubble. For example, asymmetric bubble growth forces are dependent on instantaneous bubble diameter, liquid-vapor interface velocity and acceleration. Different bubble growth models from the literature are reviewed to best represent the data collected experimentally.

1.3.2 Transition Boiling

Seiler-Marie et al. [47] and Bogdanic et al. [48] modeled the impingement jet transition boiling, but their models lacked the physical understanding of the transition boiling shoulder. No physical observations were used to support the current understanding. As a result, existing models are simple and lack the physical representation of the shoulder boiling phenomenon. The current work aims to overcome transition boiling limitations as follows:

- Explain the transition boiling shoulder heat flux based on visual observations. Previous studies hypothesized the physical mechanism behind the shoulder heat flux, but lacked observations confirming or invalidating their hypothesis [43, 47].

- Explain vapor layer break-up in the lights of Rayleigh-Taylor instability with heat and mass transfer. As vapor and liquid are configured in a way that promotes RT instability, it has been of interest to many researchers. Yet, the combined effect of mass and heat transfer was not considered.

- Develop a mechanistic wall heat flux partitioning model in the stagnation region. Wall heat flux is highly dependent on vapor layer break-up frequency. Current models either lack the break-up frequency measurements [47] or base modeling on simple relations [48].
- Measure and model vapor layer break-up frequency. Only one study by Bogdanic et al. [48] measured the frequency of surface wetting (vapor break-up). They collected the data for just one experiment using a fiber optic probe. The current study intends to extend the number of frequency measurement experiments and develop a model for the break-up frequency.

1.4 Thesis Outline

The current work presents a study of both nucleate and transition boiling under an impinging jet. Chapter 2 discusses the test loop and the advances in building the test section for both stagnation and parallel flow regions. Chapter 2 shows a new etching technique for the fiber optic probe used in the current study. Chapter 2 includes a detailed description of all the equipment used in this study along with the validation procedure of the engineering methods used to obtain the experimental measurements.

Chapter 3 discusses bubble dynamics in the case of nucleate boiling, while Chapter 3 introduces a force balance on bubbles under an impinging jet. A bubble growth model has been implemented as a submodel to estimate the bubble departure diameter.

Chapter 4 discusses the steady-state controlled surface-temperature experiments that have been carried out to investigate transition boiling under a planar water jet impinging on a flat surface. A series of high speed images of the vapor layer during its formation and break up has been analyzed. The significance of Rayleigh-Taylor instability has been studied, taking into consideration the effect of heat and mass transfer. A wall heat flux partitioning model has been proposed and validated.

Chapter 5 discusses the procedure taken to analyze the fiber optic probe signal and how the frequency, void fraction, and contact times are determined. New models for the contact frequency and vapor structure height have been proposed based on the current understanding of the jet impingement transition boiling shoulder phenomenon.

Chapter 6 provides a discussion of the work done and recommendations for future work.

Chapter 2

Experimental Setup

Different measurement techniques and tools have been used to achieve the objectives of the current study. This chapter discusses the flow loop, with the fitted connections and components; the test section (heater assembly), with a description of the control logic and the materials used to achieve high temperatures and heat flux on the surface; fiber optic probe new etching technique and its validation; high speed camera setup and settings; inverse heat conduction code used to estimate heat flux and surface temperatures; and thermocouples selection and calibration.

2.1 Flow Loop

A 60 L of distilled water is heated in a stainless steel tank at atmospheric pressure. The tank is fitted with a 3 kW thermostatic control Chromalox immersion heater in the lower half of the tank. A tank lid secures the top of the tank and guarantees minimal vapor loss.

A 1.5" suction outlet is fitted in the tank below the heater but away from the tank bottom to avoid deposits in the tank. The suction line is connected to a Y-strainer before the pump to insure no solid particles exists in the water. The suction outlet is 4" above a centrifugal pump level to ensure the pump is always covered with water. The tank water level is 2 ft higher than the pump to avoid cavitation in the pump.

The 1/2 HP centrifugal pump (Ebara CDU 200) is used to pump the heated water 2 m above the suction level. To avoid any fluctuations in the flow, the pump discharge line is fitted with an accumulator at the highest point in the flow loop. The pump is equipped with a by-pass line for better control of the system flow. Water circulation ensures homogeneity of the heated water and avoids any stratification in the water tank.

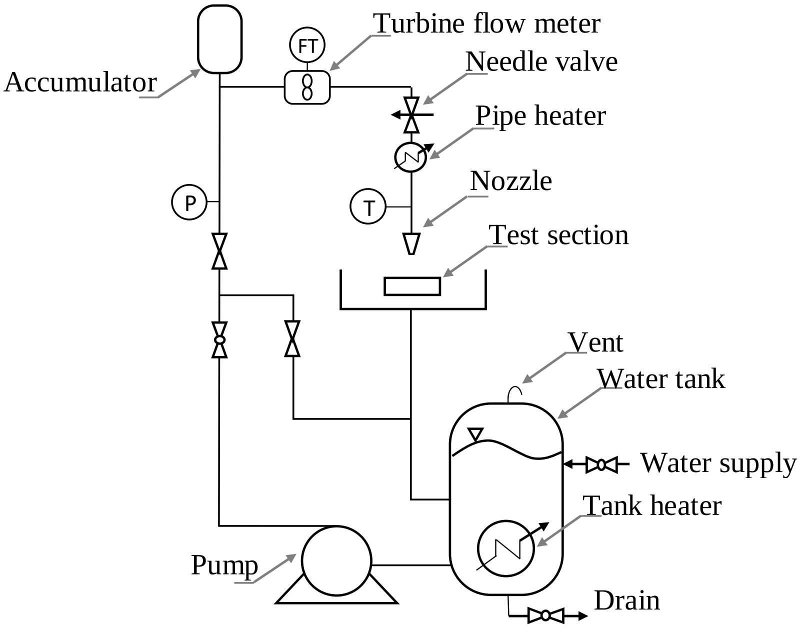

Figure 2.1: Experimental test loop

The loop, shown in Fig. (2.1), is fitted with a pressure gauge, to measure the line pressure; a water valve, to finely adjust the water velocity; a strap electric heater, to control the water temperature at the nozzle; a thermocouple, to measure the jet temperature at the exit; and a turbine flow meter, to measure the water flow rate. The water then flows through a 1-mm wide, 8-mm long planer nozzle producing a planar jet. The jet impinges the heated surface in the middle. The water is then collected and returned to the water tank.

2.2 Heating Block

There are two heating blocks used in this study. The first heating block is used to study nucleate boiling in both the stagnation and the parallel flow regions while the second block is used to study transition boiling just in the stagnation region.

The copper surface of the two modules and through out the current study has the same surface finish and roughness (110 nm RA). The effect of surface roughness has not been investigated.

2.2.1 Three Module Heater

A three module heater is built to achieve constant surface temperature. The copper block, shown in Fig. (2.2), is divided into three modules by four 5-mm deep slits from the bottom. The 1-mm wide slits separate between the different modules to minimize the heat transfer between the modules and to the sides. Each module is heated independently using a DC power supply.

Temperatures inside the copper block are measured using eighteen 0.5-mm K-type thermocouples. The thermocouples are inserted in 5-mm deep (half the width of the block) holes. The holes are drilled with a 0.02" drill-bit and distributed in two rows (0.5 mm and 2 mm below the surface). To maintain good contact between the heater body and thermocouples, the holes are filled with high temperature thermal oil and the thermocouples are secured in their locations with high temperature epoxy.

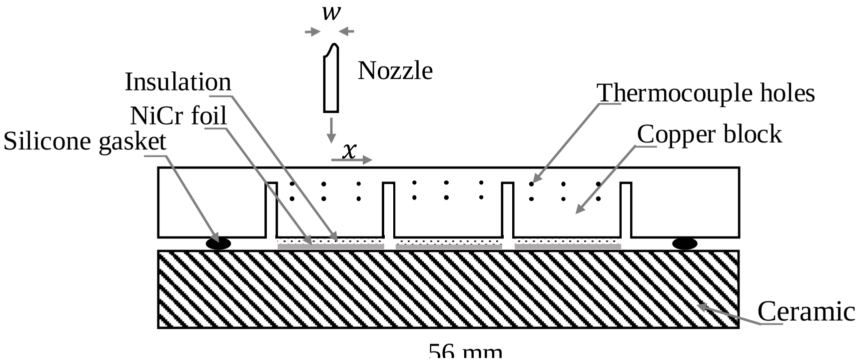

Figure 2.2: Three module heater test section

The measured temperatures are used to estimate the surface temperature and surface heat flux using an inverse heat conduction code, INTEMP. The readings of the thermocouples are collected using a NI SCXI-1102 thermocouple module with a NI SCXI-1303 construction connected to NI PCI-6601 card. NI SCXI-1303 has a built in cold junction compensation thermocouple.

Surface temperature distribution is shown in Fig. (2.3). The temperature in the middle module varies within ±0.2°C. Because of the end effect and the heat losses from the sides of the test section, there is a slope in the surface temperature in the outer halves of the first and the third modules.

Three power supplies are used to heat the copper block modules indirectly: Sorensen XG 12-140, Sorensen XG 6-110, and Xantrex XFR 12-100. They are connected to the computer using a NI GPIB-USB-HS. Each power supply has a distinct address for the communication with the computer. LabView is used to control the output of the power supplies.

The drawn current from the power supplies is used to heat a NiCr 80/20 foil by Joule effect. The foil is 25 μm thick and is cut to the size of the copper module. The NiCr foil is rested on a ceramic base, as shown in Fig. (2.2), to minimize heat loss from the bottom of the foil. The two ends of each foil are connected to two copper terminals

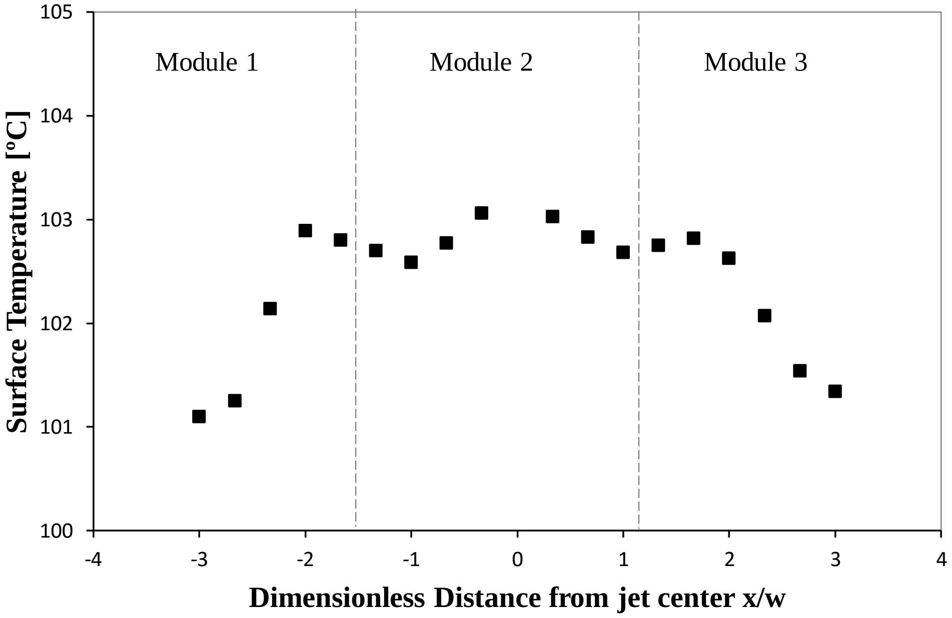

Figure 2.3: Three module heater surface temperature

which are connected to the two terminals of the DC power supply. The copper block is pressed against the NiCr foil, using spring loaded clamps, to minimize the contact resistance. A layer of thermal paste as a thermal conductor and electrical insulator is used between the copper block and the foil to avoid any possible short-circuit current through the copper block. Ultra Black RTV Gasket Maker silicone is used at all the mates to avoid water leak to the foil heater assembly.

2.2.2 Single Module Heater

To study transition boiling in the stagnation region, another heater is built to include only one heater module, as in Fig. (2.4). The single module heater is used instead of the three module heater. With this design, a maximum of 11 MW/m^2 from the foil is available. The maximum attainable surface temperature is 560 °C allowing for all the modes of the boiling regimes to be witnessed.

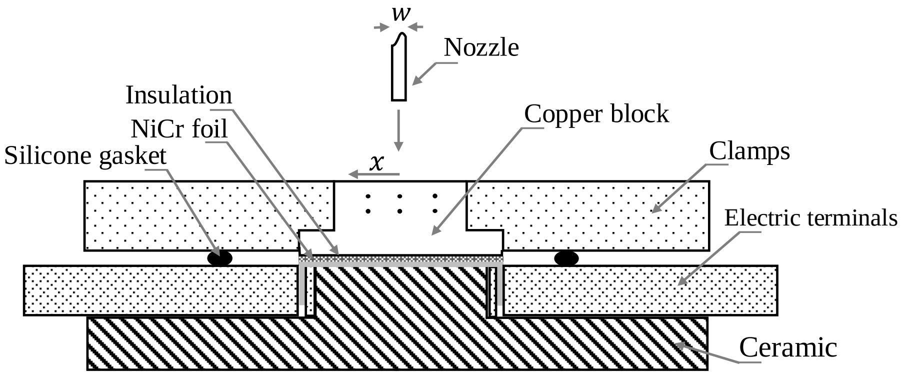

Figure 2.4: Single module heater test section

The technological challenges in the available power, control method, and the communication protocol limited the design to one heater module. The NiCr foil draws high current at voltage levels beyond the available by Sorensen XG 6-110 and Xantrex XFR 12-100. Sorensen XG 12-140 power supply is used because of its high power and ease of communication protocols. GPIB is found to take about 340 ms to communicate with the unit and change the current set point which is not fast enough to cope with the unstable nature of the transition boiling. Analog programming reduced communication time to a few milliseconds.

2.2.2.1 Control method

The single module heater is built to commence and stabilize transition boiling on the heated surface. Heat flux controlled system would cause jump in temperature which usually lead to NiCr foil burnout. Temperature controlled system is chosen to control the surface temperature. Temperature reading from the top middle thermocouple is selected to be the control variable. The controller block diagram is shown in Fig. (2.5).

It is worth noting that the process variable is the temperature measured 0.5 mm beneath the surface. The PI controller keeps this temperature around the set point

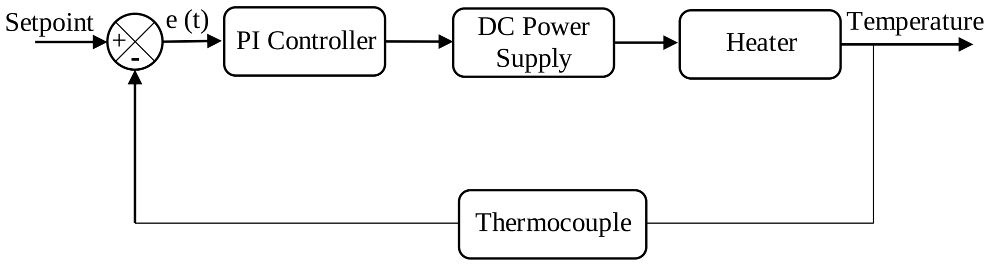

Figure 2.5: Controlled temperature heating block diagram

rather than the surface temperature. The claim that the surface temperature is controlled is valid as at each inside temperature there is a corresponding surface temperature and heat flux value as the experiments are steady-state. The obtained heat flux is related to the surface temperature after estimating the surface temperature using the inverse heat conduction problem.

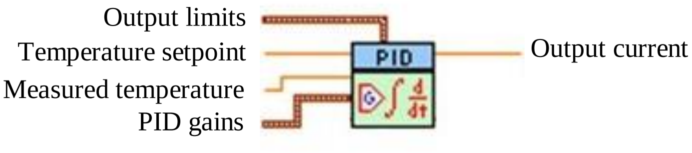

Figure 2.6: LabView PID controller

The DC power supply is controlled to achieve constant temperature using a software PI controller. A regular LabView PID controller, shown in Fig. (2.6), with no derivative component is implemented. The derivative term drives the system to instability because of the noise associated with temperature measurements [49]. The coefficients of proportional and integral terms are set based on experimental trails. There are two different sets of coefficients; the set for the nucleate boiling regime is readjusted for the transition boiling regime. The controller is adjusted to account for the fast and sudden surface temperature changes as the surface dries out.

2.2.2.2 Thermal paste selection/evaluation

The contact resistance has always been a limiting factor in high temperature heater assembly. Imperfect contact between the heat source (NiCr foil) and the copper block causes a considerable increase in the foil temperature till the point of burnout. To reduce thermal contact resistance, thermal paste is spread between the NiCr foil and the copper block. Beside good thermal conductivity and ability to fill surface irregularities, the paste must ensure electrical insulation. Physical contact between the NiCr foil and the copper block drops the electrical resistance and hence draws high current from the power supply. Four different compounds were evaluated to be used as a thermal paste:

- **OMEGATHERM 201 (OM201)**, an off-white silicone conductive thermal paste by OMEGA rated up to 200°C. It sticks to the surface, fills the irregularities and does not harden at elevated temperatures.

- **Aluminum nitride (AlN)**, known for its high thermal conductivity combined with high electrical insulation, low coefficient of expansion and thermal stability. It hydrolyzes slowly in water and hardens when dry.

- **Mix of OM201 and AlN (OM201AlN)**, experimented as it will combine between the properties of the two compounds: high thermal conductivity of AlN ($100 \sim 200$°C) and paste-like structure of OMEGATHERM 201.

- **OMEGA Heat Transfer and Release Coating (HTRC)**, a compound used for cartridge heaters at temperatures above 400°C. HTRC improves heat transfer significantly. It is water based compound with a slippery soapy texture.

The maximum safe operating temperature of NiCr 80/20 is $900\,^{\circ}\mathrm{C}$. From Fourier's law of cooling, to achieve a temperature of $400\,^{\circ}\mathrm{C}$ on the surface (assuming $5\,\mathrm{MW/m^2}$

of heat flux), the contact resistance should not exceed 10^{-4} m^{2}K/W. The contact resistance was evaluated while applying the different four pastes up to surface temperature of 140 °C.

A fast, yet reliable experimental procedure were used to estimate the thermal resistance as shown in Fig. (2.7). Based on the assumptions listed below, experiments were carried to determine which thermal paste has the lowest thermal resistance at high heat fluxes.

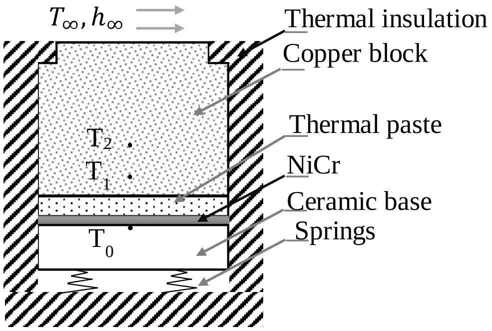

Figure 2.7: Thermal conductivity testing experimental setup

Assumptions

- NiCr foil temperature is constant across its thickness and is equal to T_0
- 1-D heat flow through the copper block
- Thermal paste of 10 μm
- Thermal resistance of copper between T_0 and T_1 is negligible compared to thermal paste thermal resistance
- Constant copper thermal conductivity

- Constant clamping force to ensure that there is no variability in the contact resistance due to clamping force

Although OM201 is rated up to 200 °C, it did not cure or experience change in properties at higher temperatures. As the paste is not soluble in water, it is suitable for jet cooling heater assembly. Although AlN has a high heat conductivity, it is water soluble. It got washed off at the sides of the heater when there was a water leak. Its performance is inconsistent. OM201AlN mix was tested for conductivity. Repetitive heating and cooling cycles were carried out to guarantee the stability of the mix and that AlN did not cure with high temperature. It was noted that the mix after the experiment has thickened, but still in the form of paste and did not harden. HTRC is suitable for this application as it is usable till 900 °C. However, HTRC is highly recommended in dry applications where the heater is not exposed to running water.

Based on the three experiments carried out, best represented in Fig. (2.8), it is found that OM201 has the lowest thermal resistance, hence lowest temperature difference between T_0 and T_1.

Although OM201 is only rated up to 200 °C, it has a stable performance at higher temperature and is used throughout this study. It was expected that the mix OM201AlN would result in the lowest thermal resistance. OM201AlN mix resulted in the highest contact resistance. It is either the AlN powder is not small enough, hence it forms relatively thick layer between the two surfaces; or it hardens at high temperatures leaving the surface not wet with the paste. HTRC contact resistance laid between OM201AlN and OM201.

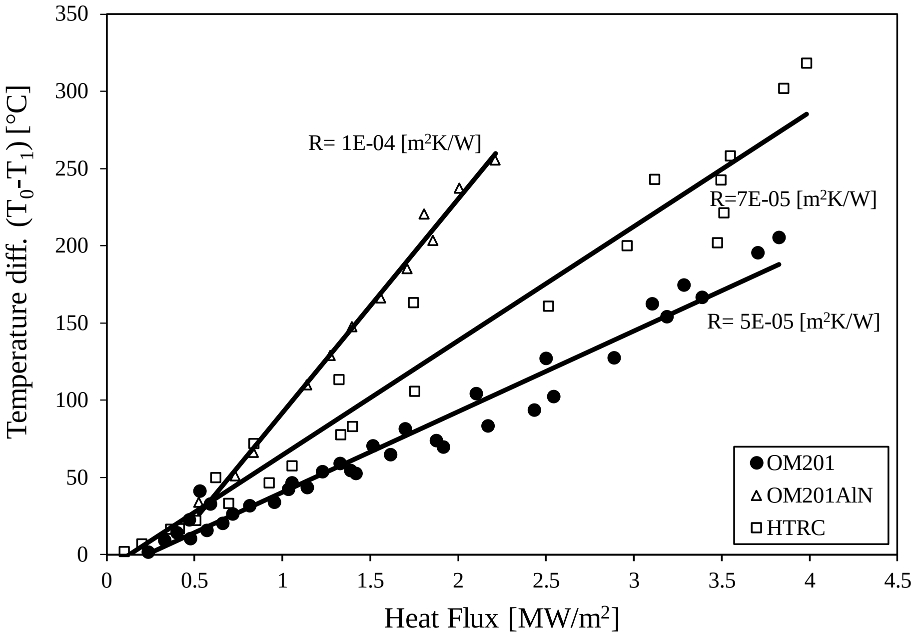

Figure 2.8: Comparison between different thermal pastes

2.3 Fiber Optic Probe

A fiber optic probe is used to differentiate between vapor and liquid in the proximity of the surface. The different index of refraction between the different phases results in light wave to be reflected internally at the tip of the fiber, while in water most of the light refracted at the tip. This difference in the reflected light wave is amplified and is used to distinguish between the two phases.

A single mode 2x2 coupler 80/20, shown in Fig. (2.9), is used with its four terminals connected to: (i) the fiber optic probe, (ii) the light-wave source, (iii) a photodiode, and (iv) the fourth end is dipped into glycerin to dissipate the signal in order not to interfere with the reflected signal from the probe tip. The single mode fiber (THORLABS-P1-SMF28E-FC) of 10.5 μm core diameter is surrounded by a 125 μm in diameter cladding material of less index of refraction to confine the light in the core.

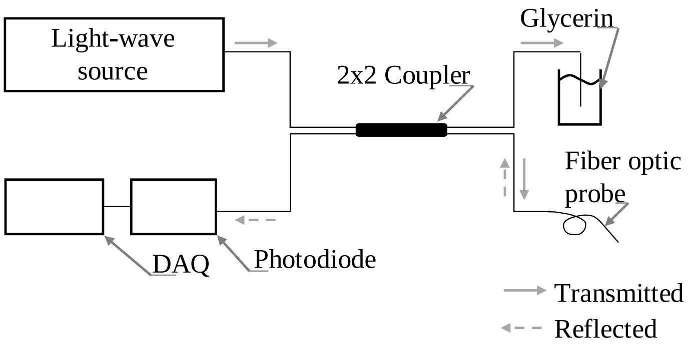

Figure 2.9: Fiber optic probe configuration

If the fiber was used directly as the probe, the size of the tip would be big enough to affect the vapor bubbles and to distort its interface under the jet. Also, as the phases changes on the probe tip and vapor comes in contact with it, liquid droplet might get attached to the tip [50]. The existence of any liquid traces gives false indication about the phase in contact with the probe. For the stated reasons, a smaller tip probe is required to minimize the interference with the vapor layer formation. Two techniques have been investigated to assess the quality of the miniaturized tip: pulling heated fiber and chemical etching.

The fiber was pulled after heating one point with a high temperature gun torch; it resulted in a very small tip with a very gradual taper. Both the cladding and the core size are reduced accordingly. The taper slope could not be controlled and it occurs over a long length of the fiber resulting in a weak fiber and higher probability of break down. The final probe is very delicate and does not have enough mechanical strength to be used under the jet.

The probe was chemically etched in hydrofluoric (HF) acid (48%). A meniscus is formed along the fiber and its height gradually drops with the reduction in the fiber diameter because of the etching. The etching process is self-terminating and known as meniscus etching [51]. If the fiber is left for long period of time, the meniscus dropped gradually resulting in a conical shape with a very small tip, as shown in Fig. (2.10-a). The tip is in order of $\phi\,1.5\,\mu$m, but it is not the only sensing part. The surface of the cone is also sensitive to the phase change till the point where cladding reflects the light internally, about $10.5 \pm 0.5\,\mu$m. The unclad (sensing) area of the probe is 100 times the area of the tip and it lies over fiber length of about $50\,\mu$m depending on the etching technique. The unclad part results in noise in the signal and it is hard to distinguish between the two phases. A different etching technique is proposed to ensure that the tip is the only sensing part of the probe.

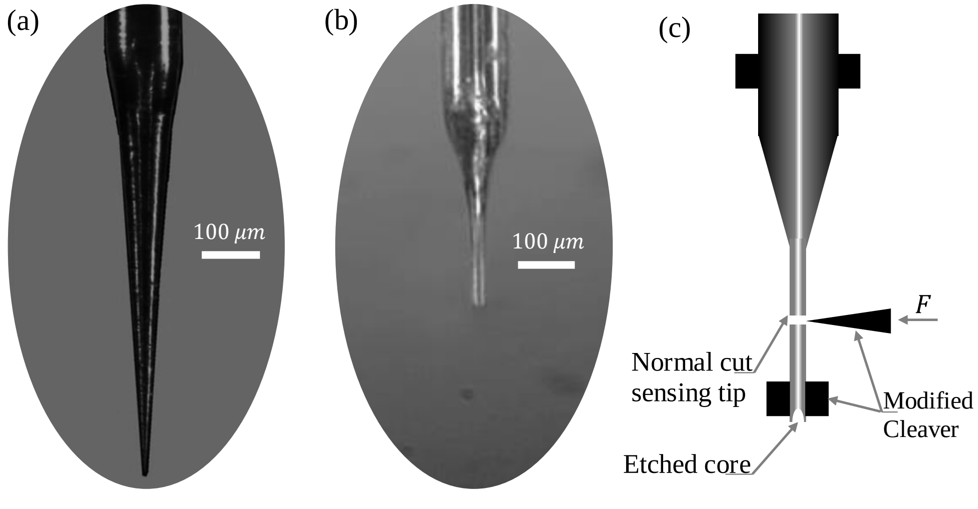

Figure 2.10: The fiber after etching: (a) cone etched, (b) the cleaved probe under the microscope, (c) cleaving process

A new etching technique is introduced to produce probe with a miniaturized sensing area. The probe is immersed in HF bath topped with a layer of paraffin oil, as shown in Fig. (2.11). As the outer layer of the probe is the cladding material, it is removed while having the same core diameter. The rate of reduction in the cladding diameter is found to be $3.75\,\mu$m/min. If the fiber is removed after 28 min, the probe diameter is reduced to 20 μm.

As HF etches the core at higher rate than the cladding, the tip becomes concave in shape and loses its normality. Therefore, the fiber is cleaved to form a normal to the axis tip. The cleaver is adjusted in the lab as shown in Fig. (2.10-c). The final cut probe, shown in Fig. (2.10-b) has a sensing area 10 times smaller than the fully conical probe (2.10-a).

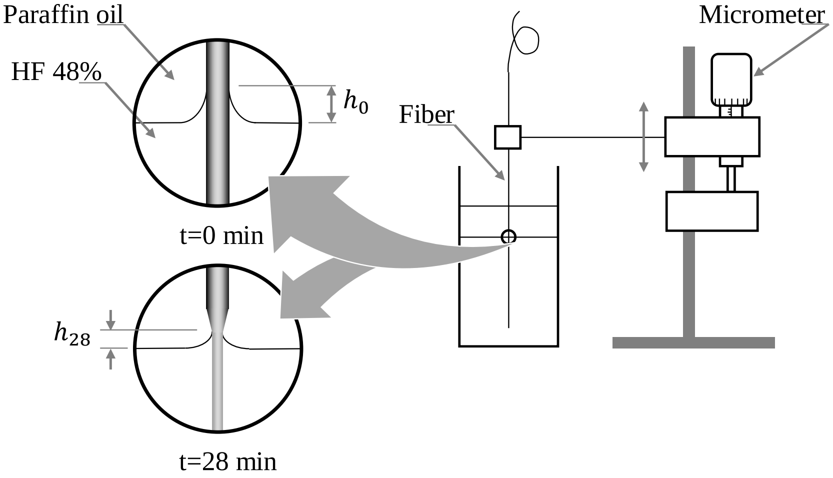

Figure 2.11: Fiber optic etching

After preparing the probe, it is attached along with a 100 μm stainless-steel wire to a stainless-steel tube of 1 mm with a high temperature glue. The distance between the two tips, of the probe and the wire, is about 270 μm, large enough not to interfere with the optical probe tip measurements. The stainless steel wire is 200 μm longer than the probe tip and it is used as a guide to the distance from the surface. The stainless-steel wire is connected to a voltage divider circuit as shown in Fig. (2.12). Both the copper surface and one end of the circuit are grounded. Once the stainless wire touches the surface, the voltmeter reads non-zero voltage. As the probe tip and the wire tip are in the same horizontal plane, then the probe tip is at a distance from the surface equal to 200 $sin\theta$ μm. A micrometer is used to move the probe vertically away from the surface at the stagnation zone. With the current probe dimensions, distinguishability of the phase is possible down to distance of $10\,\mu$m from the surface and it is moved in steps of $100 \pm 10\,\mu$m.

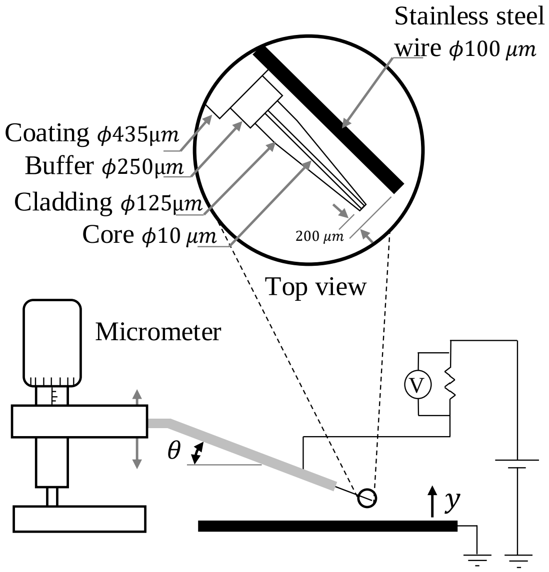

Figure 2.12: The probe in the proximity of the surface

By immersing the probe in boiling water, the response time can be monitored. The change of phase occurs over $20 - 40\,\mu$s. To ensure the capture of all the changes, the voltage signal from the photodiode is sampled with almost 5 times the rate of phase change. The signal is sampled with the rate of 250 kS/s for 20 seconds using a NI-DAQ PCI-card. The signal is then saved in a binary format file due to its relativity small size compared to text file and its low memory usage. The files are saved for further processing.

2.3.1 Probe Performance Validation

The probe is tested to ensure that the photo-diode voltage signal is corresponding to the phase change that will take place at the surface. Two test setups, Fig.(2.13), have been built: (a) oscillating cantilever and (b) rising air bubbles.

The oscillating cantilever test outcomes set the expectations for the signal behavior while the probe is alternated between air and water. The probe is attached to the end of a stainless-steel cantilever, as shown in Fig.(2.13-a). The end is free to oscillate in the vertical direction such that at rest the probe tip is slightly above distilled water free surface. From basic physics, first mode natural oscillation frequency is expressed as,

$$\omega = 3.52 \sqrt{\frac{E\, w\, y3}{12\, m\, L^4}} \tag{2.1}$$

where, $\omega = 2\pi f$, E is stainless steel modulus of elasticity, w is the cantilever width, y is the cantilever thickness, m is the oscillating mass, L is the vibrating length.

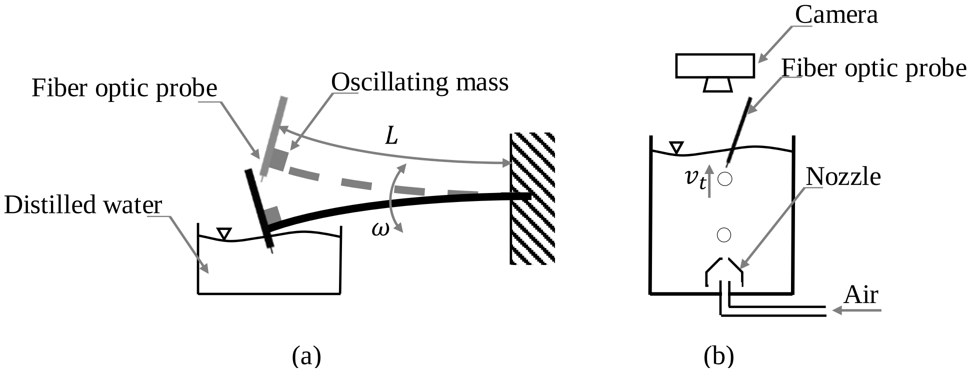

Figure 2.13: fiber optic probe testing: (a) oscillating cantilever, (b) rising air bubble

When the probe immersed in water, most of the light-wave is refracted and the the photodiode voltage is low. While when the probe is in the air, the light-wave is internally reflected and the photodiode voltage is high. Fig.(2.14) shows sample of the signal for the cantilever test. The sudden change from water to air causes sharp jump in the voltage followed by period of oscillation in the voltage. While the sudden change from air to water is followed by flat voltage signal. Fluid Phase Function (FPF),

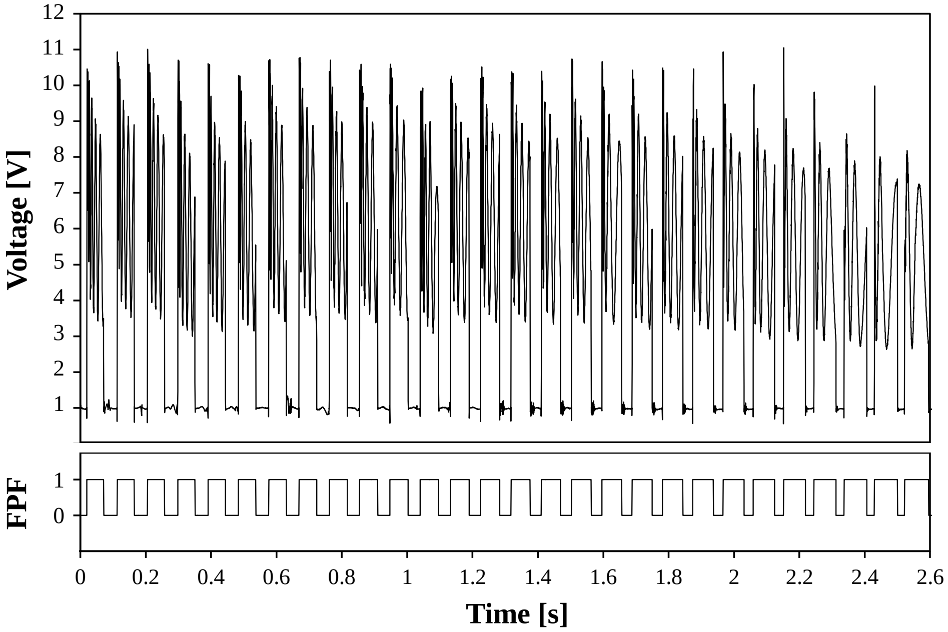

Figure 2.14: Photodiode signal for the oscillating cantilever test

defined in section 5.1, is determined such that values of 1 are assigned to gas/vapor and values of 0 are assigned to liquid.

As the system is underdamped, the oscillation is decaying with time and hence liquid time is decreasing with constant frequency. The calculated frequency from Eq. (2.1) was 11.2 Hz (s^{-1}). While the frequency obtained from the signal was 10.5 Hz

In the rising air bubble test, the trapped air inside the nozzle is released when it reaches certain volume, resulting in a series of bubbles of diameter, D. Air bubbles are assumed to reach terminal velocity when they touch the probe tip. Assuming that bubbles are rising under only drag and buoyancy force, the equilibrium velocity is expressed as,

$$v_t = 2\sqrt{\frac{2}{3}gD} \tag{2.2}$$

The time for the air bubble to pass through the probe can then be calculated knowing the bubble diameter. The air bubble diameter is measured using a camera that is mounted on the top of the water free surface. The most probable diameter is found to be around 3 mm. Water surface with no disturbance is necessary not to distort the image and cause inaccurate diameter measurements. The time required by the bubble to pass the probe is 10.7 ms. The mean time calculated from the measurements is 9.5 ms.

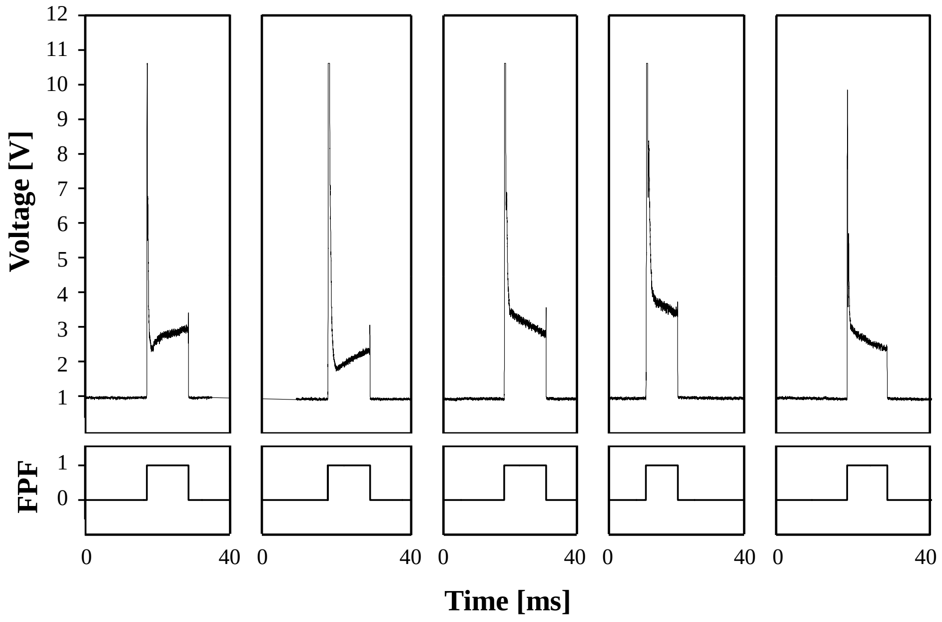

Figure 2.15: Photodiode signal for the rising bubble test

As a bubble comes into contact with the probe, a sudden rise is witnessed in the photodiode signal, as shown in the five instance in Fig. (2.15). The air voltage is distinguishable from the liquid voltage. As the bubble passes by, the probe comes into contact with the liquid again and there is a sudden drop in the voltage as expected.

2.4 High Speed Imaging

Water flow direction is guided on the surface through a channel. The channel is formed using two opposing high purity quartz glass plates, as shown in Fig. (2.16). With a diffused light source placed at one side, high speed images are captured from the other side. High speed images have been taken at a rate of 6,000 fps in order to capture (i) bubble growth and departure in nucleate boiling, and (ii) the cycle of the vapor layer breaking up and its reformation in transition boiling. The camera was set at first parallel to the surface, position (1) in Fig. (2.16), giving real dimensions and fast processing of the images. Yet, the distribution of the bubbles on the surface is not controlled and the bubbles close to the camera will hide bubbles in the middle. Tilting the camera widens the frame and allow more bubbles to be pictured, position (2) in Fig.(2.16). However, tilting the camera at the surface requires correcting the measured lengths and angles measured. A high speed camera has been set with an angle to the surface, as shown in Fig. (2.16), to take pictures. it allows for the observation of bubbles forming on a wider area of the heated surface.

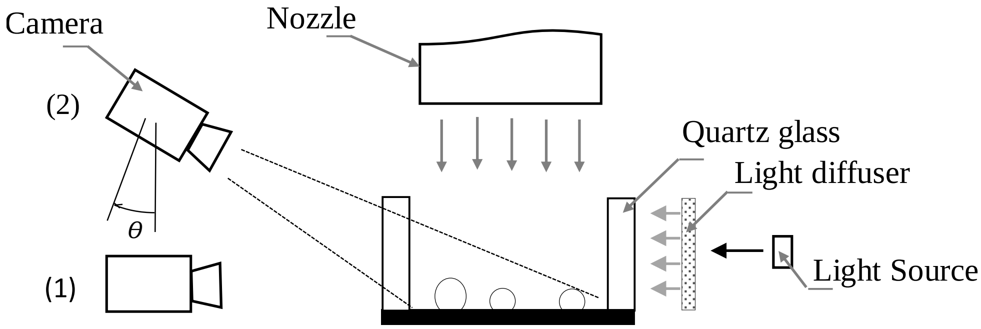

Figure 2.16: High speed camera setup

The captured images are imported to an image processing software, ImageJ, for further processing. The scale is set using a 0.5 mm resolution scale on the surface. A scale ratio is then set in the horizontal direction for all the horizontal measurements while the vertical length measurements and angle measurements are corrected. The relation between the measured and actual lengths and angles is shown in Fig. (2.17) and is expressed as follows,

$$L_a = L_m \cos\theta \tag{2.3}$$

$$\phi_a = \tan^{-1}\frac{\tan\phi_m}{\cos\theta} \tag{2.4}$$

where L_a is the actual length, L_m is the measured length, θ is the camera tilt angle, ϕ_a is the actual angle, and ϕ_m is the measured angle.

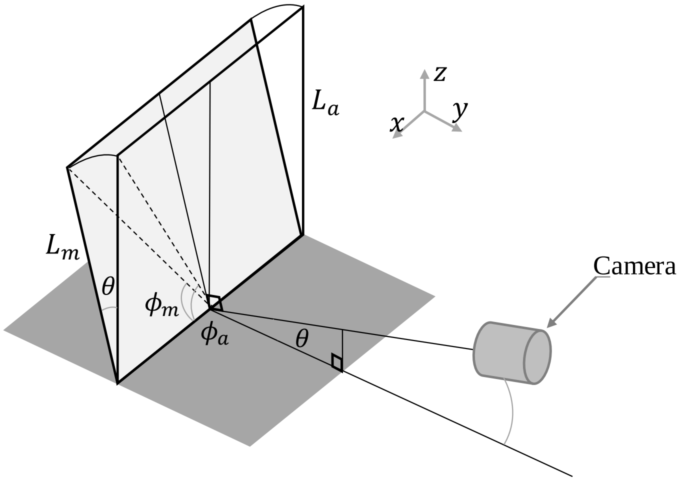

Figure 2.17: Tilted lengths and angles

2.4.1 Measurements Validation

Images from the camera are analyzed to measure the bubble diameter. High confidence in diameter measurements is required in assessing forces acting on the bubble. A 3 mm spherical transparent bead is placed in the the heated water before ONB on the heated surface. The horizontal and vertical diameters are measured using the camera. The horizontal diameter is 2.96 mm and the vertical diameter is 2.56 mm. Knowing that the camera is tilted 30 degrees, the vertical diameter is corrected and is equal to 2.95 mm.

2.5 Inverse Heat Conduction Solver

From the temperature measurements collected, the surface heat flux is estimated using an inverse heat conduction solver, INTEMP. INTEMP is a highly flexible and inexpensive tool to solve inverse heat conduction problem for different systems [52].

The program solves for the spatial temperature using either Crank-Nicolson formula or implicit formula. The fully implicit scheme gives more accurate results in the steady-state case. INTEMP solves for the temperature as,

$$(C_i + k_i h)\, T_{i+1} = (c_i)\, T_i + hPf_i \tag{2.5}$$

Where C is the capacitance matrix, k is the conductance matrix, P is the participation matrix which defines where is the flux is applied and h is the integration step size. INTEMP then solves for the fluxes, f_j, that minimize the general least square error between the input and the estimated temperatures,

$$E = \sum_{j=1}^{N} (UT_j - d_j, A(UT_j - d_j)) + (f_j, Bf_j) \tag{2.6}$$

Where E is the error, d_j is a matrix consists of the input temperatures, U is a matrix identifies the nodal locations of the temperature data, A is symmetric positive matrix represents the weight of the data and B represents the smoothing of the unknown heat flux history. Choosing the optimum values for A and B is a tricky task in INTEMP, as it effects the heat flux in transient data. Luckily, the current work is a steady-state study. The configuration of the mesh and data locations is shown in Fig. (2.18).

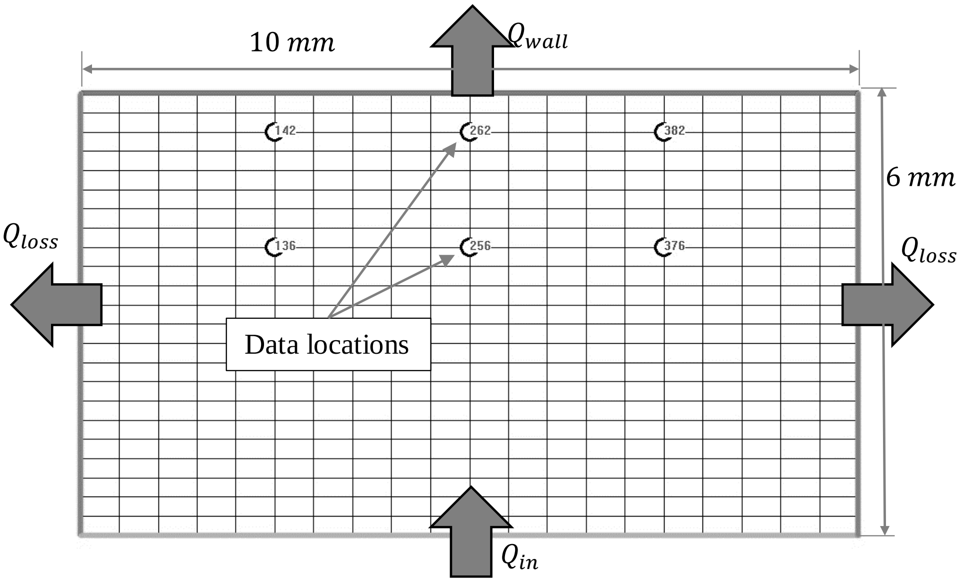

Figure 2.18: One module heater mesh in INTEMP

2.5.1 INTEMP Validation

In order to validate the output of INTEMP, a test case was developed. The spatial temperatures of the one module heater is solved using a 2-D finite element heat transfer program, FEHT. Boundary conditions were chosen such that they represent the actual case of jet impingement. The 6x10 mm copper block is heated from the bottom with a 1 MW/m^2, as shown in Fig. (2.19). Losses to the side is assumed to be 20% of the heat input, 0.2 MW/m^2. The top surface is exposed to a fluid at 100 °C with a heat transfer coefficient of 10 kW/m^{2}K. The temperature of specific nodes, at the same locations as the thermocouples, are exported to INTEMP. INTEMP solved for the heat flux at the surfaces and temperature at the nodes. The estimate of the surface temperature

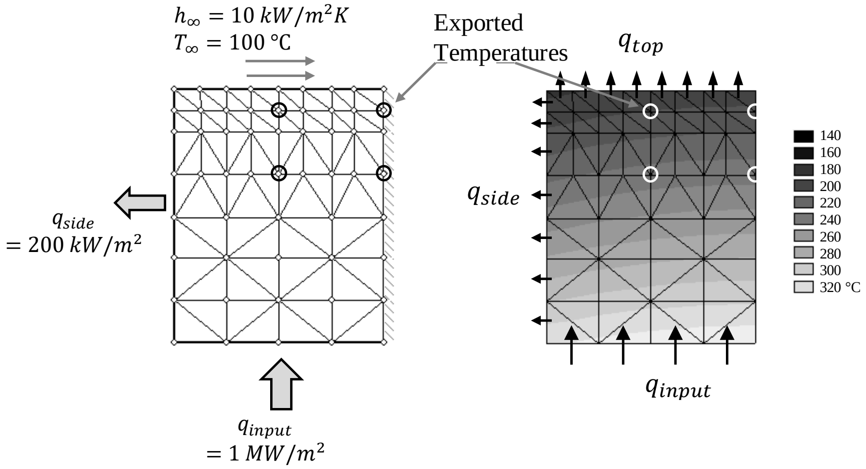

(a) (b)

Figure 2.19: FEHT mesh, left half of the copper block, (a) boundary conditions, (b) temperature contours.

has a maximum error of 1.4 °C, equivalent to 0.85%, as shown in Fig. (2.20). The top heat flux was estimated with an error of 3%, while the side heat flux with 35% and bottom heat flux with a 6%.

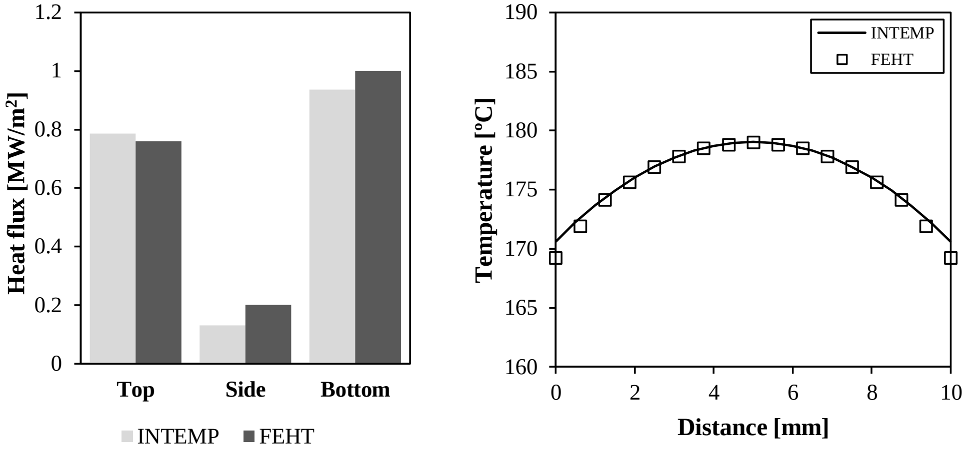

(a) (b)

Figure 2.20: Solution of INTEMP compared to FEHT, (a) top, side, and bottom heat fluxes, (b) surface temperatures

As a second measure of INTEMP accuracy, an energy balance of the copper block is calculated. The heat loss from the copper block is 93% of the input heat flux. The imbalance is 7% of the input heat flux. Because the thermocouples holes positions are chosen to achieve the highest accuracy in top heat flux estimation and surface temperature, the error in the top heat flux is small compared to bottom and side heat flux.

2.6 Thermocouples Calibration

Thermocouples used in the study are calibrated against a calibrated class-A RTD. Thermocouples are placed as close together as possible in a radial pattern with the RTD in the center in a constant temperature oil bath (EXCalibrator [1]), shown in Fig. (2.21). Thermocouples and the RTD sensing tips are all in the same horizontal plane. Enough immersion is ensured to avoid heat losses from the stem. The temperature of the bath is controlled using a PID controller. The oil bath compartment is guarded with a second heater in order to reduce the losses to the surrounding. The insulation temperature is also PID controlled.

Thermocouples temperature and RTD temperature are fed into the LabView Measurement and Automation Explorer (MAX) and calibration curve is plotted. The calibration process is carried out for all the connected and new thermocouples.

---

[1] EXCalibrator is a thermocouple calibration oil bath developed by McMaster Engineering students under supervision of Dr. R. L. Judd

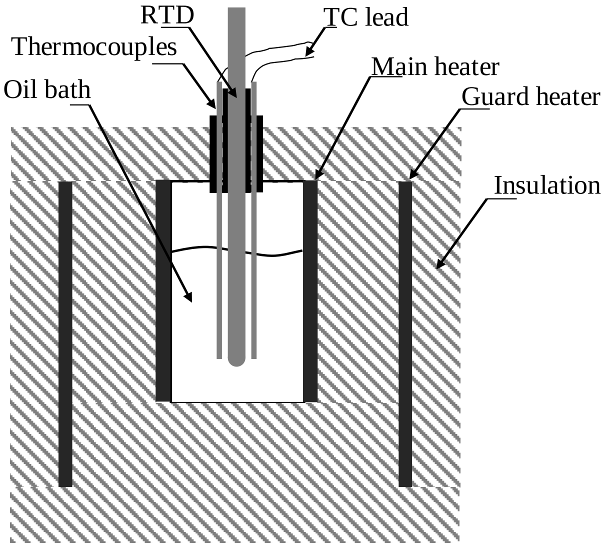

Figure 2.21: Thermally insulated oil bath used for calibration

2.7 Experimental Procedure

The tank is filled with water and the tank heater is turned on till the tank temperature reaches the desired set point. The pump is then switched on with the by-pass valve open to recirculate the water in the tank to ensure that there is no stratification in the tank. The by-pass valve is then partly closed and the nozzle valve is open to get the air out of the loop. Jet temperature and velocity are monitored till they reach steady state before directing the nozzle on the boiling surface.

The boiling surface is cleaned before each experiment with acetone and soft cloth to ensure the surface is free of deposits and marks from the previous experiment.

After the copper block temperature reaches steady state, the DC power supplies are turned on. LabView control program is started with the start of the experiment. The desired temperature set point is set in Lab View and the control algorithm adjust the power supplies current.

The copper block temperature is monitored till is reaches steady state where multiple successive measurement of all the thermocouples, jet velocity, current and voltage is recorded for after processing.

After the completion of the experiment, the power supplies output is set to zero first then switched off. Then, the pump is turned off.

Chapter 3

Bubble Dynamics

The focus of the previous two chapters were the transition boiling under impinging jets. This chapter is mainly discussing bubble dynamics in the nucleate boiling regime under an impinging jet. Omar [18] considered the different cases where bubble would collapse or slide on the surface as a departure scenario. The current experimental results showed small bubble departure diameters in the stagnation region and bigger bubbles away from the center of the jet. Bubbles under the jet are observed to grow and depart after it reaches certain diameter.

3.1 Bubble Growth

The growth process passes through two stages: inertial growth and heat diffusion growth which neither can be ignored. But, the effect of heat transfer is more dominant under the jet. Zuber [33] model, represented by Eq. (1.27), accounts for the condensation from the bubble and hence a decrease in the bubble diameter is expected if the heat input to the bubble is less than the heat to the bulk liquid. The value of the constant,

b which is recommended by Zuber to be $\pi/2$ for a spherical bubble was found not to well represent the data. Value of $b = \pi/7$ was found to fit the data better in the jet stagnation region and $b = 5\pi/6$ for bubbles in the parallel flow region. Heat flux to the bulk liquid is found by an inverse heat conduction solver for each set of experiments.

3.1.1 Bubble Growth Experimental Results

Bubble growth estimation is vital for departure diameter estimation. Calculations of the forces are dependent on the instantaneous bubble diameter and its rate of change. Bubble diameter is measured from incipience to lift-off. As the high speed camera is set to 6000 fps the step in time is the multiples of 1/6 ms. Number of bubbles were measured and tracked at each time step of its time. A representative bubble diameter is chosen based on the average of the measured diameters. The measured diameters are not skewed, so arithmetic mean is representative of the bubble diameter as shown in Fig. (3.1).

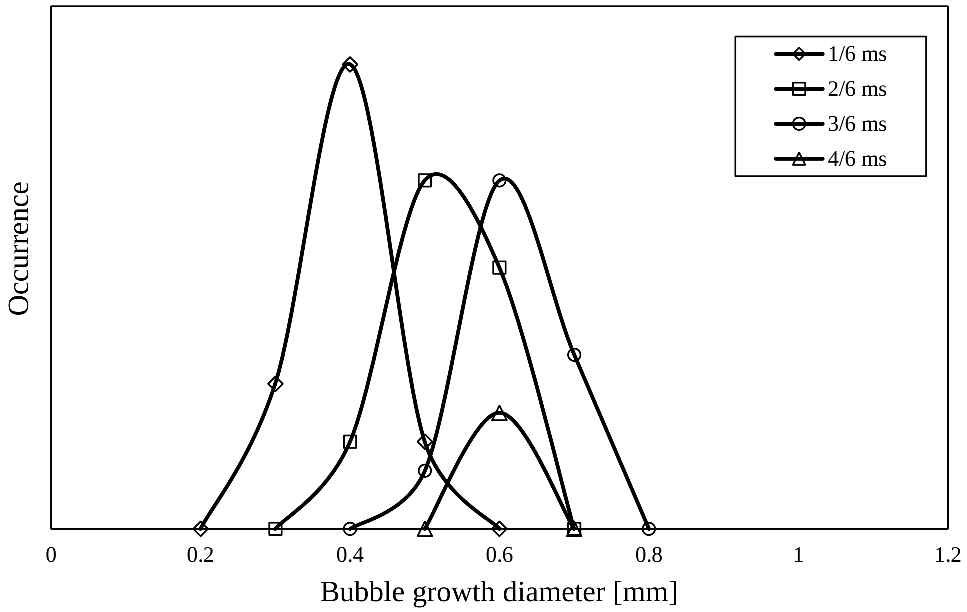

Figure 3.1: Histogram of measured growing bubble diameter at each frame at jet velocity of 0.8 m/s and 20 °C of subcooling

3.1.1.1 Stagnation region

As the Thermal Boundary Layer (TBL) is thinner in case of impingement jet than flow boiling or pool boiling [1], bubble diameter is bigger than the TBL causing condensation at the top of the bubble. Condensation is balanced with evaporation happens in the TBL. Bubble continues to grow (because of the heat diffusion) until the point at which the vertical forces on the bubble, discussed in Section 3.2, act to detach it from the surface ($\Sigma F_y \neq 0$).

Zuber model, Eq. (1.27) estimated the mean bubble diameter in the stagnation region for different conditions of jet velocity ($0.65, 0.8$ and 0.9 m/s) and degrees of subcooling ($13, 20$ and 30 °C). The model showed good agreement with the experimetal measured data except at low jet velocities and high degrees of subcooling where the bubble diameter decrease before lift-off. The model followed the trend of the bubble size with less agreement. Estimated bubble diameters for two cases are shown in Fig. (3.2) and Fig. (3.3)

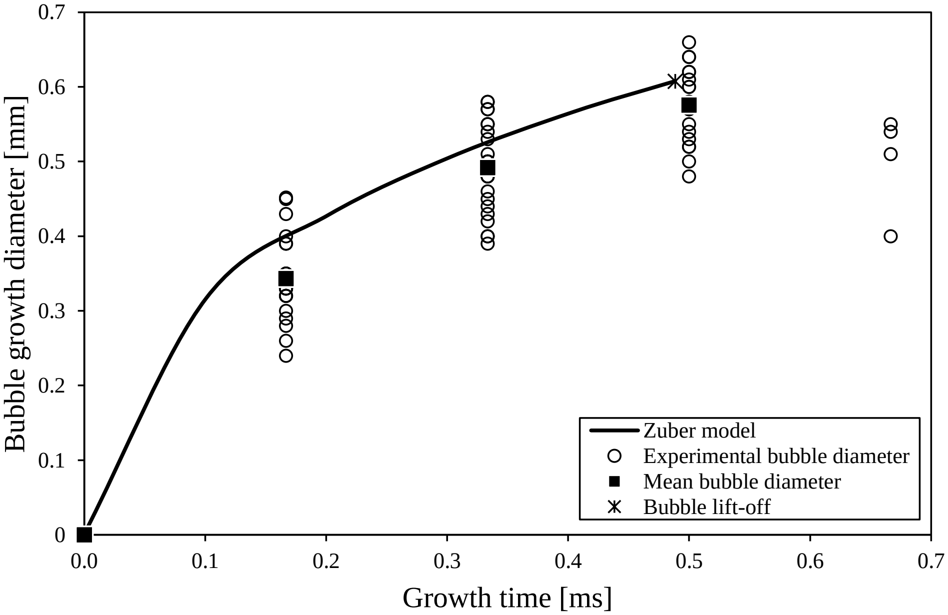

Figure 3.2: Experimental bubble diameter and Zuber model for jet velocity of 0.8 m/s and 20 °C of subcooling

The estimated bubble growth diameter is compared to the experimental measurements and to the mean diameter, as shown in Fig. (3.4). The model has normalized root mean square error (NRMSE) of 21% for the mean diameter and 25% for all the experimental data.

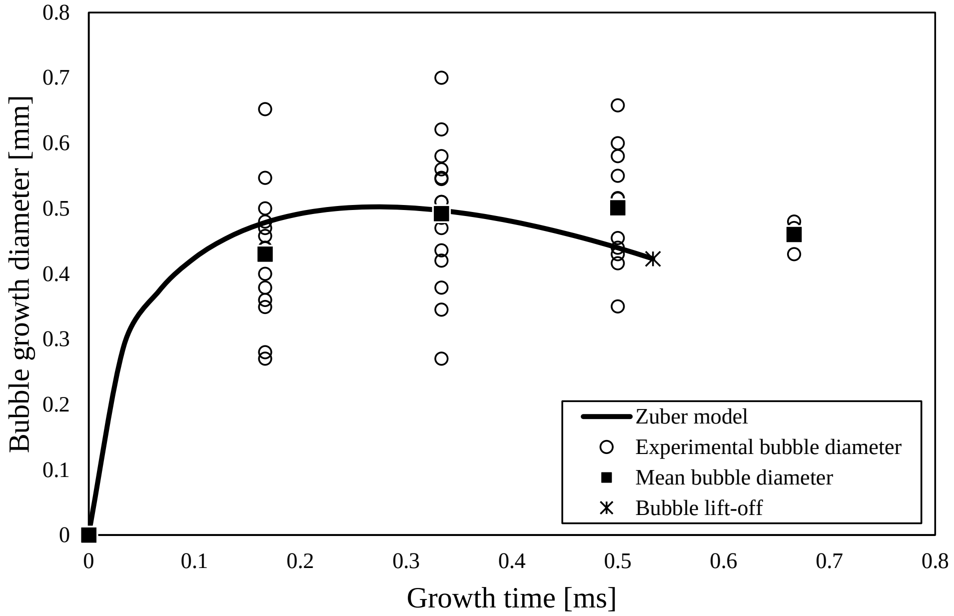

Figure 3.3: Experimental bubble diameter and Zuber model for jet velocity of 0.65 m/s and 13 °C of subcooling

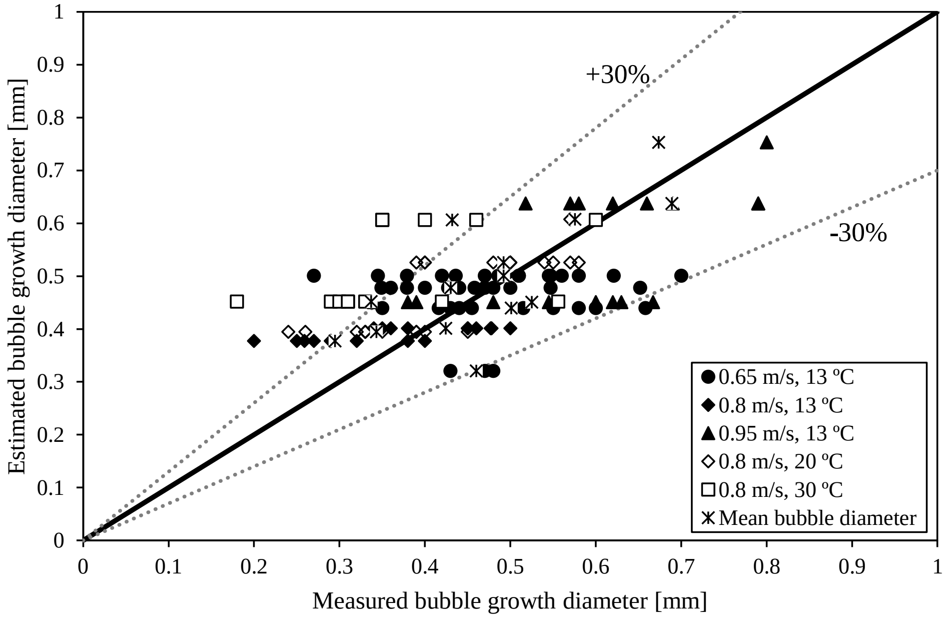

Figure 3.4: Experimental bubble diameter vs estimated bubble diameter in the stagnation region

3.1.1.2 Parallel flow region

The boiling surface in the parallel flow was pictured under water jet velocity of 0.85 m/s and 7 °C of subcooling. Diameter of the bubble was measured every two frames with an uncertainty of ±0.14 mm. The bubble diameter was observed to increase with the distance from the jet. For example, the most probable bubble diameters for nucleation sites $x/w = 16$ is 0.8 mm compared to 2.1 mm for $x/w = 22$. The previous observation coincide with the the current understanding of the jet dynamics. The jet cause a thin boundary layer and hence smaller bubbles [1].

Mikic model, Eq. (1.29), was initially used to estimate the bubble growth diameter for bubbles away from the jet. Their proposed relation is considered as the average between the linear growth in the inertia controlled growth and the power growth in the heat diffusion controlled growth. The model fits the data reasonably, but it does not predict the reduction in diameter due to the condensation close to the lift-off. Fig. (3.5) shows Mikic model against experimental data for different waiting times. The waiting time data were collected for the average time taken between first bubble departure and successive bubble incipience from the same nucleation site. On the other hand, Zuber model, shown in Fig. (3.5), shows better agreement with the experimental data and counts for the condensation at the top of the bubble. The different values for, q_b are obtained from solving the inverse heat conduction problem and estimating the heat flux at different values of x/w. Comparison between the experimental data and estimated values of bubble diameter for different values of x/w is shown in Fig. (3.6). The model tends to overestimate the growth rate for $x/w = 16$ and 22. The model has a normalized root mean square error (NRMSE) of 31% for the parallel flow region.

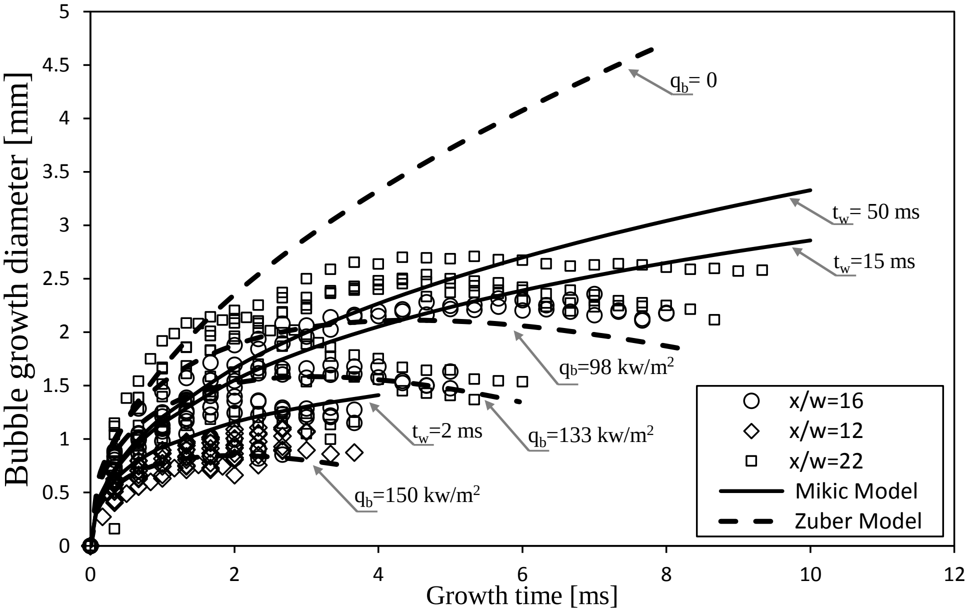

Figure 3.5: Bubble growth diameter for 0.85 m/s jet velocity and 7 °C of subcooling compared to Zuber and Mikic model

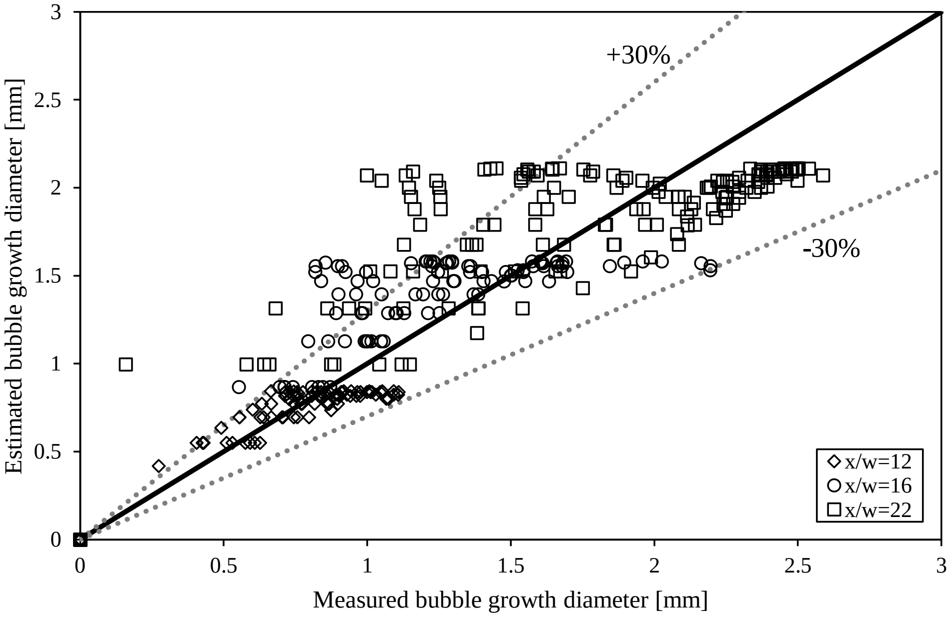

Figure 3.6: Estimated values of Zuber model vs experimental data for parallel flow region

3.2 Forces on a Growing Bubble under an Impinging Jet

Bubble growth under an impinging jet has different characteristics than the extensively studied pool boiling and flow boiling as the jet hydrodynamics adds extra forces on the bubble. By considering the forces acting on a bubble in flow boiling [35, 39], the proposed forces acting on a growing bubble under the jet are shown in Fig. (3.7). The force balance in the y-direction can be expressed as,

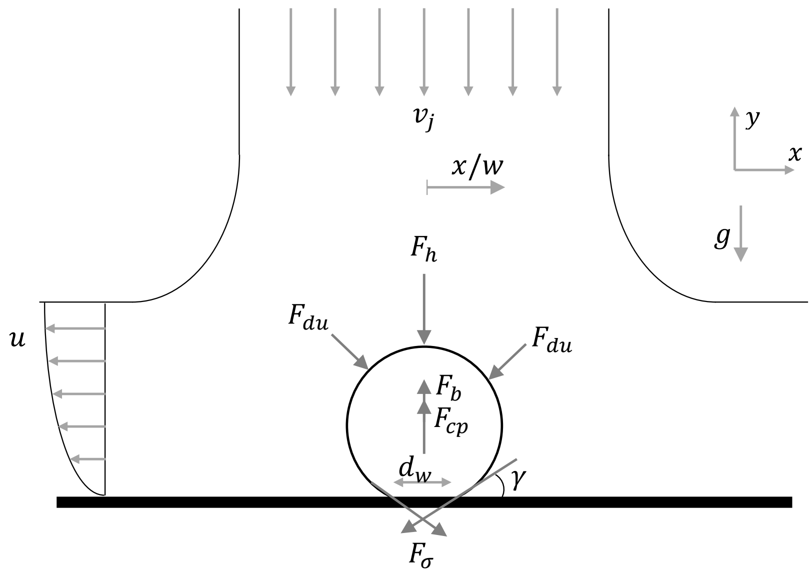

Figure 3.7: Forces acting on a bubble in the stagnation region

$$\sum F_y = F_\sigma + F_{du} + F_{cp} + F_b + F_h \tag{3.1}$$

where, F_σ is y-direction surface tension, F_{du} is asymmetric growth force, F_{cp} is contact pressure force, F_b is buoyancy force, and F_h is the hydrodynamic pressure force caused by the jet. In the stagnation region, the x-direction forces are balanced and no information may be inferred from it. Following is a description of each force component.

3.2.1 Surface Tension Force

The surface tension force is written as,

$$F_\sigma = \int_0^{2\pi} d_w \sigma \; sin \; \gamma \; d\phi \tag{3.2}$$

where ϕ is a polar angle around the bubble, d_w is the contact diameter, σ is the surface tension, and γ is the contact angle which is assumed to be constant as the bubble is symmetric under the jet. By integrating tension forces, Eq. (3.2) can be written as,

$$F_\sigma = 2\pi d_w \sigma \; sin \; \gamma \tag{3.3}$$

Contact angle, γ, is condition dependent and estimation models are scarce in the literature which leaves a room for uncertainty in the model [53]. The contact angle is measured in the current set of experiments. The contact diameter, d_w, value is related to the bubble diameter as, $d_w = 2r/15$ based on recommendation of Yun et al. [40].

3.2.2 Asymmetrical Bubble Growth Force

Klausner et al. [39] considered the ideal case of bubble growth where an attached hemispherical bubble is expanding in a stagnant liquid. The pressure distribution over an expanding bubble in Eq. (1.24) is used to find the forces due to bubble growth. The forces on a hemispherical bubble due to the growth is expressed as,

$$F_{du,s} = \pi \rho_l r^2 \left[r \, \ddot{r} + 1.5 \, \dot{r}^2 \right] \tag{3.4}$$

The bubble is not actually expanding in a stagnant fluid; it is expanding in an opposing flowing fluid. By considering the inviscid velocity potential, the extra force component due to the growth in a non-stagnant fluid is expressed as [39],

$$F_{du,m} = 2\pi \rho_l V_j r \dot{r} \tag{3.5}$$

3.2.3 Pressure Forces

The remaining forces (F_b, F_{cp}, F_h) which are due to pressure distribution at the bubble in the y-direction is simplified and is written as,

$$F_b = 4/3\, \pi r^3 (\rho_l - \rho_v) g \tag{3.6}$$

$$F_{cp} = \frac{\pi d_w^2}{4} \frac{2\sigma}{r_r} \tag{3.7}$$

$$F_h = P_j \frac{\pi}{4} d_w^2 \tag{3.8}$$

where r_r is the radius of curvature of the bubble at the reference point on the surface $y = 0$, and it is usually an order of magnitude greater than the mean bubble radius. The contact pressure is the force due to the pressure difference inside and outside the bubble over the contact area where $r_r = 10\, r$ [39].

The hydrodynamic jet force, F_h, is also resulting from the dynamic pressure change at the bubble. Zumbrunnen et al. [54] developed a formula for the pressure distribution in the stagnation region under a planar jet based on experimental measurements as shown in Eq. (3.9).

$$\frac{P_j}{\frac{1}{2}\rho_l V_j^2} = 2\left(\frac{x/w}{1.75}\right)^3 - 3\left(\frac{x/w}{1.75}\right)^2 + 1 \tag{3.9}$$

3.3 Bubble Departure at Stagnation

As bubble grows, the magnitude of the forces acting on it changes. Once the diameter at which the condition $\Sigma F > 0$ is reached, bubble leaves nucleation site and lifts off. Before this condition is met, forces anchor bubble to the surface. Evaluation of the forces on the bubble is greatly related to bubble growth.

At the point of lift-off the buoyancy and contact pressure forces balance with the asymmetric growth, surface tension and jet caused hydrodynamic forces as shown in Fig. (3.8). Contact pressure force is almost negligible compared to other forces. It is in order of $F_{cp} \sim 7 \times 10^{-8}\,\mathrm{N}$ compared to $F_b \sim 1 \times 10^{-4}\,\mathrm{N}$ for buoyancy force. The asymmetric bubble growth in a stagnant fluid component is high in the beginning then it slightly decreases as the growth reaches asymptote. It is in order of $F_{du,s} \sim 4 \times 10^{-5}\,\mathrm{N}$ compared to $F_{du,m} \sim 8 \times 10^{-5}\,\mathrm{N}$ for the asymmetric bubble growth in a moving fluid component. Surface tension is small as expected and might be ignored with a marginal error; it is in order of $F_\sigma \sim 8 \times 10^{-6}\,\mathrm{N}$. Finally, the hydrodynamic force caused by the jet is in order of $F_h \sim 2 \times 10^{-5}\,\mathrm{N}$. As all the anchoring forces are balanced with, mainly, the buoyancy force, the balance occurs at large bubble diameters. The experimental data is compared to the estimation from the model. The estimated departure bubble diameter is usually overestimated as shown in Fig. (3.9). Bubbles were observed to depart at lower diameters than the estimated values. The magnitudes of forces calculated from the model are bigger than ranges reported in the literature [35, 39].

The previous two facts raise a question, do bubbles really depart in the stagnation region? A quick answer will be no as the jet influence is so high and it will collapse. A more reasonable answer will be it depends. Experimental observations confer that

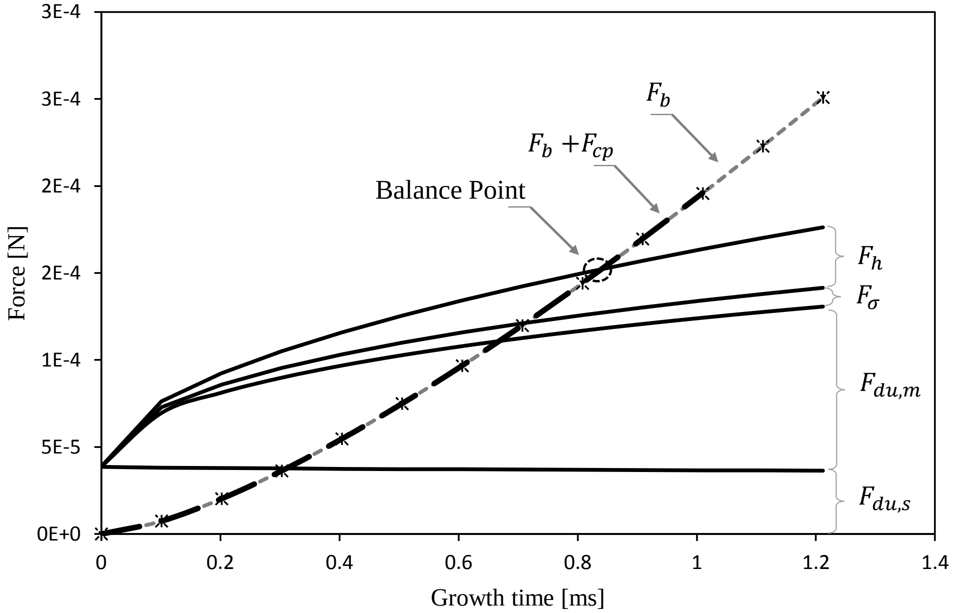

Figure 3.8: Instantaneous forces acting on a growing bubble under an impinging jet

bubble shrinks again after it reaches a maximum bubble diameter. As this happens, asymmetric growth forces dramatically increase and lift-off is attained at smaller bubble diameters. The model estimated the departure diameter with a NRMSE of 21%.

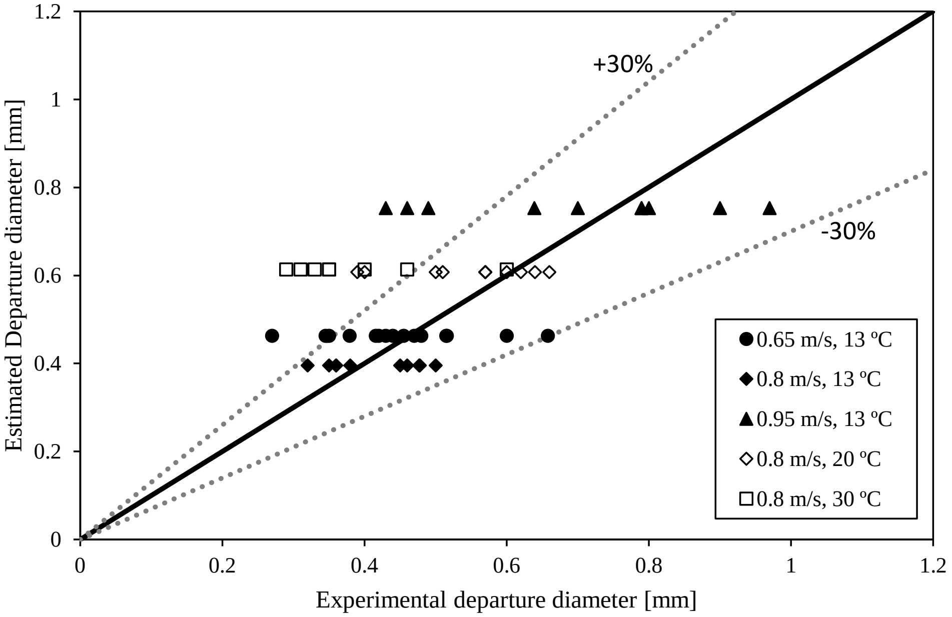

Figure 3.9: Instantaneous forces acting on a growing bubble under an impinging jet

Chapter 4

Transition Boiling Heat Flux

This chapter presents a description of transition boiling characteristics under an impinging jet. The results in this chapter are obtained using the high temperature single module heater described in Section 2.2.2. Embedded thermocouples temperature measurements are used to estimate the heat flux and temperature at the surface.

Fig. (4.1) shows the boiling curve for a steady-state experiment carried out for 0.6 m/s jet velocity and 15 °C degree of subcooling. The surface degree of superheat is controlled and increased in steps till $\Delta T_{sup} = 460\,°\mathrm{C}$. The wide range of surface superheat allowed for different modes of heat transfer to be observed on the surface.

Before the ONB, 10 °C of superheat, heat is extracted from the surface by forced convection. It is followed by nucleate boiling where scattered bubbles appear on the surface until the CHF (point a) is reached at about 63 °C of superheat. The CHF under the jet is much higher than CHF in the case of pool and flow boiling.

At CHF, bubbles ability to coalesce increases and bubbles start to form vapor pockets. Vapor pockets promote the transition boiling conditions which are observed over a wide range of degrees of superheat up to about 455 °C. In the transition boiling,

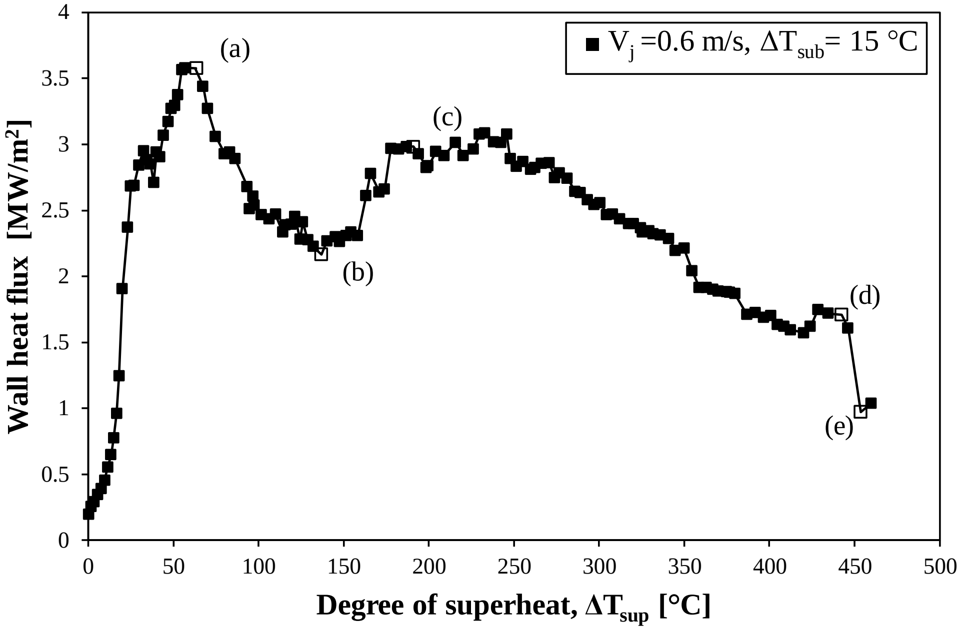

Figure 4.1: Impinging jet boiling curve at the stagnation region at $V_j = 0.6\,\mathrm{m/s}$ and $\Delta T_{sub} = 15\,°\mathrm{C}$.

the heat flux decreased then increased again passing through a point of a local minimum heat flux called the first minimum [42].

From the boiling curve in Fig. (4.1), the transition boiling can be divided into four regions: (i) decrease in heat flux, from CHF to the first minimum (a-b); (ii) increase in heat flux, from the first minimum until a constant heat flux is reached (b-c); (iii) a region of constant heat flux, known as the shoulder boiling followed by a decrease in the heat flux (c-d); and (iv) rapid decrease in heat flux, until the incipience of film boiling is reached at about 455 °C of superheat (d-e). Film boiling starts beyond the Leidenfrost point. In the film boiling, the heat flux is expected to increase with the surface degree of superheat.

In comparison with Fig. (1.9), transition boiling in Fig. (4.1) has less fluctuations in the surface heat flux. There are two reasons why the curve does not suffer from the same amount of noise as Fig. (1.9). During the experiment multiple consecutive values of the thermocouples reading is stored and averaged to get one value for each thermocouple at each set point. The variation in the temperature is within ±5 °C.

The averaged temperatures is then fed into INTEMP to estimate the heat flux and the surface temperature. INTEMP smooths output data with a third order filter to ensure there is no outlayer points in the estimation, as the inverse problem is sensitive to spurious data [52].

The smoothing parameters can be optimized to minimize the mean square error and the norm of the heat flux. If the mean square error and the norm of the heat flux are plotted against each other, the point in the left bottom of the curve is the optimum value. In this study value of 1000 is found to be the optimum value.

4.1 Surface Re-wetting Mechanisms

In transition boiling, the surface goes through a repetitive cycle of dryness and wetness due to formation and break-up of vapor pockets. The high speed camera, in Section 4.1, captured 6,000 pictures per second of the surface in order to capture the cycle of the vapor break-up and reformation.

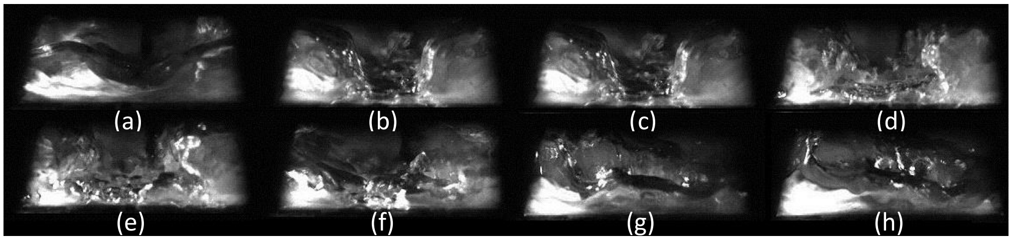

Figure 4.2: Snapshots of the observed vapor layer breakup cycle at moderate degrees of superheat

Fig. (4.2) represents one full cycle of vapor break-up and formation. The alphabetically labeled frames are 8 selected pictures of a total of 426 frame. Each two

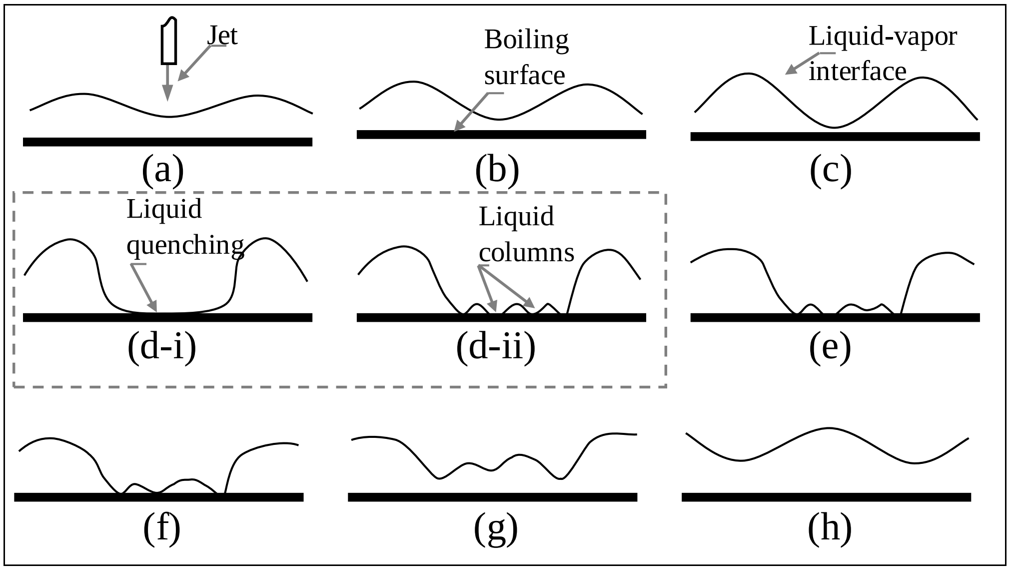

Figure 4.3: Schematic of the observed vapor layer breakup cycle

frames of the 8 frames are separated by ∼ 8.8 ms (53 frames). The observed cycle of vapor break-up and formation is schematically represented in Fig. (4.3). The interface disturbance caused by the jet grows till the liquid approaches the surface (Fig. (4.2 a-c) and Fig. (4.3 a-c)). At moderately high degrees of superheat, it is often observed that the liquid touches the surface and spreads on it (Fig. (4.2 d) and Fig. (4.3 d-i)). While at high degrees of superheat, the liquid mostly reaches the surface in the form of small liquid columns penetrating the thin vapor layer, under Rayleigh-Taylor instability, and capturing vapor pockets between the penetrating columns (Fig. (4.3 d-ii) and Fig. (4.4 c)). Finally, the vapor pockets grow and start to coalesce (Fig. (4.2 e-f) and Fig. (4.3 e-f)) till the surface is completely isolated from the liquid (Fig. (4.2 g-h) and and Fig. (4.3 g-h)).

For the experiment shown in Fig. (4.1), sample of the high speed images captured is shown in Fig. (4.4). The surface goes through cycles of dryness and wetness as the vapor layer goes through continuous cycles of break-up and formation in the transition boiling regime until the vapor thickness is significantly reduced and a stable vapor film is formed at the incipience of film boiling. At CHF, bubbles merge and form large volume of vapor pockets (Fig. (4.4 a)). Vapor pockets isolate large areas of the heater from being reached by the liquid. At very high degrees of superheat, a stable vapor film (Fig. (4.4 d)) is formed and any introduced instability is decayed.

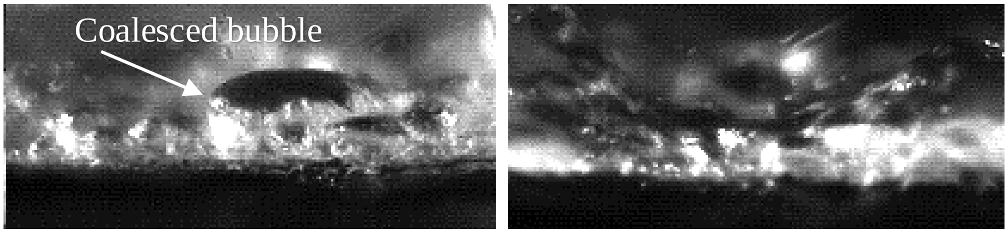

(a) $\Delta T_{sup} = 63\ °C$
Vapor layer formation

(b) $\Delta T_{sup} = 135\ °C$
Vapor layer break up

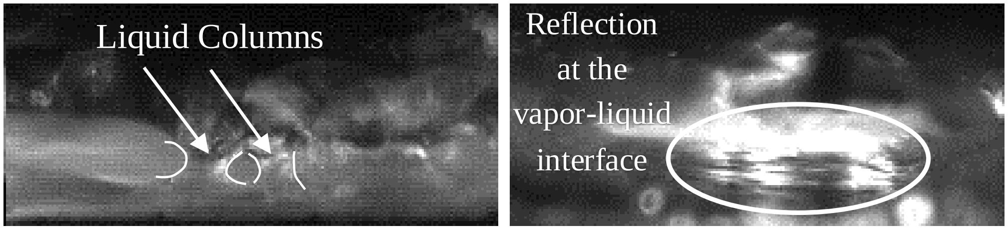

(c) $\Delta T_{sup} = 190\ °C$
Liquid intrusions

(d) $\Delta T_{sup} = 455\ °C$
Stable vapor film

Figure 4.4: Images of bubble dynamics on the boiling surface at points a,b,c and d in Fig. (4.1)

The use of the high speed camera is combined with miniaturized fiber optic probe to distinguish between the liquid and vapor phases at the proximity of the surface. With the current etched probe, distinguishability of the phase is possible down to distance of 10 μm from the surface. Detailed description of the fiber optic is in Section 2.3, while the signal analysis is in Chapter 5.

4.2 Rayleigh-Taylor Instability

Based on the high speed images obtained in this study and the previous work reported in the literature [19, 42, 47, 48, 55], it seems that Rayleigh-Taylor instability plays a role in promoting or demoting the wetting of the dry surface under the jet in the transition boiling regime. When two fluids of different densities configured such that a heavier fluid (water in this case) is resting on a lighter fluid (vapor), as shown in Fig. (4.5), Rayleigh-Taylor instability is of a concern. As the interface is disturbed due to the acceleration of one fluid into the other, normal to the interface, the disturbance might grow if the acceleration is from the low density to the high density fluid [33]. The interface would remain stable and would dissipate any disturbances elsewise.

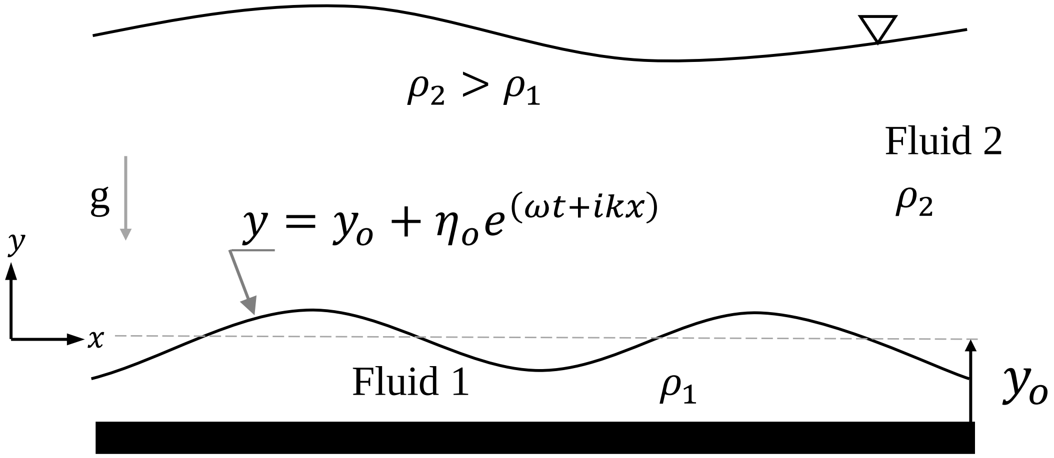

Figure 4.5: Rayleigh-Taylor instability: Two fluids of different densities

Rayleigh-Taylor (RT) instability has been studied extensively for many decades. Different analysis techniques has been implemented to find valid expressions for the dispersion relation and the critical wave length. The critical wave length, λ_c, is defined as the wavelength at which the perturbation starts to grow, while the most dangerous wavelength, λ_d, corresponds to the maximum instability growth rate. Taylor [56] and Lewis [57] studied the instability of a falling liquid layer of a finite height bounded with air at the top and the bottom. Interfaces are accelerated in a normal direction to their planes. They derived an expression for the linear part of the instability. based on the potential flow theory, the critical wavelength and the most dangerous wavelength are expressed as [58],

$$\lambda_c = 2\pi\sqrt{\frac{\sigma}{a(\rho_l - \rho_g)}} \tag{4.1}$$

$$\lambda_d = \sqrt{3}\lambda_c \tag{4.2}$$

where a is the acceleration of the vapor into the water, σ is the water surface tension, ρ_l and ρ_v are the densities of the liquid and the vapor, respectively.

4.2.1 Effect of Heat Transfer on RT Instability

Due to the increased interest in the RT instability in heat transfer applications, the effect of heat and mass transfer on RT instability was studied by Hsieh [59]. The dispersion relation based on the inviscid flow analysis is given by,

$$\begin{aligned}\Big[\rho_v \coth(kh_v) + \rho_l \coth(kh_l)\Big]\omega^2 + \Big[(\rho_v - \rho_l)ak + \sigma k^3\Big] \\ + \left[\frac{K\Delta T_{sup}}{h_v h_{fg}}\left(\frac{1}{h_l} + \frac{1}{h_v}\right)(\coth(kh_v) + \coth(kh_l))\right]\omega = 0\end{aligned} \tag{4.3}$$

where K is the vapor thermal conductivity, k is the wave number, h_l and h_v are the water and vapor height, respectively, ω is the growth rate, and h_{fg} is the latent heat of vaporization.

For the case of zero temperature gradient (no heat transfer), Hsieh concluded that the perturbation will grow only under the acceleration effect. However, for a positive temperature gradient (heat is flowing from vapor to liquid), any intrusion of the liquid into the vapor results in liquid evaporation and the instability is damped. For film boiling, the temperature gradient is very strong such that any introduced perturbation is damped and the vapor film is stable.

Recently, Awasthi and Agrwal [60] developed a viscous potential model to include the effect of heat and mass transfer on RT instability. Awasthi [61] modified the model by considering the viscous pressure in the normal stress balance and concluded that heat and mass transfer have a stabilizing effect on the instability. He derived a relation for the growth rate, Eq. (4.4), and the critical wave number, Eq. (4.5), which can be directly related to the critical wave length as $\lambda_c = 2\pi/k_c$,

$$\begin{aligned}\Big[\rho_v \coth(kh_v) + \rho_l \coth(kh_l)\Big]\omega^2 \\ +\Bigg[\frac{K\Delta T_{sup}}{h_v h_{fg}}\left(\frac{1}{h_l}+\frac{1}{h_v}\right)(\coth(kh_v)+\coth(kh_l)) \\ +4k^2(\mu_v \coth(kh_v) + \mu_l \coth(kh_l))\Bigg]\omega \\ +\Bigg[(\rho_v-\rho_l)ak + \sigma k^3 + 4k^2\frac{K\Delta T_{sup}}{h_v h_{fg}} \\ \times\left(\frac{\mu_v}{\rho_v}\coth(kh_v) + \frac{\mu_l}{\rho_l}\coth(kh_l)\right)\Bigg] = 0 \end{aligned} \tag{4.4}$$

$$\begin{aligned} k^2 + \frac{4k}{\sigma}\left(\frac{\mu_v}{\rho_v}\coth(kh_v) + \frac{\mu_l}{\rho_l}\coth(kh_l)\right) \\ \times\frac{K\Delta T_{sup}}{h_v h_{fg}}\left(\frac{1}{h_l}+\frac{1}{h_v}\right) - \frac{(\rho_l-\rho_v)a}{\sigma} = 0 \end{aligned} \tag{4.5}$$

where μ_l and μ_v are the dynamic viscosity of the water and vapor, respectively.

4.2.2 Vapor Acceleration into Liquid

In the case of boiling under an impinging jet, the jet is disturbing the liquid free surface and the liquid-vapor interface. The traditional acceleration, $a = g$ is not physically representing the actual acceleration. A new expression for the interface acceleration accounts for both gravitational acceleration and jet dynamics is needed.

The jet dynamic pressure at the stagnation region causes pressure difference across the liquid layer. The difference in pressure causes extra acceleration of both the fluid into each other that is not accounted for in the classical RT instability.

Baker et al. [62] studied the effect of pressure difference on RT instability of liquid layer with two disturbed interfaces. He found that the acceleration resulting from the pressure difference across the two interfaces of the liquid layer is,

$$a = \frac{\Delta P}{\rho h_l} \tag{4.6}$$

where a is the acceleration and h_l is the liquid layer height.

Zumbrunnen et al. [54] developed a relation for the stagnation pressure gradient caused by a planar jet based on experimental measurements and found it to be,

$$\frac{P}{\frac{1}{2}\rho_l V_j^2} = 2\left(\frac{x/w}{1.75}\right)^3 - 3\left(\frac{x/w}{1.75}\right)^2 + 1 \tag{4.7}$$

From Eq. (4.6) and Eq. (4.7), the proposed total acceleration expression on the interface at the stagnation region $(x/w = 0)$ is,

$$a = \frac{V_j^2}{2h_l} + g \tag{4.8}$$

where V_j is the jet velocity and g is the gravitational acceleration.

4.2.3 Relation between The Critical and The Most Dangerous Wavelengths

Eq. 4.2 relates the most dangerous wavelength to the critical wavelength based on the potential flow theory. Kim et al. [63] compared the instability growth from four models, namely: inviscid potential flow, viscous potential flow, fully viscous flow analysis and lubrication theory. They found that for thin vapor layers, the ratio between the most dangerous wavelength, λ_d, and the critical wavelength, λ_c, is not constant to ($\sqrt{3}$) as in Eq. (4.2). However, it depends on the vapor height. Their findings can be expressed as,

$$\lambda_d = \begin{cases} \sqrt{3}\,\lambda_c & h_v < 10\sqrt{\sigma\Delta\rho g} \\ \sqrt{2}\,\lambda_c & h_v \geq 10\sqrt{\sigma\Delta\rho g} \end{cases} \tag{4.9}$$

After obtaining the acceleration from Eq. (4.8). The critical wavelength is calculated from Eq. (4.5). The most dangerous wave number/length is related to the critical wave number/length by Eq. (4.9). The most dangerous wave number is then used to calculate the most dangerous growth rate from Eq. (4.4).

4.3 Transition Boiling Heat Flux Model

CHF in pool boiling is characterized by a vapor layer that isolates the surface from the liquid resulting in a decrease in the heat flux. Similar to pool boiling, vapor pockets are formed in the stagnation region under impinging jets. The formed vapor pockets result in a decrease in the heat flux. However, the jet causes disturbance to the liquid-vapor interface. The disturbance grows under the effect of Rayleigh-Taylor instability resulting in an increase in the heat flux.

Unlike the classical Rayleigh-Taylor instability where the lighter fluid is accelerated only under gravitational acceleration, the jet creates an additional acceleration term adding a source of instability to the system (See Section 4.2.2). The additional acceleration term is due to the dynamic pressure of the jet. The total acceleration term used in the current model is given by Eq. (4.8).

Based on observations discussed in Section 4.1, a wall heat flux partitioning model is proposed. The model assumes that the heat flux constitutes of two components: liquid quenching transient conduction and liquid intrusions transient conduction. At moderately high degrees of superheat, $\sim 80\,^{\circ}\mathrm{C}$, heat is extracted from the surface through transient conduction as liquid rushes and quenches the surface for the time permitted by the vapor break up cycle.

At high degrees of superheat, $\sim 200\,^{\circ}\mathrm{C}$, the ability of the liquid to wet the surface decreases as the vapor builds up promoting RT instability. The liquid reaches the surface in the form of liquid columns intruding into the vapor layer. Heat is mainly transferred by transient conduction through the intruding liquid columns. Transient conduction dominates till the liquid columns reach the saturation temperature and a microlayer of vapor is formed which evicts the liquid back into the bulk liquid. It is worth noting that there is no fine line separating the two components/mechanisms as the vapor break-up and formation cycle, described in Section 4.1, occurs at all degrees of superheat up to the Leidenfrost point. The proposed model of the wall heat flux is expressed as,

$$q_w = A\, q_i + B\, q_q \tag{4.10}$$

where q_i is the liquid intrusion transient conduction component, q_q is the liquid quenching transient conduction component. A and B are expressed as,

$$\begin{aligned} A &= \left(\frac{\Delta T_{sup}}{\Delta T_{min}}\right)^n \\ B &= 1 - A \end{aligned} \tag{4.11}$$

A and B account for the increase in degree of superheat; such that at moderate degrees of superheat, heat transfer from liquid in direct contact with the surface is more prevailing. However, at high degrees of superheat, the heat flux is mainly due to liquid intrusions. This assumption is justified from the high speed imaging on the vapor layer break-up, yet the change with the degree of superheat can not be inferred directly from the images. Exponent value of $n = 0.4$ is found to best represent the change in the factors A and B for experiments in literature [48]. The same value is found to predict the heat flux reasonably for other experiments in [19, 42]. ΔT_{min} is the degree of superheat corresponding to the Leidenfrost point; it is determined experimentally.

The liquid quenching component, q_q, is determined assuming transient conduction in a semi-infinite liquid volume,

$$q_q = K_l \frac{T_w - T_l}{\sqrt{\pi \alpha t}} \tag{4.12}$$

where k_l is the liquid thermal conductivity, α is the liquid thermal diffusivity, and t is the contact time between the liquid and the surface; it is determined experimentally from the surface wetting frequency obtained by Bogdanic et al. [48], $t = 1/f$

The liquid intrusion component, q_i, is determined by considering the lumped capacitance transient conduction,

$$q_i = \frac{\rho_l A_l h_v \, C_p \, \Delta T_{sub}}{A_{eff}} \, \frac{A_l}{A_c} \, \omega \tag{4.13}$$

where A_l is the liquid intrusion area as shown by the circles in Fig. (4.6), $A_{eff} = cA_h$, c is the portion of the heater area, A_h, where the re-wetting occurs. Value of $c = 0.4$ is representing for the stagnation and acceleration region where $x/w < 2$ [1], h_v is liquid columns intrusion height and it is equal to the vapor structure height data collected by Bogdanic et al. [48], ω is the growth rate estimated from Rayleigh-Taylor instability dispersion relation, Eq. (4.4), and A_l/A_c is the ratio between the liquid area and the total (liquid and vapor) area represented in Fig. (4.6).

From RT analysis in Section 4.2, the liquid columns are assumed to intrude the vapor layer and touch the surface at locations separated by the RT most dangerous wavelength, λ_d, and are of diameter of $\lambda_d/2$. The area bounded in the hatched rhombus in Fig. (4.6) represents a repeated cell area. The area ratio is the ratio between the liquid area (grayed areas) and the hatched area. The area ratio is expressed as,

$$\frac{A_l}{A_c} = \frac{\pi}{8\sqrt{3}} \tag{4.14}$$

The periodic surface wetting frequency data, as shown in Fig. (4.7), are adapted from the optical probe experimental measurements carried out for the current experiments as discussed in Chapter 5. The vapor structure height measurements were not measured in the current study. Rather, measurements carried out by Bogdanic et al. [48] are assumed to be valid to all the current experiments.

The proposed model in Eq. (4.10) has been used to calculate the wall heat flux for the current experimental data and different experimental data found in the literature,

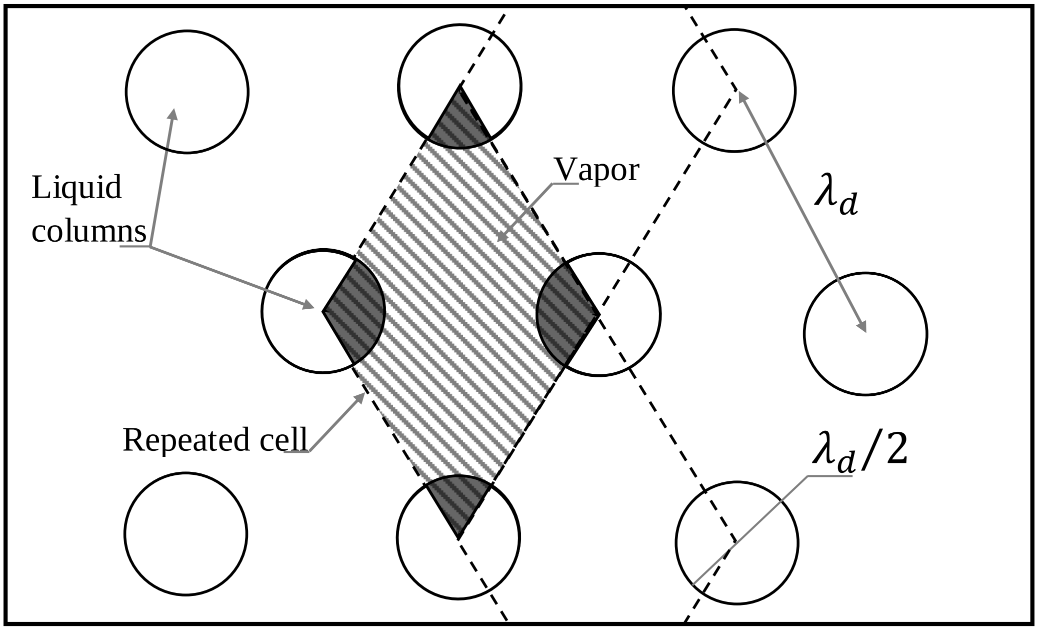

Figure 4.6: Liquid columns contact area on the surface and the repeated cell area

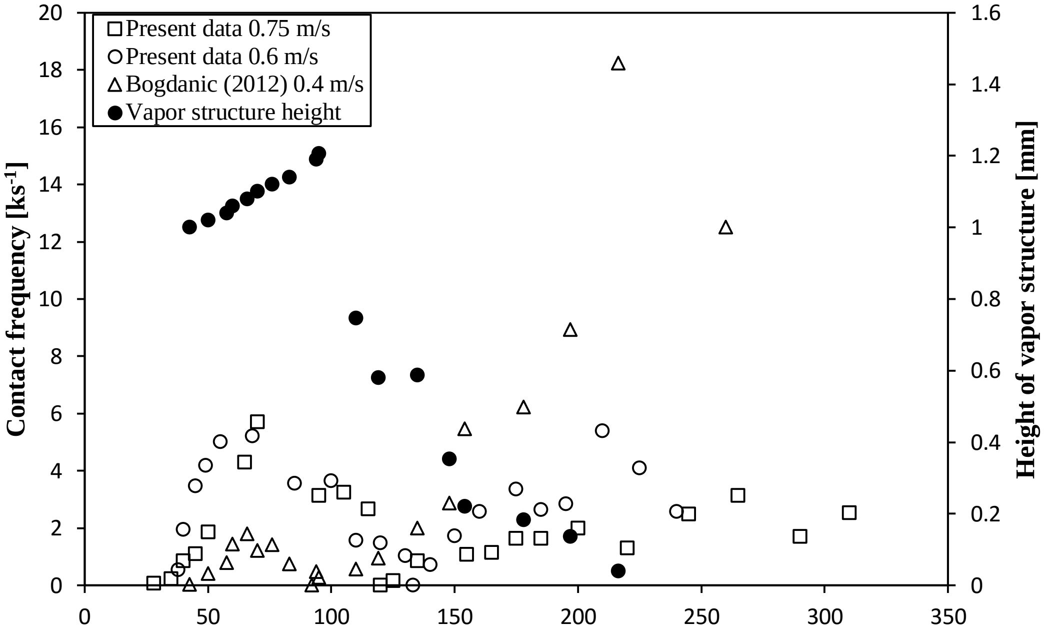

Figure 4.7: Contact frequency and height of vapor structure measured using optical probe. Obtained from Bogdanic et al. [48]

as shown in Table. 4.1.

Table 4.1: Current model validation data

Experiment No.	Authors	V_j [m/s]	Re_L [2]	ΔT_{sub}[°C]	ΔT_{min} [°C]	Use
1	Bogdanic et al. [48]	0.4	3,200	20	285	Training
2	Robidou et al. [42]	0.7	5,600	7	280	Validation
3	Robidou et al. [42]	0.7	5,600	17	380	Validation
4	Robidou et al. [42]	0.8	6,400	17	360	Validation
5	Ahmed and Hamed [19] [1]	0.6	4,800	15	460	Validation
6	Ahmed and Hamed [19] [1]	0.75	6,000	15	450	Validation

The heat flux has been calculated under the conditions of experiment No. 1 reported by Bogdanic et al. [48], as shown in Fig. (4.8). The estimated heat flux matches the experimental heat flux in the transition region. Although the model is not developed for nucleate boiling, the increase in the heat flux is proportional to the increase in the measured vapor break-up frequency.

The wall heat flux is the sum of two components: the liquid quenching component and the liquid intrusion component. From Eq. (4.13) and Eq. (4.10), the quenching component is proportional to constant B, the degree of superheat and the square root of the break-up frequency, $q_q \propto B\,\Delta T_{sup}\,\sqrt{f}$. Similarly, the intrusion component is proportional to the vapor structure height and instability growth rate, $q_i \propto A\,h_v^4$ where $\omega \propto h_v^3$.

Fig. (4.9) shows the contribution of the two components to the wall heat flux. Although, the weight of the liquid quenching, B, decreases with the increase of surface temperature, the frequency and degree of superheat increase. The liquid quenching component is 60% of the wall heat flux at the CHF and up to 90% at the shoulder boiling. The liquid intrusion component weight, A, increases with the surface temperature. However, the vapor height decrease is more significant than the increase in A.

---

[1] Current work

[2] Reynolds number is based on jet width, w

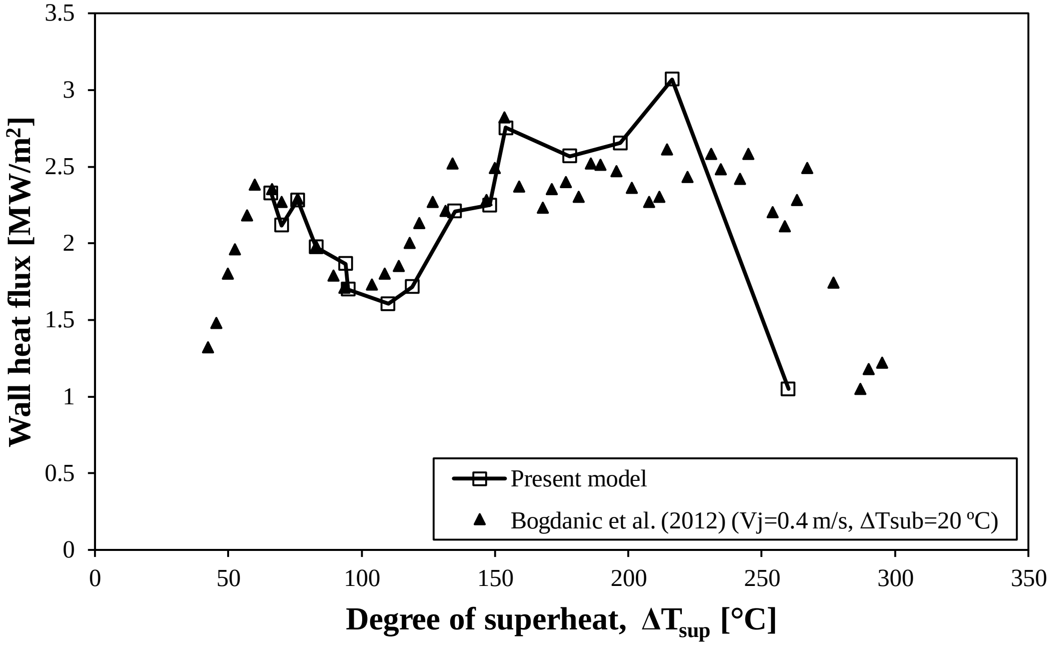

Figure 4.8: Comparison of the experimental data reported by Bogdanic et al. [48] and the heat flux obtained from the present model Eq. (4.10)

The estimated heat flux from the model for experimets No. 2 & 3 is shown in Fig. (4.10) and for experiments No. 5 & 6 is shown in Fig. (4.11).

The comparison of the estimated heat flux using the proposed model with the corresponding current experimental data and data reported in the literature is shown in Fig. (4.12). The model follows the trend of the boiling curve from the CHF to the Leidenfrost point with a local minimum point (the first minimum). The model estimates the first minimum heat flux with a maximum error of 38% and the degree of superheat it occurs at with a maximum error of 19%. Close to the end of the shoulder flux, the model does not show good agreement with the experimental data. The reason is the incomplete frequency and vapor height data till the film boiling incipience.

The range of applicability of the model is limited by the available vapor break-up frequency and vapor layer height; no frequency data is available close to Leidenfrost

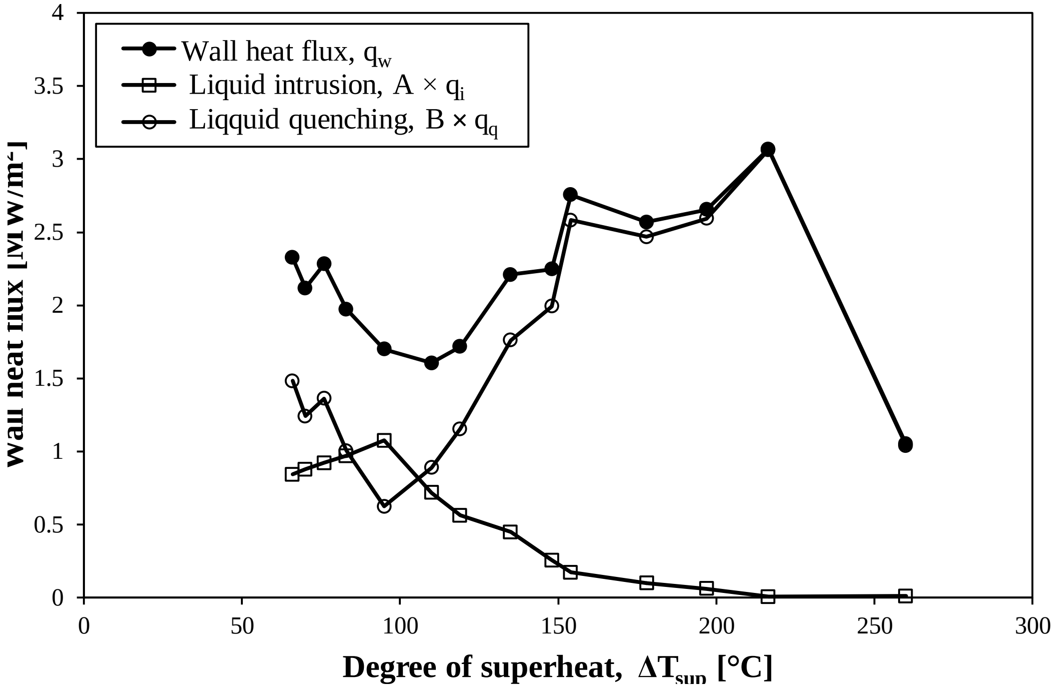

Figure 4.9: Wall heat flux and the two heat components Exp.1

point. The frequency is expected to drop sharply as the instability is decayed and a stable vapor film is formed.

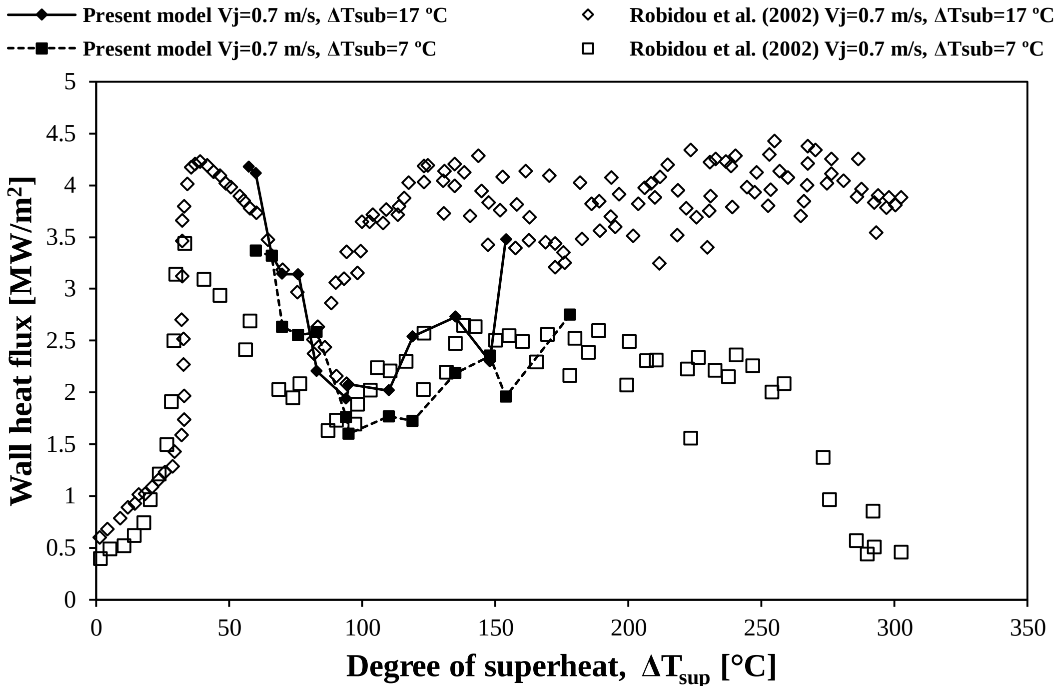

Figure 4.10: Comparison of the experimental data reported by Robidou et al. [42] and the heat flux obtained from the present model Eq. (4.10)

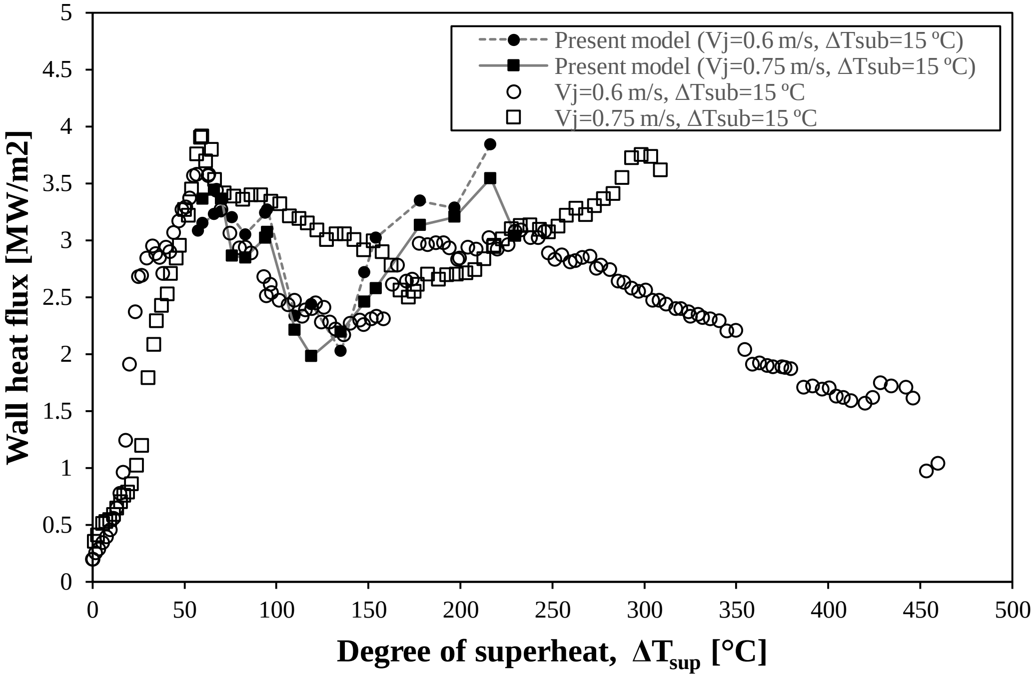

Figure 4.11: Comparison of the present experimental data and the heat flux obtained from the present model Eq. (4.10).

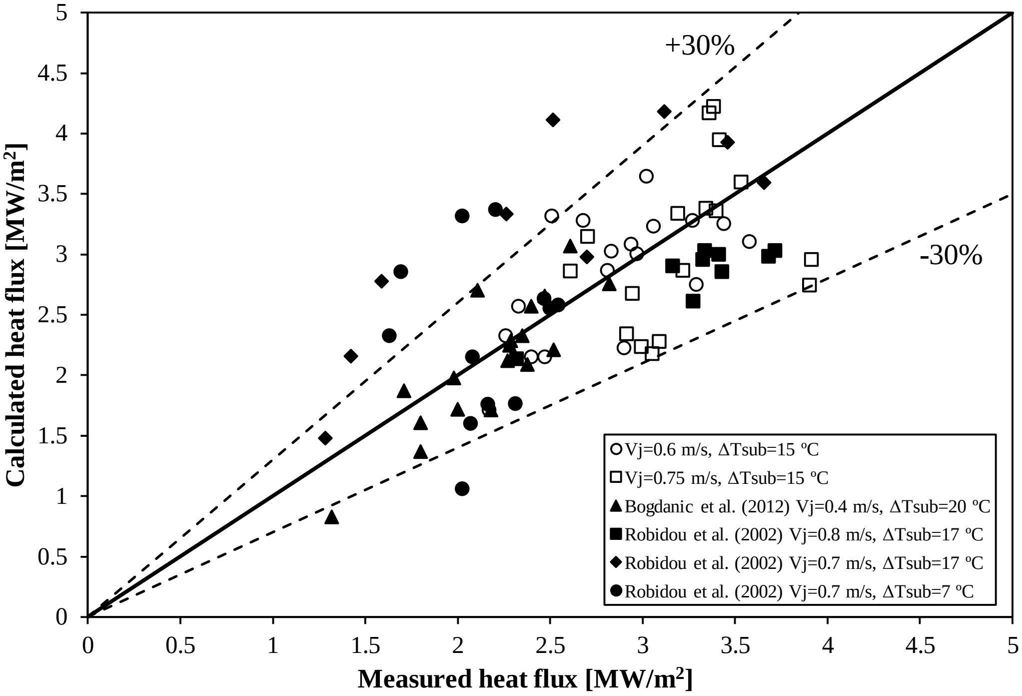

Figure 4.12: Estimated heat flux Eq. (4.10) versus corresponding experimental heat flux from CHF to $\Delta T_{sup} = 215\,^{\circ}\mathrm{C}$

4.4 Effect of Frequency and Vapor Height

The model is sensitive to re-wetting cycle frequency and vapor layer height. It is crucial for modeling heat flux at transition boiling to get accurate measurements of cycle frequency and vapor structure height.

Unfortunately, not all the experiments have frequency and vapor height measurements. Table 4.2 lists the available data for both frequency and vapor height. Non-measured values are either scaled based on measured data from Bogdanic et al. [48] or Ahmed and Hamed [19] or directly used as measured without scaling.

Table 4.2: Frequency and vapor height data

Experiment No.	Authors	Frequency	Vapor Height
1	Bogdanic et al. [48]	Measured	Measured
2	Robidou et al. [42]	From Exp.6	From Exp.1
3	Robidou et al. [42]	From Exp.6	From Exp.1
4	Robidou et al. [42]	From Exp.6	From Exp.1
5	Ahmed and Hamed [19]	Measured	Scaled
6	Ahmed and Hamed [19]	Measured	Scaled

Scaling is based on matching three points between experiments: the CHF, the first minimum and the Leindenfrost point. The trend between each two points is assumed to depend only on the degree of superheat. For the vapor height, the trend from CHF to the first minimum is assumed linear while from the first minimum is fitted as a polynomial.

Scaling the vapor height was found to have effect on the shoulder boiling heat flux and insignificant effect on the CHF and the first minimum, as shown in Fig. (4.13). On the contrary, scaling the frequency has a pronounced effect on the CHF and the first minimum and minor effect on the shoulder boiling. Accurate frequency measurements is essential for modeling the heat flux. The next chapter shows how re-wetting frequency is collected, analyzed and modeled.

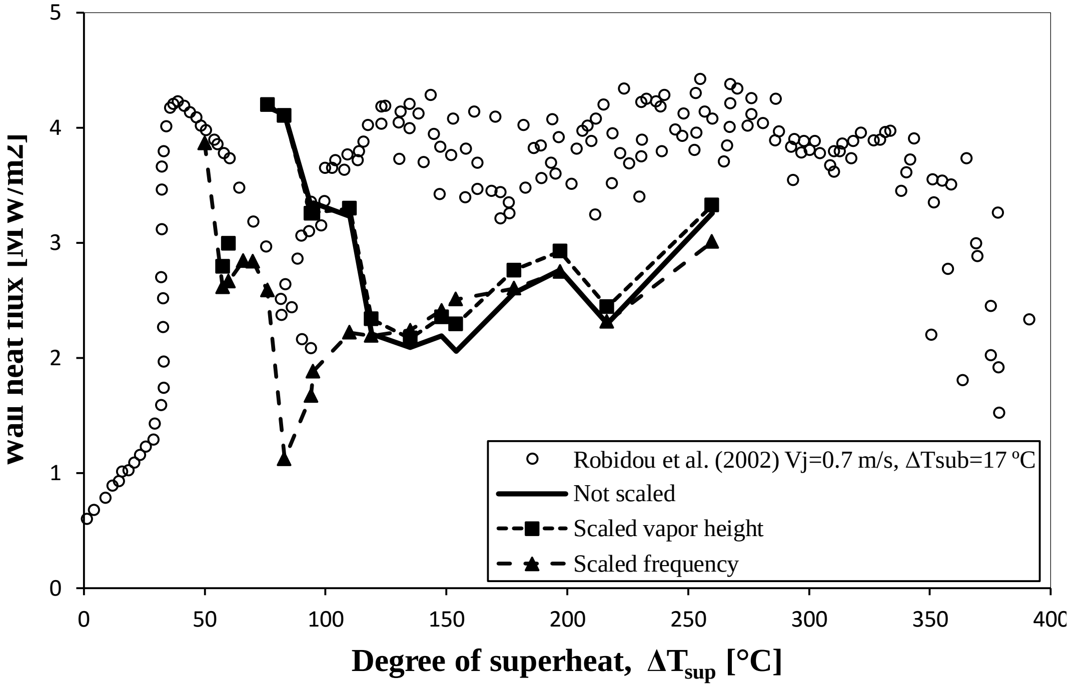

Figure 4.13: Effect of frequency and vapor height scaling

4.5 The Minimum Heat Flux

At the minimum heat flux, both frequency and vapor height reach very low values. Rayleigh Taylor instability is suppressed at the Leidenfrost point as the growth rate drops dramatically [59]. The most critical growth rate is proportional to the third power of the vapor height, $\omega_d \propto h_v^3$ [63]. As the vapor film forms, the interface perturbations are suppressed and any instability is decayed.

At low vapor heights the perturbations will not grow, but the possibility for the liquid to touch the surface increases and the break-up frequency is significant.

It is believed that the frequency goes to zero at the Leidenfrost point. Due to technological difficulties, the available measurements of the break-up frequency do not extend to the Leidenfrost point and the trend of the frequency is not known. Although it is not supported by measurements, formation of stable vapor film strengthen the conclusion of decaying frequency and vapor height.

Chapter 5

Surface Re-wetting Frequency

Processing the fiber optic probe signal is crucial for sound analysis of surface wetting. The surface re-wetting frequency is modeled and validated using the optical probe measurements collected at the proximity of the surface.

5.1 Signal Processing

The single threshold technique, shown in Fig. (5.1), is used for phase determination. If the voltage signal is below a predefined certain threshold, the phase is defined as liquid and the opposite is true. Single threshold method is the simplest method to determine Fluid Phase Function (FPF).

The selected threshold voltage is required to be lower than any high voltage (vapor) oscillations and higher than any low voltage (liquid) oscillations. By smoothing the signal, fast transitions are counted as change in phase while slow transitions are considered as noise. Oscillations in the voltage level in the vapor phase are ignored. This conclusion is based on preliminary experiments, presented in Section 2.3.1, carried out to evaluate probe behavior and the level of the cut-off voltage.

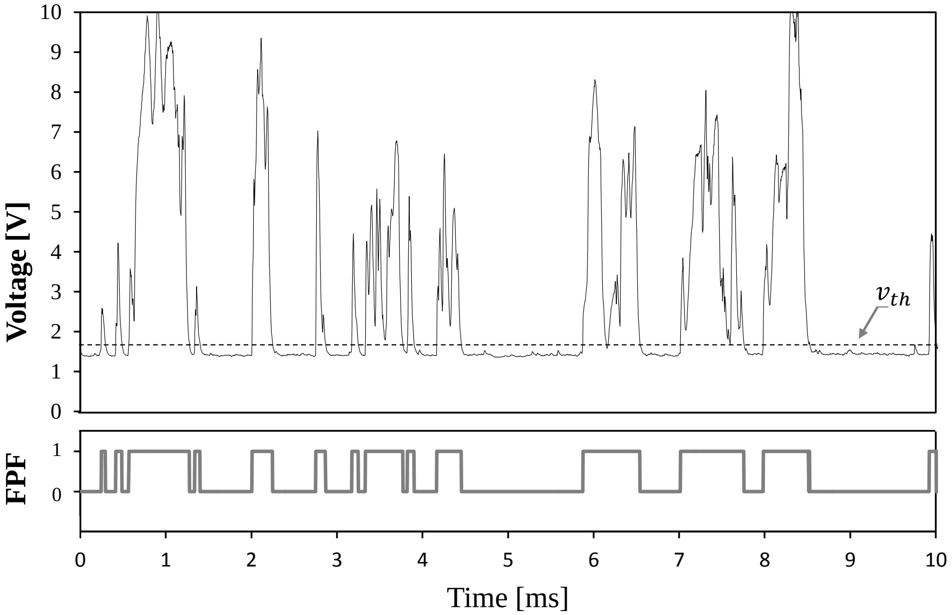

Figure 5.1: Sample of the phootodiode signal and the FPF

FPF is defined such that [64],

$$FPF\,(y,t) = \begin{cases} 0 & V < V_{th}\,(liquid) \\ 1 & V \geq V_{th}\,(vapor) \end{cases} \tag{5.1}$$

where V_{th} is the threshold voltage. To eliminate counting short period oscillations as change in phase, the signal is filtered and smoothed. MATLAB low pass filter is applied on the signal, as shown in Fig. (5.2). The filter ignored the short period oscillations in voltage level around the threshold voltage. One of the problems with filtering is losing part of the data. The time at which phase change occurs are incorrectly shifted due to the smoothing accompanied by the filtering. The error in the phase change location was found to be insignificant and has a maximum value of 40 μs.

As the FPF is expected to follow certain periodic behavior, statistical auto-correlation is used to find the a correlation between the function and itself. The

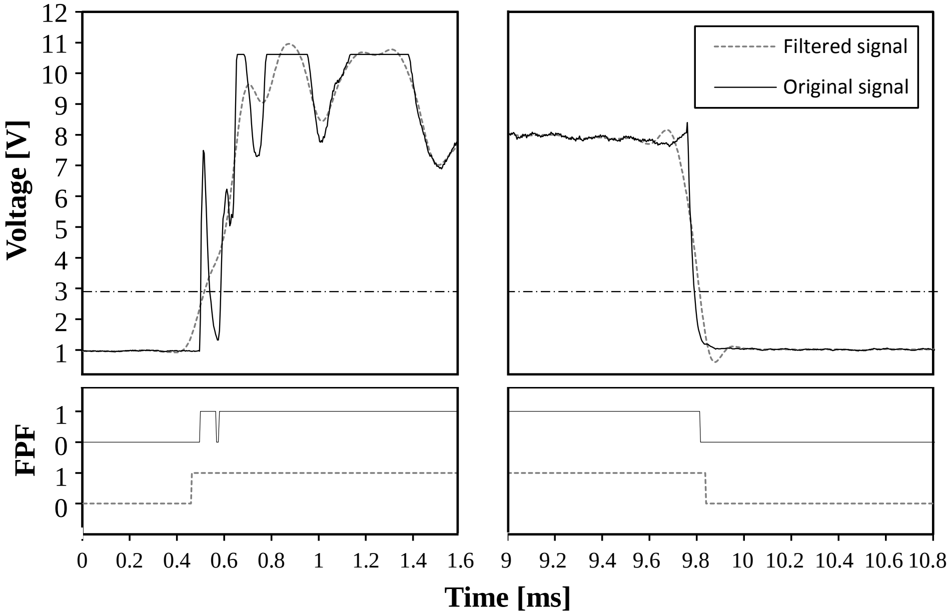

Figure 5.2: Filtered vs. original signal

periodicity of the FPF can then be determined. This procedure does not always return good results. The number of phase changes, N, is counted. Liquid/vapor contact frequency is obtained from,

$$f = N/t_s \tag{5.2}$$

where t_s is the sampling time. After calculating the frequency, the time taken while each phase in contact with the probe is counted. Void fraction is defined as the sum of vapor time to the total sampling time. The time averaged void fraction can be simplified as,

$$\alpha(y) = \frac{1}{t_s}\int_{t_s} FPF(y,t)\,dt = \frac{1}{t_s}\sum_{i=1}^{N} t_v(i) \tag{5.3}$$

where t_v is the vapor time. The liquid fraction is calculated in a similar manner. A full analysis of surface re-wetting can not be completed without vapor and liquid time distribution. A histogram of both liquid time and vapor time is obtained.

The frequency at the surface is shown in Fig. (5.3) for the same conditions as the boiling curve in Fig. (4.1). The frequency increases with the increase in the surface degree of superheat till it reaches its maximum at the CHF. The frequency then decreases until the first minimum which is followed by a second increase during the shoulder region.

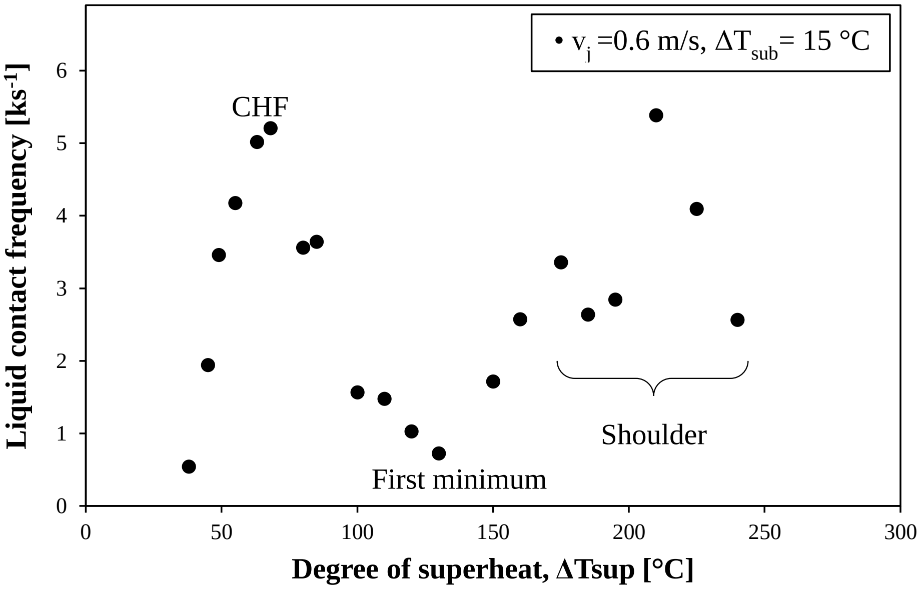

Figure 5.3: Frequency at the surface $V_j = 0.6\,\mathrm{m/s}$ and $\Delta T_{sub} = 15\,°\mathrm{C}$.

Total vapor time and the variation of vapor (void) time fraction with the surface degree of superheat is shown in Fig. (5.4). The void fraction increases, as expected, till the CHF. While void fraction is expected to keep increasing till the first minimum, it decreases dramatically from the CHF to the first minimum. To assess this fact, the void fraction only is not enough; the distribution of the time over different contact time periods needs to be assessed. The distribution is shown in the same figure.

Vapor contact instance happens over a certain time. Then it is followed by time where the probe is in contact with liquid. The distribution of the instant time periods

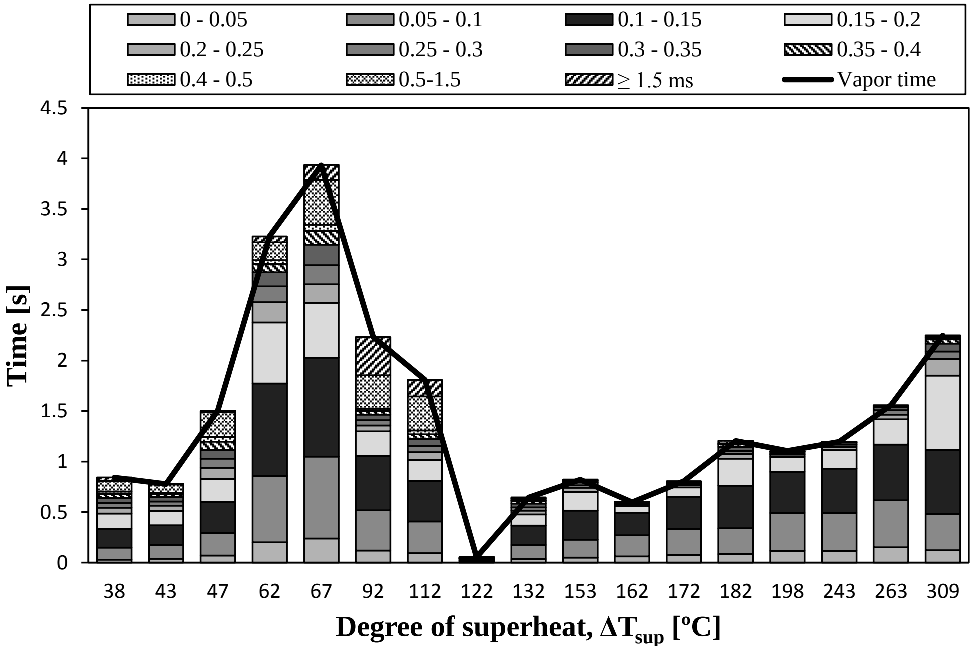

Figure 5.4: Vapor time fraction

over these distinct contact instances is shown in Fig. (5.5) for vapor and Fig. (5.6) for liquid. The vapor phase is observed to last, on the surface, for short periods of time up to 1.5 ms while liquid contact instances time ranges from 0 to 20 ms.

Close to the CHF, corresponding to high contact frequencies, the vapor time is mainly due to contact over short periods of time, < 1.5 ms, while liquid time is mainly distributed over longer periods of time, $1.5 - 20$ ms. While close to the first minimum, the liquid occurs mainly over longer periods of times, > 20 ms. This is aligning with the frequency measurements, as the frequency is inversely proportional to the summation of the two times. Long periods of liquid contact means less alternation between phases and hence low frequency, as shown in Fig. (5.7).

The vapor phase time is expected to increase and be of a maximum value at the first minimum to cause full blanketing of the surface and hence hinder the heat flux. The previous explanation is valid for the Leidenforst point, but not in the transition boiling

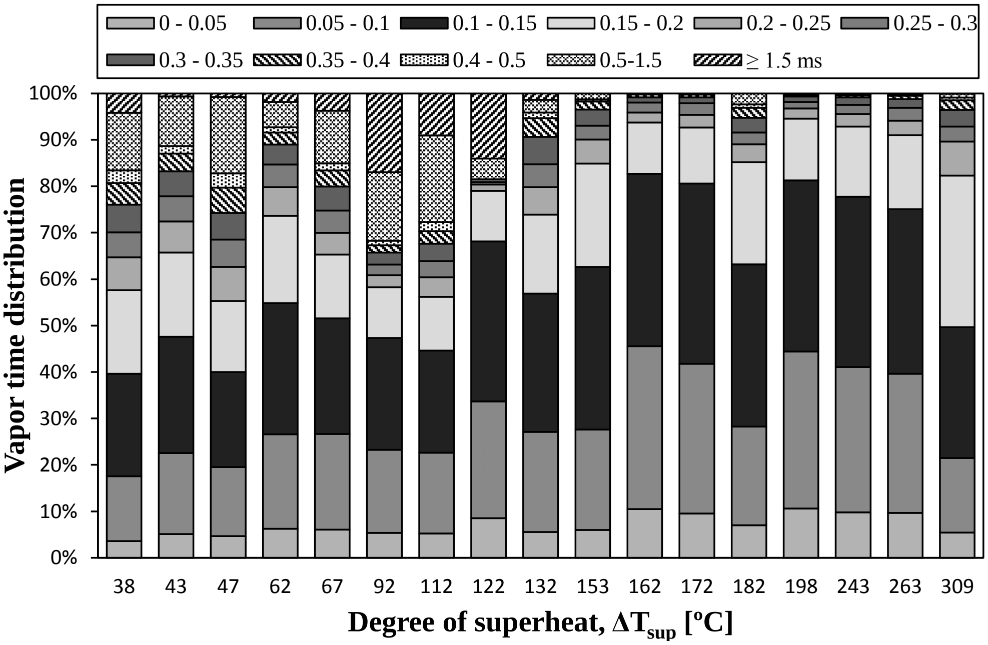

Figure 5.5: Vapor contact time distribution

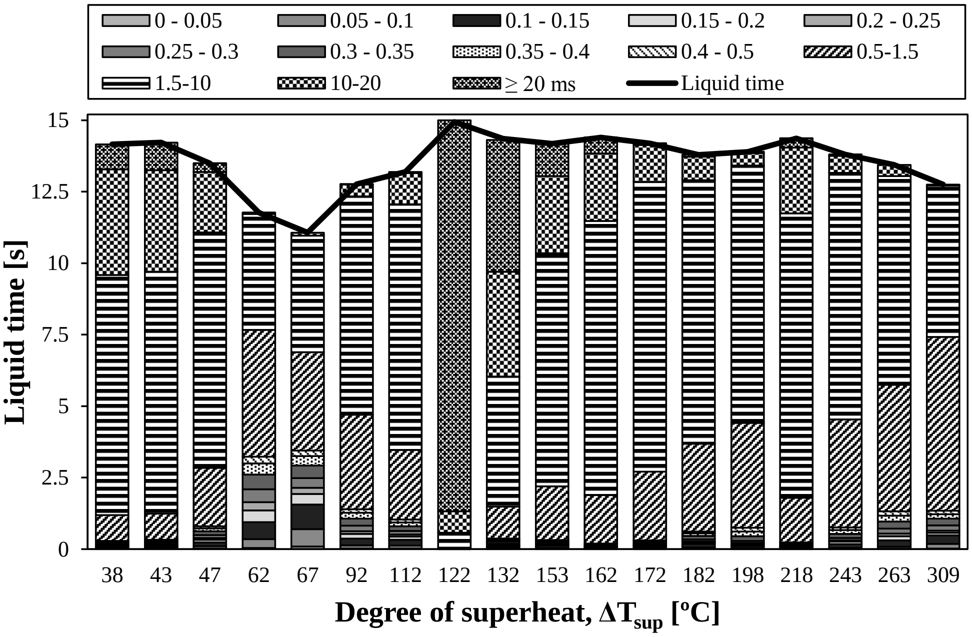

Figure 5.6: Liquid contact time distribution

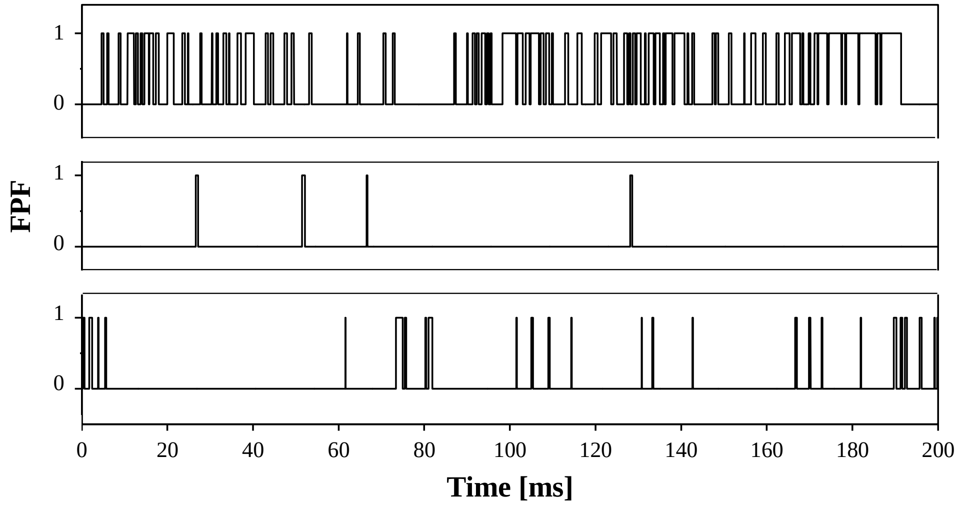

Figure 5.7: FPF for CHF (top), first minimum (middle), and shoulder (bottom)

case. As discussed in Section 4.3, the heat is transferred by transient conduction. Longer periods of liquid contact with the surface means greater energy extracted from the surface and less instant heat flux. More rapid transition between phases means that the time average heat flux is high, as schematically shown in Fig. (5.8).

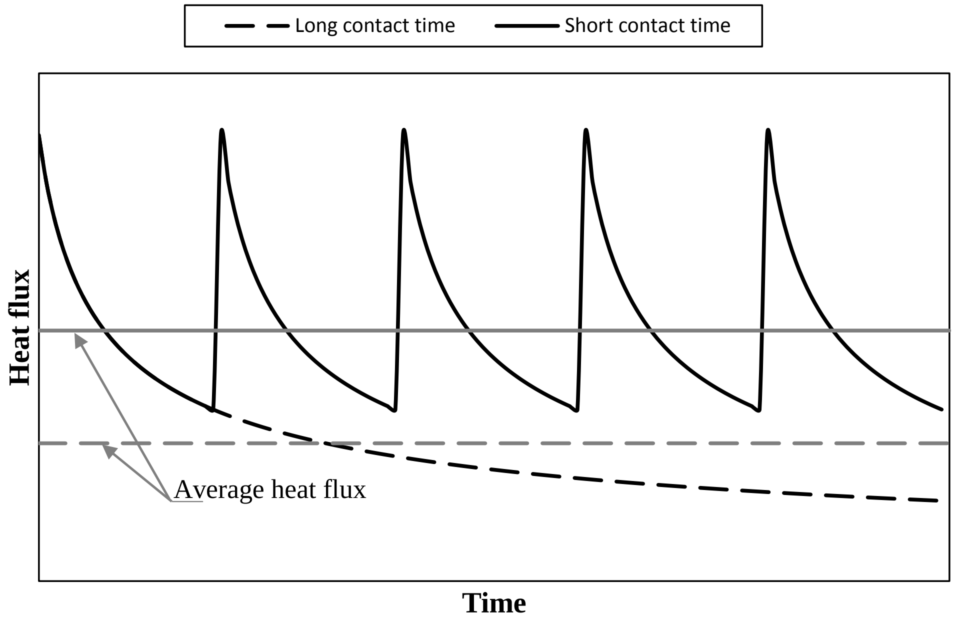

Figure 5.8: Average heat flux for short and long liquid contact time

5.2 Frequency Modeling

The boiling surface goes through periodic cycles of wetting and dry-out in the transition boiling regime. There are two re-wetting mechanisms observed from high speed images of the boiling surface, discussed in Section 4.1. The first mechanism, more frequent in the region from the CHF to the first minimum, is a result of vapor pocket break-up by the jet and direct surface contact is observed. The second mechanism, more pronounced from the first minimum to the Leidenfrost point, is by liquid intrusions into the vapor layer controlled by Rayleigh-Taylor instability.

The frequency of the break-up and formation cycle, shown in Fig. (5.3), can be assumed to be due to the turbulence caused by the jet in the region from CHF to the first minimum and due to the liquid intrusions beyond the first minimum point. The wetting starts with liquid intrusions and ends with the evaporation of the liquid touching the surface.

From the previous discussion, vapor layer break-up frequency can be expressed as,

$$f = \begin{cases} f_J & \Delta T_{CHF} < \Delta T_{sup} < \Delta T_{fm} \\ f_I & \Delta T_{fm} \leq \Delta T_{sup} < \Delta T_{min} \end{cases} \tag{5.4}$$

where f_J is the frequency of break-up because of the jet and f_I is the frequency caused by liquid intrusions.

5.2.1 Jet Dynamics Break-up Model

There are many studies on the break-up of an immiscible fluid bulk immersed in a flow. The importance of these studies comes from the study of jet atomization and droplets break-up. Taylor Analogy Break-up (TAB) model is one of the widely used models to describe the break-up of a liquid droplet sprayed in air [65]. The model is developed based on the analogy between a distorting liquid bulk and a spring mass system. Surface tension forces represent the spring restoring force. The drag force on the bubble is similar to the external forces on the mass. Liquid viscosity is similar to the damping force. The basic assumption is that the droplet is oscillating under the fundamental mode and break-up occurs at the first oscillation.

TAB model can be similarly used to estimate the break-up of a vapor pocket under the jet. The model takes the form,

$$F - kx - c\frac{dx}{dt} = m\frac{d^2x}{dt^2} \tag{5.5}$$

where x is a displacement of the bubble equator from its spherical shape. The coefficient of the equations are,

$$\begin{aligned}\frac{F}{m} &= C_F\frac{\rho_l V_j^2}{\rho_g r}\\ \frac{k}{m} &= C_k\frac{\sigma}{\rho_v r^3}\\ \frac{c}{m} &= C_d\frac{\mu_v}{\rho_v r^2}\end{aligned} \tag{5.6}$$

where $C_F = 3/16$ is obtained from the drag force on sphere. C_k and C_d are obtained by matching the fundamental oscillation frequency for the case of a droplet [65]. Using the non-dimensional parameter, $y = 2x/r$, Eq. (5.6) can be solved assuming constant relative velocity and distortion started from spherical shape to take the form,

$$y = We_c - \left[We_c \cos\omega t + \frac{We_c}{\omega t_d}\sin\omega t\right] e^{-t/t_d} \tag{5.7}$$

where,

$$\begin{aligned}We_c &= 2\frac{C_F}{C_k}We\\ We &= \frac{\rho_l V_j^2 r}{\sigma}\\ \frac{1}{t_d} &= \frac{C_d}{2}\frac{\mu_v}{\rho_v r^2}\\ \omega^2 &= C_k\frac{\sigma}{\rho_v r^3} - \frac{1}{t_d^2}\end{aligned} \tag{5.8}$$

The breakup is assumed to happen whenever the distortion, x is equal to half the droplet radius, r, i.e. $y = 1$. Break-up time, based on TAB model assumptions, is found to be 3.5 ms. From Fig. (5.5), the most probable vapor time is in order of 10^{-1} ms. TAB model overestimates the vapor break-up time by one order of magnitude. The reason behind the overestimation might be that the model only consider the drag force on the vapor pocket, while the vapor pocket at the stagnation is subjected to an extra turbulence caused by the jet at the stagnation region.

While TAB model studied atomization of a liquid droplet sprayed into different medium, different studies studied air particles in a jet flow. When a volume of immiscible fluid of different properties is immersed in turbulent jet flow, it breaks-up into smaller volumes [66]. The turbulence caused by the main fluid is the main cause of break-up. Fragmentation frequency can be modeled knowing flow kinetic energy and mean square value of velocity fluctuations [67]. Coulaloglou and Tavlarides [68] assumed that the eddy turnover time can be used to determine the break-up time. With the assumption of homogeneous turbulence, fragmentation frequency is expressed as,

$$f_J = a\left(\frac{\varepsilon}{D^2}\right)^{\frac{1}{3}} \exp\left(b\frac{\sigma}{\rho\varepsilon^{2/3}D^{5/3}}\right) \tag{5.9}$$

where ε is the turbulent dissipation, a and b are experimental constants, D is the diameter of a sphere has equivalent volume to the vapor pocket.

As this model is developed for flow with no stagnation points, Timm et al. [69] showed that the turbulence caused by the jet is governed by the rapid growth and condensation of vapor pockets. At high population of bubbles, laminar boundary layer is not existent close to the surface and the maximum diffusivity near the wall is expressed as,

$$\varepsilon_{max} \sim \frac{F{r_b}^2}{0.5t_b} \tag{5.10}$$

where F is the area fraction of the surface covered with bubbles, r_b is time average maximum bubble radius, t_b is the mean bubble life time.

Omar et al. [70] studied the turbulent mixing under the jet. The existence of vapor voids on the surface enhance the mixing and hence the heat transfer. It results in an additional diffusivity that is correlated in a dimensionless form as,

$$\varepsilon = \frac{Re_D^{-0.7} Ja_{sup}^{4.2} Ja_{sub}^{-1.6}}{We_D^{4.3} + 5.6} \tag{5.11}$$

It is clear that the increase in the jet momentum and degrees of subcooling would result in decrease in the dissipation. While degree of superheat has a positive effect on the diffusivity.

5.2.2 Liquid Intrusion Break-up

As the liquid-vapor interface become unstable under Rayleigh-Taylor instability, liquid intrude into the surface in the form of columns of diameter equal to half the most dangerous instability wave length, $\lambda_d/2$ [55]. The intruded liquid traps volumes of vapor between the columns and heat is transferred mainly by transient conduction to the liquid. Once the liquid touching the surface reaches saturation, it evaporates and the vapor pockets get connected and evict the liquid back to the bulk liquid. The re-wetting cycle frequency can be assumed to be inversely proportional to the time required for the liquid to evaporate, $f \propto 1/t$. Liquid layer evaporation frequency can be expressed as,

$$\frac{1}{f_I} = -c_i \frac{\rho \, h_v \, Cp}{h} \ln\left(\frac{T_{sat} - T_\infty}{T_l - T_\infty}\right) \tag{5.12}$$

where, c_i is an empirical coefficient depends on jet velocity and degree of subcooling expressed as,

$$c_i = 0.8\, v_j^{2.3}\, \Delta T_{sub}^{2.5} \tag{5.13}$$

h_v is the vapor layer height, h is the heat transfer coefficient, T_∞ is the surroundings temperature which is assumed to be equivalent the film temperature ($T_f = (T_w + T_l)/2$), and T_l is the liquid temperature.

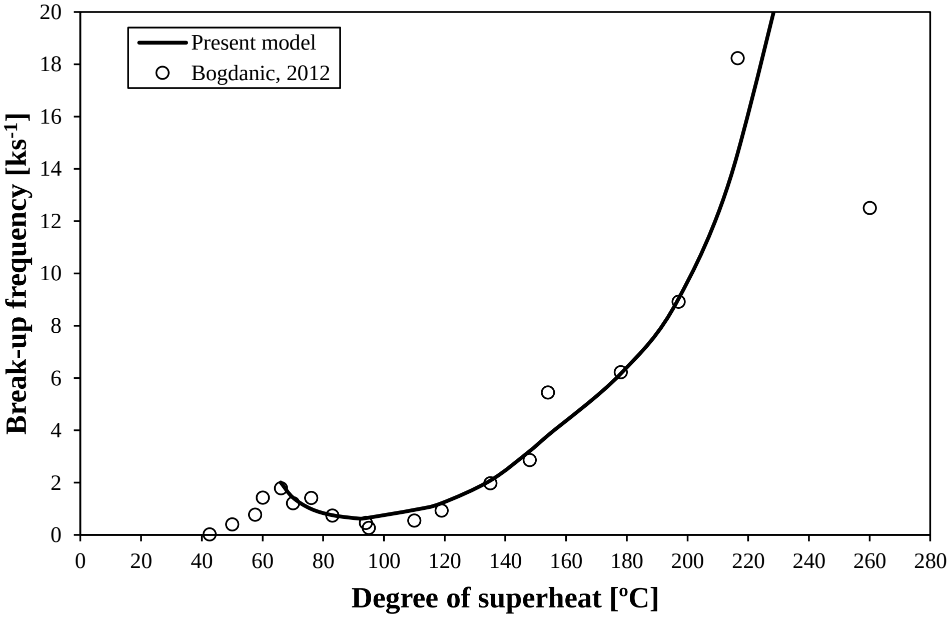

Figure 5.9: Vapor break-up frequency obtained by Bogdanic et al. [48] and the current model

Fig. (5.9) and Fig. (5.10) show the values of the break-up frequency estimated from Eq. (5.4) against experimental data from the literature (0.4 m/s jet velocity and 15 °C degree of subcooling) [48] and present data (Fig. (5.3)), respectively. The model shows good agreement with the experimental data. The model does not follow the experimental data close to CHF and at high degrees of superheat. Jet dynamics break-up models based on force balance (TAB model) or based on the flow turbulence

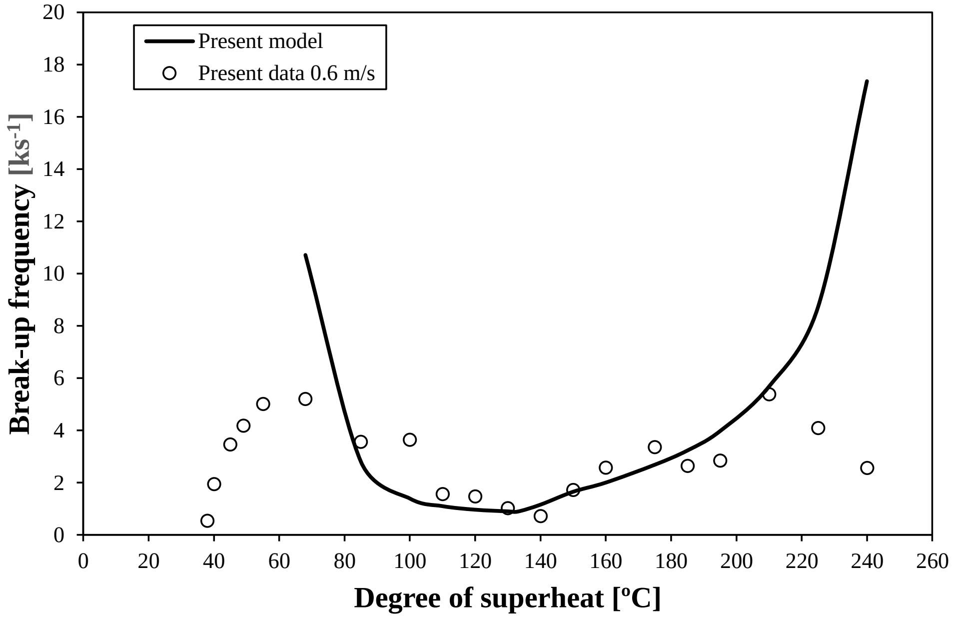

Figure 5.10: Vapor break-up frequency present data and the current model

are not representing the decrease in the frequency from CHF to the first minimum well. Experimental data from the literature and from the present work are plotted against estimated frequency, as shown in Fig. (5.11). The proposed model showed a total normalized root square mean error (NRSME) of 25%.

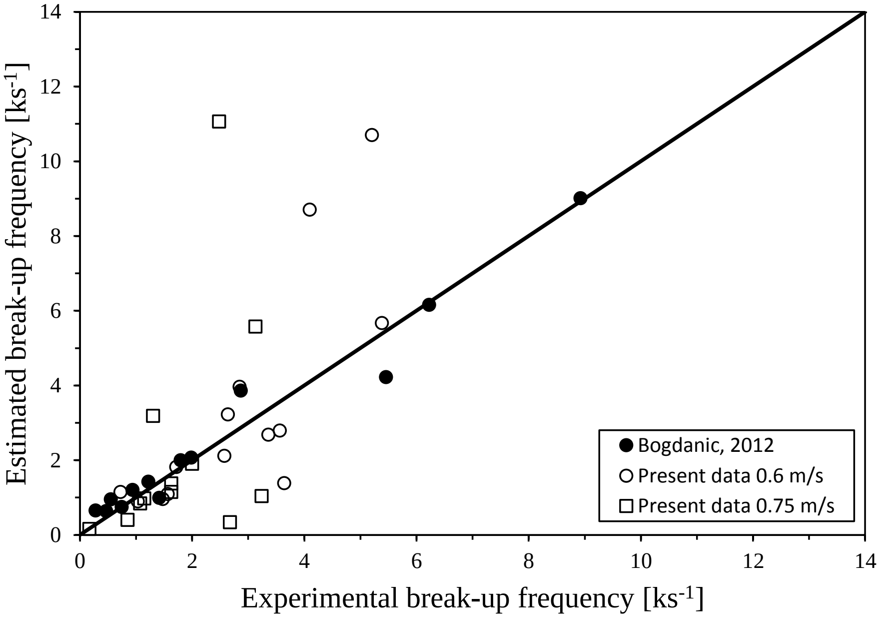

Figure 5.11: Frequency experimental data vs. present model estimation

5.3 Relation between Vapor Height and Frequency

Bogdanic et al. [48] measured vapor layer height under an impinging jet in the stagnation region beyond the first minimum. Vapor height is inversely proportional to the cycle break-up frequency, $h_v \propto 1/f$. Modeling the vapor height is crucial in finding the cycle break-up frequency. Many studies have been carried out in the nucleate boiling regime and concluded that bubble release frequency and the bubble departure diameter are related as follows [33, 71–73],

$$fD^m = k\left[\frac{g(\rho_l - \rho_v)}{\rho_l}\right]^n \tag{5.14}$$

where $m = 1$ and $n = 0.5$, k is a proportionality constant and is equal to 0.2. Although the previous relation is developed for nucleate boiling, it can represent the vapor structure height in the transition boiling regime. The vapor layer height is estimated with a NRSME of 23%.

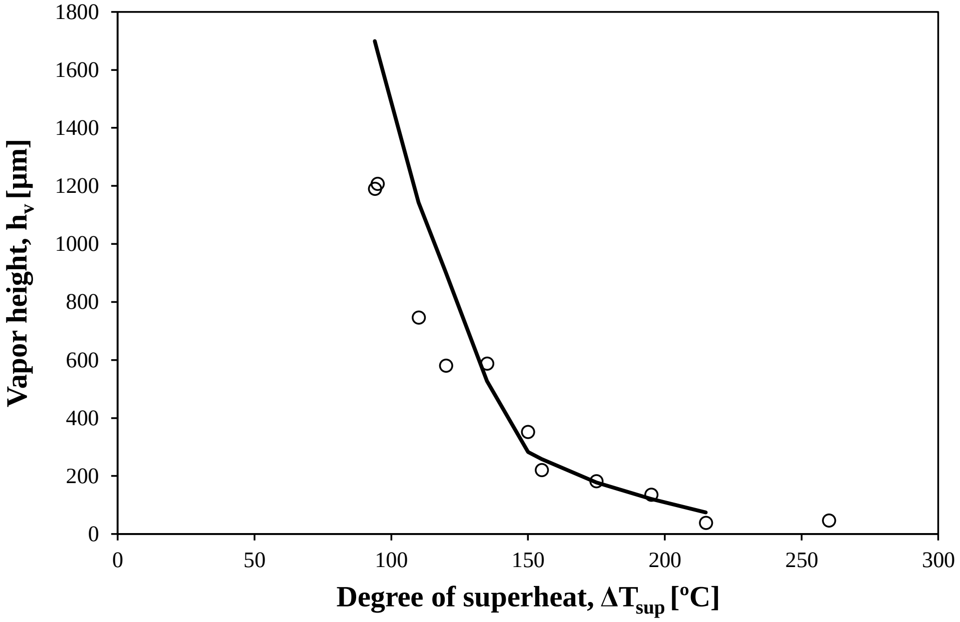

Figure 5.12: Estimated vapor height

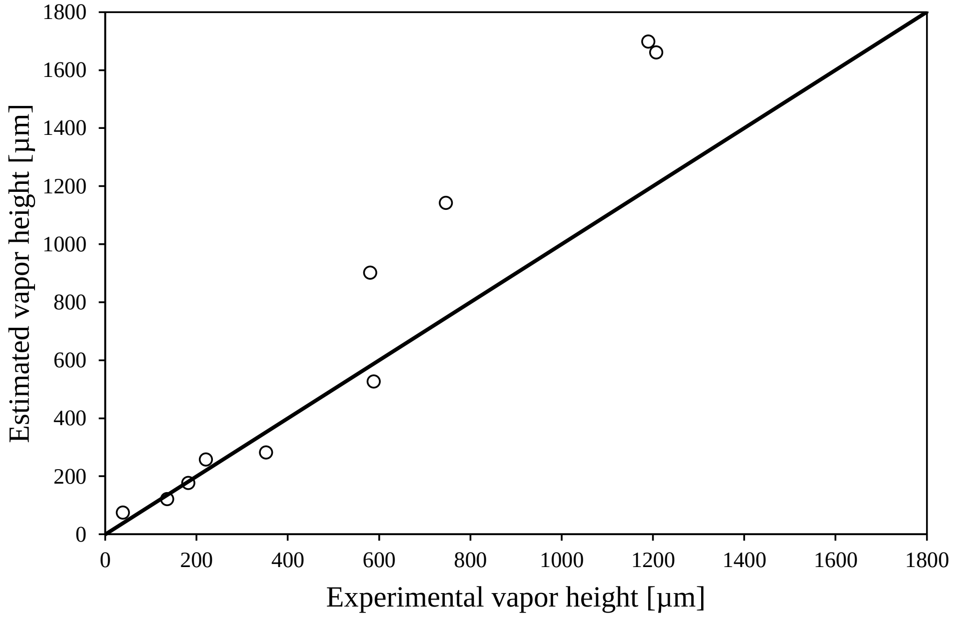

Figure 5.13: Vapor height experimental data [48] vs. present model estimation

Chapter 6

Summary and Conclusions

The current work is based on experimental study of nucleate and transition boiling under an impinging planar water jet. **For the nucleate boiling (Chapter 3)**, bubble growth is studied in both stagnation and parallel flow region. The modified Zuber model for non-uniform temperature field is found to best fit the experimental data with different b values. $b = \pi/7$ is found to best describe the data in the stagnation region and $b = 5\pi/6$ for the parallel flow compared to $b = \pi/10$ proposed by Omar [18].

New forces are introduced acting on bubbles growing under the jet. The jet is found to cause extra two forces: asymmetric bubble growth force in a moving fluid and pressure hydrodynamic force caused by the jet stagnation. The extra forces are anchoring the bubble and the force balance estimate bigger departure diameter than observed.

For the transition boiling (Chapter 4 and chapter 5), the high temperature design allows for the surface to reach temperatures up to 560 °C. As a result, the full boiling curve is obtained. From the boiling curve, a second increase in the heat flux is observed after the classical decrease in the transition boiling regime. The increase resulted in a local minimum point called the first minimum. The heat flux after the second increase is characterized by a region of constant heat flux called, the shoulder boiling. The difference in the boiling curve of flow boiling and jet boiling is due to the rapid and continuous vapor layer breaking up and formation.

Two mechanisms for vapor break-up is hypothesized based on experimental observations. *The first mechanism* is breaking due to turbulence caused by the jet in the stagnation region. *The second mechanism* which is more frequent at higher temperatures is due to the Rayleigh-Taylor instability. As the temperature increases, more vapor covers the surface and RT instability comes to play. Liquid column intrusions are observed. The frequency of the breaking-up is modeled based on these two hypotheses.

A new wall heat flux partitioning model is introduced based on the current physical understanding, the two components of the model are assumed to have weighted contribution to the total heat flux. Although the two components are simple, they are based on physical understanding supported with experimental observations.

Chapter 7

Future Work

The current work is a breakthrough in the mechanistic modeling of boiling under the jet. However, many challenges have limited the ability to expand laterally, to cover more aspects of boiling under the jet and longitudinally, to study vapor structure under the jet in depth. The following lists recommendations for future work.

Recommendations for future work

- Expand the transition boiling study by exploring more stable control techniques and revolutionize the heating element design
- Study the vapor break-up under unbounded jets
- Study vapor formation under the jet
- Study the effect of wall superheat and liquid subcooling on the vapor formation and break-up

- Use multiple optical probes or spatial probes (like conductance probe) instead of one point probe
- Improve optical probe signal processing
- Understand the frequency trends
- Expand Taylor Analogy Break-up (TAB) to model vapor break-up.
- Study vapor break-up frequency at high degrees of superheat. It is expected to decrease till it reaches minimum at the Leidenfrost point.
- Model the first minimum degree of superheat based on both frequency and the heat flux
- Understand vapor formation at the Leidenforest point
- Use of micro-thermocouples for surface temperature mapping
- USe faster high speed imaging for finer bubble growth data

Appendix A

Uncertainties and Error Analysis

The accuracy of the heat fluxes models develop in this work, depend on the error in the values of the measured parameters.

Measured temperature

Thermocouples were used through out this study in measuring the temperature at specific locations in the copper block. Thermocouples are mechanically inserted in a transition fit holes in the copper block. The holes are filled with thermal oil and high temperature epoxy was used to secure the thermocouples in place and seal the hole. Type-k thermocouples of a 0.5 mm junction diameter were used. The manufacturer reported uncertainty for this kind of thermocouples is ±0.1 °C. For each individual thermocouple, the temperature is based on the average of a number of measurements. Uncertainty in temperature measurements is at a maximum of 0.03 °C in the nucleate boiling and 0.3 °C in the transition boiling regime. The cold junction compensation in the DAQ SCXI-1102 is ±0.5 °C. The total combined uncertainty is obtained from the following relation,

$$u = \sqrt{u_m^2 + u_s^2 + u_{CJ}^2} \tag{A.1}$$

where u_m is the manufacturer uncertainty, u_s is the sampling uncertainty, u_D is the DAQ uncertainty. The total uncertainty for a 95% confidence level is 0.59 °C. The maximum variation in temperature in the transition boiling regime is ±5 °C.

Thermocouples location

The thermocouples are inserted half way through the copper block all the way to the bottom of the drilled holes. The holes were drilled with a precision drill. The uncertainty in the depth is ±0.001 mm while it is X and Y locations were within ±0.005 mm of the desired location.

Heat flux

The estimation of the uncertainty is not a straight forward. Under the assumption of 1-D heat transfer where, $q = -k\, dT/dx$ the combined uncertainty is expressed as,

$$\frac{u_q}{q} = \sqrt{\left(\frac{u_{\Delta T}}{\Delta T}\right)^2 + \left(\frac{u_{\Delta x}}{\Delta x}\right)^2} \tag{A.2}$$

The uncertainty from Eq. (A.2) is 8.5 kW/m^2.

An inverse heat conduction code, INTEMP, has been used to solve for the surface heat flux and surface temperature. The code estimates the heat flux that satisfy the energy equation and result in a minimal error in the measured temperature. As INTEMP solves 2-D heat conduction in the copper block, estimation of uncertainty is not straight forward as shown in Eq. (A.2). To quantify the uncertainty in the flux, the sampled temperature measurements is used to estimate the surface temperature and the heat flux. A noisy signal from the thermocouples at the transition region (maximum variation) is fed into INTEMP. INTEMP then estimates the heat flux and surface temperature for each input. The standard uncertainty in the estimated heat flux is 3.5 $\mathrm{kW/m^2}$ in the nucleate boiling regime and maximum of 17.5 $\mathrm{kW/m^2}$ (Less than 1% of the CHF) in the transition boiling regime. The maximum standard statistical uncertainty is 0.15 °C in the surface temperature.

Jet velocity

A turbine flow meter is used to measure the jet flow rate. The average jet velocity is estimated from the continuity equation. Jet velocity is calculated as follows,

$$V_j = c * F/A \tag{A.3}$$

where c is a constant, F is turbine meter frequency and A is the nozzle area. The uncertainty in the jet velocity is expressed as,

$$u = \sqrt{u_F^2} \tag{A.4}$$

OMEGA turbine flow meter uncertainty is $\pm 3 \times 10^{-3}$. The total combined uncertainty based on 95% confidence interval is 3×10^{-3} m/s.

Bubble diameter

Bubble diameter is measured from pictures taken as the bubble grow on the surface. The pictures are taken with a 6000 fps. The uncertainty in the time can be expressed from $u = a/\sqrt{3}$, where, a is the half width between the upper and lower limits. The uncertainty is $50\,\mu$s. The statistical standard uncertainty in the diameter measurements is 0.14 mm.

Bibliography

[1] D. Wolf, F. Incropera, Jet impingement boiling, Advances in Heat Transfer 23 (1993) 1–132.

[2] Y. Cheng, A. Tay, X. Hong, An experimental study of liquid jet impingement cooling of electronic components with and without boiling, in: Electronic Materials and Packaging, 2001. EMAP 2001. Advances in, 2001, pp. 369–375. doi:`10.1109/EMAP.2001.984012`.

[3] D. Zhou, C. Ma, Local jet impingement boiling heat transfer with R113, Heat and Mass Transfer 40 (2003) 539–549.

[4] Y. Katto, M. Kunihiro, Study of the mechanism of burn-out in boiling system of high burn-out heat flux, Bulletin of JSME 16 (1973) 1357–1366.

[5] L. Qiu, S. Dubey, F. H. Choo, F. Duan, Effect of conjugation on jet impingement boiling heat transfer, International Journal of Heat and Mass Transfer 91 (2015) 584–593.

[6] R. J. Copeland, Boiling Heat Transfer to a Water Jet Impinging an a Flat Surface (-1g), Ph.D. thesis, 1970.

[7] M. A. Ruch, J. Holman, Boiling heat transfer to a freon-113 jet impinging upward onto a flat, heated surface, International Journal of Heat and Mass Transfer 18 (1975) 51–60.

[8] M. Monde, Y. Katto, Burnout in a high heat-flux boiling system with an impinging jet, International Journal of Heat and Mass Transfer 21 (1978) 295–305.

[9] S. Ishigai, S. Nakanishi, T. Ochi, Boiling heat transfer for a plane water jet impinging on a hot surface, in: Sixth International Heat Transfer Conference, Toronto, ON, Canada, 1978, pp. 445–4450.

[10] Y. Miyasaka, S. Inada, Y. Owase, Critical heat flux and subcooled nucleate boiling in transient region between a two-dimensional water jet and a heated surface., Journal of Chemical Engineering of Japan 13 (1980) 29–35.

[11] C. F. Ma, A. E. Bergles, Jet impingement nucleate boiling, Int. J. Heat Mass Transfer 29 (1986) 1095–1101.

[12] D. E. Hall, F. P. Incropera, R. Viskanta, Jet impingement boiling from a circular free-surface jet during quenching: Part 1-Single-phase iet, Journal of Heat Transfer 123 (2001) 901.

[13] Z. Liu, Y. Qiu, Boiling heat transfer characteristics of nanofluids jet impingement on a plate surface, Heat and Mass Transfer 43 (2007) 699–706.

[14] Y. Qiu, Z. Liu, Nucleate boiling on the superhydrophilic surface with a small water impingement jet, International Journal of Heat and Mass Transfer 51 (2008) 1683 – 1690.

[15] D. T. Vader, F. P. Incropera, R. Viskanta, Convective nucleate boiling on a heated surface cooled by an impinging, planar jet of water, Journal of Heat Transfer Transactions of the ASME American Society of Mechanical Engineers Series C United States Journal Volume 1141 (1992) 152–160.

[16] X. Wang, M. Monde, Critical Heat Flux in Forced Convective Subcooled Boiling with a Plane Wall Jet (Effect of Subcooling on CHF), Heat and Mass Transfer 33 (1997) 167–175.

[17] V. K. Dhir, Mechanistic Prediction of Nucleate Boiling Heat Transfer–Achievable or a Hopeless Task?, Journal of Heat Transfer 128 (2006) 1.

[18] A. Omar, Experimental study and modeling of nucleate boiling during free planar liquid jet impingement, Ph.D. thesis, McMaster University, 2010.

[19] A. Ahmed, M. Hamed, Modeling of transition boiling under an impinging water jet, International Journal of Heat and Mass Transfer 91 (2015) 1273–1282.

[20] R. W. Bowring, Physical model based on bubble detachment and calculation of steam voidage in the subcooled region of a heated channel, Technical Report, HPR-10, Institutt

for Atomenergi, Halden, Norway, 1962.

[21] S. Rouhani, E. Axelsson, Calculation of void volume fraction in the subcooled and quality boiling regions, International Journal of Heat and Mass Transfer 13 (1970) 383–393.

[22] P. Griffith, J. A. Clark, W. M. Rohsenow, Void volumes in subcooled boiling, in: U.S. National Heat Transfer Conference, Chicago, 1958.

[23] O. Zeitoun, Subcooled flow boiling and condensation, Ph.D. thesis, McMaster University, 1994.

[24] V. H. Del Valle, D. Kenning, Subcooled flow boiling at high heat flux, International Journal of Heat and Mass Transfer 28 (1985) 1907–1920.

[25] N. Kurul, M. Z. Podowski, Multidimensional effects in forced convection subcooled boiling, in: Proceedings of the 9th International Heat Transfer Conference, volume 2, Hemisphere Publishing Corporation, 1990, pp. 21–26.

[26] N. Basu, G. R. Warrier, V. K. Dhir, Wall Heat Flux Partitioning During Subcooled Flow Boiling: Part 1—Model Development, Journal of Heat Transfer 127 (2005) 131 – 140.

[27] N. Basu, G. R. Warrier, V. K. Dhir, Wall Heat Flux Partitioning During Subcooled Flow Boiling: Part II—Model Validation, Journal of Heat Transfer 127 (2005) 141.

[28] N. Basu, Modeling and experiments for wall heat flux partitioning during subcooled flow boiling of water at low pressures, Ph.D. thesis, University of California Los Angeles, 2003.

[29] a. J. Robinson, R. L. Judd, The dynamics of spherical bubble growth, International Journal of Heat and Mass Transfer 47 (2004) 5101–5113.

[30] B. Mikic, W. Rohsenow, P. Griffith, On bubble growth rates, International Journal of Heat and Mass Transfer (1970) 657–666.

[31] L. Rayleigh, Viii. on the pressure developed in a liquid during the collapse of a spherical cavity, Philosophical Magazine Series 6 34 (1917) 94–98.

[32] M. S. Plesset, S. a. Zwick, The growth of vapor bubbles in superheated liquids, Journal

of Applied Physics 25 (1954) 493–500.

[33] N. Zuber, Hydrodynamic aspects of boiling heat transfer, Ph.D. thesis, 1959.

[34] M. Colombo, M. Fairweather, Prediction of bubble departure in forced convection boiling : A mechanistic model 85 (2015) 135–146.

[35] L. Zeng, J. Klausner, D. Bernhard, R. Mei, A unified model for the prediction of bubble detachment diameters in boiling systems II. Flow boiling, International Journal of Heat and Mass Transfer 36 (1993) 2271–2279.

[36] L. Zeng, J. Klausner, R. Mei, A unified model for the prediction of bubble detachment diameters in boiling systems— I. Pool boiling, International Journal of Heat and Mass Transfer 36 (1993) 2261–2270.

[37] W. VanHelden, C. VanDerGeld, P. Boot, Forces on bubbles growing and detaching in flow along a vertical wall, Int. H. Heat Mass Transfer 9310 (1995).

[38] G. E. Thorncroft, J. F. Klausner, R. Mei, Bubble forces and detachment models, Multiphase Science and Technology 13 (2001) 35–76.

[39] J. Klausner, R. Mei, D. Bernhard, L. Zeng, Vapor bubble departure in forced convection boiling, International Journal of Heat and Mass Transfer 36 (1993) 651–662.

[40] B. J. Yun, A. Splawski, S. Lo, C. H. Song, Prediction of a subcooled boiling flow with advanced two-phase flow models, Nuclear Engineering and Design 253 (2012) 351–359.

[41] A. Omar, M. S. Hamed, Modeling of bubble growth under an impinging free planar water jet, Heat Transfer Engineering 37 (2016).

[42] H. Robidou, H. Auracher, P. Gardin, M. Lebouche, Controlled cooling of a hot plate with a water jet, Experimental Thermal and Fluid Science 26 (2002) 123–129.

[43] Robidou, Local heat transfer from a hot plate to a water jet, Heat and Mass Transfer 39 (2003) 861–867.

[44] K. Suzuki, T. Kokubu, M. Nakano, H. Kawamura, I. Ueno, H. Shida, O. Ogawa, Enhancement of heat transfer in subcooled flow boiling with microbubble emission, Experimental Thermal and Fluid Science 29 (2005) 827–832.

[45] K. Suzuki, High heat flux transport by microbubble emission boiling, Microgravity

Science and Technology 19 (2007) 148–150.

[46] M. Gradeck, a. Kouachi, J. Borean, P. Gardin, M. Lebouché, Heat transfer from a hot moving cylinder impinged by a planar subcooled water jet, International Journal of Heat and Mass Transfer 54 (2011) 5527–5539.

[47] N. Seiler-Marie, J.-M. Seiler, O. Simonin, Transition boiling at jet impingement, International Journal of Heat and Mass Transfer 47 (2004) 5059–5070.

[48] L. Bogdanic, H. Auracher, F. Ziegler, Investigation of the two-phase structure in subcooled jet impingement boiling with a miniaturized optical probe, in: 8th International Conference on Boiling and Condensation Heat Transfer, Jun 3-7, Lausanne, Switzerland, 2012.

[49] J. Blum, W. Marquardt, Stability of Boiling Systems, International Journal of Heat and Mass Transfer 39 (1996) 3201–3033.

[50] M. Buchholz, H. Auracher, Improved Optical Probes and Their Validation for Local Measurements in Two-Phase Flows, in: Proceedings of the German-Japanese Workshop on Multi-Phase Flow, 2002, pp. B1–B10.

[51] D. Turner, Etch procedure for optical fibers, 1984. US Patent 4,469,554.

[52] D. M. Trujillo, H. R. Busby, Practical inverse analysis in engineering, CRC Press, 1997.

[53] R. Sugrue, J. Buongiorno, A modified force-balance model for predicting bubble departure diameter in subcooled flow boiling, in: Proceedings of The 15th International Topical Meeting on Nuclear Reactor Thermal-Hydraulics, NURETH-15, 2013.

[54] D. Zumbrunnen, F. Incropera, R. Viskanta, A laminar boundary layer model of heat transfer due to a nonuniform planar jet impinging on a moving plate 319 (1992) 311–319.

[55] A. B. Ahmed, M. S. Hamed, Experimental Investigation of Boiling Under a Planar Water Jet, in: 9th International Conference on Boiling and Condensation Heat Transfer, Apr 26-29, Boulder, CO, 2015.

[56] G. Taylor, The Instability of Liquid Surfaces when Accelerated in a Direction Perpendicular to their Planes. I, Proceedings of the Royal Society A: Mathematical, Physical and Engineering Sciences 201 (1950) 192–196.

[57] D. J. Lewis, The Instability of Liquid Surfaces when Accelerated in a Direction Perpendicular to their Planes. II, Proceedings of the Royal Society A: Mathematical, Physical and Engineering Sciences 202 (1950) 81–96.

[58] R. E. Bellman, R. Pennington, Effects of surface tension and viscosity on taylor instability. (1953).

[59] D. Y. Hsieh, Effects of Heat and Mass Transfer on Rayleigh-Taylor Instability, Journal of Basic Engineering 94 (1972) 156.

[60] M. K. Awasthi, G. S. Agrwal, Viscous potential flow analysis of Kelvin-Helmholtz instability of cylindrical interface, 2011. doi:`10.0000/ijamc.2011.3.2.271`.

[61] M. K. Awasthi, Viscous Corrections for the Viscous Potential Flow Analysis of Rayleigh–Taylor Instability With Heat and Mass Transfer, Journal of Heat Transfer 135 (2013) 071701.

[62] G. R. Baker, R. L. Mccrory, C. P. Verdon, S. a. Orszag, Rayleigh-Taylor instability of fluid layers, Journal of Fluid Mechanics 178 (1987) 161.

[63] B. J. Kim, J. H. Lee, K. D. Kim, Rayleigh–Taylor instability for thin viscous gas films: Application to critical heat flux and minimum film boiling, International Journal of Heat and Mass Transfer 80 (2015) 150–158.

[64] F. A. Hamad, F. Imberton, H. H. Bruun, An optical probe for measurements in liquid – liquid two-phase flow 8 (1997) 1122–1132.

[65] P. J. O'Rourke, A. A. Amsden, The TAB method for numerical calculation of spray droplet breakup, Technical Report, SAE Technical Paper, 1987.

[66] C. D. Eastwood, L. Armi, J. C. Lasheras, The breakup of immiscible fluids in turbulent flows, Journal of Fluid Mechanics 502 (2004) 309–333.

[67] J. C. Lasheras, C. Eastwood, C. Martínez-Bazán, J. L. Montañés, A review of statistical models for the break-up of an immiscible fluid immersed into a fully-developed turbulent flow, International Journal of Multiphase flows 28 (2002) 247–278.

[68] C. Coulaloglou, L. Tavlarides, Description of interaction processes in agitated liquid-liquid dispersions, Chemical Engineering Science 32 (1977) 1289–1297.

[69] W. Timm, K. Weinzierl, A. Leipertz, Heat Transfer in Subcooled Jet Impingement Boiling at High Wall Temperatures, International Journal of Heat and Mass Transfer 46 (2003) 1385–1393.

[70] A. Omar, M. Hamed, M. Shoukri, Modeling of Nucleate Boiling Heat Transfer under An Impinging Free Jet, International Journal of Heat and Mass Transfer 52 (2009) 5557–5566.

[71] P. McFadden, P. Grassmann, The relation between bubble frequency and diameter during nucleate pool boiling, int. J. heat mass transfer 5 (1962) 169–173.

[72] H. Ivey, Relationships between bubble frequency, departure diameter and rise velocity in nucleate boiling, International Journal of Heat and Mass Transfer 10 (1967) 1023–1040.

[73] G. Hazi, A. Markus, On the bubble departure diameter and release frequency based on numerical simulation results, International Journal of Heat and Mass Transfer 52 (2009) 1472–1480.